RECENT ICE SHEET SNOW ACCUMULATION AND FIRN STORAGE OF MELTWATER INFERRED BY GROUND AND AIRBORNE RADARS

by

Clément Miège

A dissertation submitted to the faculty of
The University of Utah
in partial fulfillment of the requirements for the degree of

Doctor of Philosophy

Department of Geography

The University of Utah

August 2015

The University of Utah Graduate School

STATEMENT OF DISSERTATION APPROVAL

The dissertation of **Clément Miège**

has been approved by the following supervisory committee members:

Richard R. Forster	, Chair	**Feb 2nd, 2015** Date Approved
Philip E. Dennison	, Member	**Feb 2nd, 2015** Date Approved
Simon C. Brewer	, Member	**Feb 2nd, 2015** Date Approved
Lora S. Koenig	, Member	**Feb 2nd, 2015** Date Approved
Jason E. Box	, Member	**Feb 2nd, 2015** Date Approved

and by **Andrea R. Brunelle**, Chair of

the Department of **Geography**

and by David B. Kieda, Dean of The Graduate School.

ABSTRACT

Recent surface mass balance changes in space and time over the polar ice sheets need to be better constrained in order to estimate the ice-sheet contribution to sea-level rise. The mass balance of any ice body is obtained by subtracting mass losses from mass gains. In response to climate changes of the recent decades, ice-sheet mass losses have increased, making ice-sheet mass balance negative and raising sea level. In this work, I better quantify the mass gained by snowfall across the polar ice sheets; I target specific regions over both Greenland and West Antarctica where snow accumulation changes are occurring due to rising air temperature.

Southeast Greenland receives 30% of the total snow accumulation of the Greenland ice sheet. In this work, I combine internal layers observed in ice-penetrating radar data with firn cores to derive the last 30 years of accumulation and to measure the spatial pattern of accumulation toward the southeast coastline. Below 1800 m elevation, in the percolation zone, significant surface melt is observed in the summer, which challenges both firn-core dating and internal-layer tracing. While firn-core drilling at 1500 m elevation, liquid water was found at ~20-m depth in a firn aquifer that persisted over the winter. The presence of this water filling deeper pore space in the firn was unexpected, and has a significant impact on the ice sheet thermal state and the estimate of mass balance made using satellite altimeters. Using a 400-MHz ice-penetrating radar, the extent of this widespread aquifer was mapped on the ground, and also more extensively

from the air with a 750-MHz airborne radar as part of the NASA Operation IceBridge mission. Over three IceBridge flight campaigns (2011-2013), based on radar data, the firn aquifer is estimated to cover ~30,000 km^2 area within the wet-snow zone of the ice sheet. I use repeated flightlines to understand the temporal variability of the water trapped in the firn aquifer and to simulate its lateral flow, following the gentle surface slope (< 1°) and undulated topography of the ice sheet surface toward the ablation zone of the ice sheet. The fate of this water is currently unknown; water drainage into crevasses and at least partial runoff is inferred based on the analysis of radar profiles from different years.

I also present results from a field expedition in West Antarctica, where data collection combined high-frequency (2-18 GHz) radar data and shallow (< 20 m) firn cores from Central West Antarctica, crossing the ice divide toward the Amundsen Sea. The radar-derived accumulation rates show a 75% increase (+0.20 m w.eq. y^{-1}) of net snow accumulation from the ice divide, toward the Amundsen Sea for a 70-km transect, assuming annual isochrones being detected in the radar profile. On the Ross Sea side of the divide, with accumulation rates less than 0.25 m w.eq. y^{-1} and significant wind redistribution, only a multi-annual stratigraphy is detected in the radar profile. Using radar, I investigated the small-scale variability within a radius of ~1.5 km of one firn-core site, and I find that the averaged variation in accumulation-rate in this area is 0.1 m w.eq. y^{-1} in the upper 25-m of the firn column, which is 20% of the average accumulation rate.

I dedicate this dissertation to my two grand-fathers, René and Georges.

Merci pour tout ce que vous m'avez appris.

TABLE OF CONTENTS

LIST OF TABLES

LIST OF FIGURES

ACKNOWLEDGEMENTS

The work accomplished during these five years of research was made possible by funding from the National Science Foundation Office of Polar Programs and a graduate fellowship from the National Aeronautics and Space Administration Earth and Space Sciences Program. I am grateful for support from a Chateaubriand Fellowship that sponsored my visit to the Centre d'Etude de la Neige/Météo France in Grenoble for five months.

I would like to thank my advisor Rick Forster for his patience, support, and expertise to guide me through the obstacles of graduate school. Rick also gave me responsibilities to lead research and fieldwork, allowing me to grow as an independent researcher. I am thankful to Jason Box who gave me the opportunity to come study in the U.S. and for teaching me all about fieldwork, Greenland weather, and climate variability. I am thankful to Lora Koenig for letting me join two Antarctic field expeditions, for being so responsive each time I needed help, and for the friendship that we built throughout the years. Finally, thanks to Simon Brewer and Phil Dennison, my University of Utah committee members, for their time to follow my PhD work, to evaluate my research skills during the qualifying exams, and later to evaluate this PhD dissertation.

The results presented in this work are due to the tremendous help of valuable collaborators and friends: Ludovic Brucker at NASA Goddard, Joe McConnell and Dan Pasteris at DRI, Summer Rupper and Landon Burgener at BYU, Susan Zager at CPS,

Laurent Mingo at BSI, Blue Spikes at ESA, and Kip Solomon at the University of Utah, Geology.

Many thanks to Samuel Morin and Matthieu Lafaysse at Météo France for their support with the snow model CROCUS and an extra thanks to the entire CEN team for their warm welcoming during my stay in fall 2012.

With major fieldwork components during this PhD work, I would like to thank all my other teammates who made the field such a happy place: Evan Burgess, Terry Gacke, Brian Ballard, Jay Kyne, Mike Atkinson, Randy Skinner, Jeff VanLooy, and Greg Vandeberg.

Thanks to Ed Waddington and Twit Conway who gave me the great opportunity to finish my PhD research at the Department of Earth and Space Sciences at the University of Washington.

I got the chance to have amazing officemates and great friends both at Univ. of Utah and Univ. of Washington: Evan, Annie, Kat, Al, Lisbeth, and others: thank you.

During grad school, it was great to have supportive friends. In Salt Lake City, Sebastian, Sylvain, Marc, Julie, Corinne, Clément, Stanley, and others were part of great Southern Utah adventures, Wasatch hikes, and backcountry skiing. In Seattle, the rainy weather was not bad at all with the very warm Tuesday-dinner group! During my visits in France, I had the chance to see my old friends and their families.

I am saving a few words in French for my family: Elsa, Guillaume, Maman, Papa, Mamie et Grand-mère: Un grand merci d'être toujours là pour moi.

Finally, thanks to Michelle for your incredible generosity, endless patience, and unconditional support along the way.

CHAPTER 1

INTRODUCTION

Human interference with our climate is occurring, which has raised the level of CO_2 in the atmosphere and caused the Earth surface to warm since the mid-20th century (IPCC, 2013). Recent climate changes affect ecosystems, ice reservoirs, weather extremes, and already have resulted in consequences for our society. The cryospheric response to climate change has been observed worldwide, in particular, glaciers are shrinking, Arctic sea ice extent is decreasing, drainage of ice from the ice sheets is increasing, permafrost is degrading, and the amount of water from spring snowpack is reducing for western North America (IPCC, 2013). In many regions of our planet, melting snow and ice have direct consequences on hydrological systems and on the quality and quantity of water resources (IPCC 2013).

The contribution of glaciers and ice sheets to sea level rise is significant. For the 21st century, mountain glaciers and ice caps contribute to more than half of the sea level rise (SLR) coming from ice loss (Meier et al., 2007). For the last two decades (1992-2010), the Greenland and Antarctic ice sheets contributed 0.43±0.11 mm yr^{-1} and 0.27±0.11 mm yr^{-1} to SLR, respectively, based on reconciled observations and simulations (Shepherd et al., 2012; IPCC 2013). From 2003-2009, mountain glaciers contributed 0.76±0.37 mm yr^{-1} to SLR (Gardner et al., 2013; IPCC, 2013).

Mountain glaciers are rapidly shrinking, dominating the cryospheric contribution to SLR today, and their total contribution is estimated to be + 0.41 m of vertical SLR (IPCC, 2013). The ice sheets' total ice mass corresponds to a SLR of + 65.7 m, with +7.4 m for Greenland and +58.3 m for Antarctica. Reducing the uncertainties in sea-level rise contributions from Greenland and Antarctica is crucial for policy and decision makers, since coastal cities will be at a very likely risk of flooding by the end of the 21st century (IPCC, 2013).

Ice loss from the ice sheets can be partitioned between ice discharge from Antarctica and from Greenland due to ice calving at the edges and due to surface melt runoff to the ocean (occurs primarily for Greenland and the Antarctic Peninsula). To offset the mass loss, the ice sheet is gaining mass by snowfall, which is not equally distributed over the ice sheets. The mass balance of each ice sheet is established by adding mass losses and mass gains for each year.

For Greenland, surface melt contributed to 50% of the total ice loss for the last decades (van den Broeke et al., 2009). For the 2009-2012 period, the surface melt contribution to ice loss increased to ~70% (Enderlin et al., 2014) since it includes the exceptional and widespread melt during summer 2012 (Nghiem et al., 2012). Compensating for some of the mass loss, and correlated with increasing air temperature over the ice sheet, an increasing accumulation trend has been observed since 1958 (Hanna et al., 2008; Wake et al., 2009). However, regional signal trends are important; for example, the snow falling in the southeastern corner of Greenland contributes 30% of the total accumulation of the ice sheet. This region is poorly constrained and discrepancies of 1.5 m w.e. yr^{-1} exist between regional climate model estimates and there

has been no significant increasing trend of accumulation since 1958 (Burgess et al., 2010; Box et al., 2013; Miège et al., 2013).

Since 1979, the Antarctic ice sheet lost mass by two main processes: basal ice-shelf melt and ice discharge (e.g., Rignot et al., 2013a). Surface melt is also occurring but is typically restricted to coast areas of Antarctica and the peninsula; most of the melt does not contribute directly to SLR as it refreezes in the subjacent firn layer (Kuipers Munneke et al., 2012). Monitoring the firn layer within the ice shelves is important to assess their stability and to convert volume change to mass change conversion (Helsen et al., 2008; Scambos et al., 2009). The West Antarctic Ice Sheet (WAIS) is a critical research target as it is grounded below sea level and recent studies have shown there is potential for the ice-sheet collapse in the near future (Joughin et al., 2014; Rignot et al., 2014). Along the Amundsen Sea coast, the main outlet glaciers are thinning, retreating, and accelerating (Pritchard et al., 2009; Rignot et al., 2014). At the surface of the WAIS, air temperature is increasing significantly (Steig et al., 2009; Bromwich et al., 2013). This observed recent temperature warming trend would suggest synchronous increase of the snow accumulation. However, this increased accumulation pattern has not been yet confirmed from firn-core studies in central WAIS (e.g., Frezzotti et al., 2013).

1.1. Motivation and objectives

In this dissertation, I focus on the ice sheet mass input, primarily snowfall. I do this by reconstructing the snow accumulation history for the last ~40 years. I target the specific regions of Southeast Greenland and West Antarctica where important changes in snow accumulation are taking place. Since accumulation rates vary in space and time, I use ground and airborne snow and ice sounding radars to extend point observations from

firn cores by tracking internal isochrones in the radar data. In Southeast Greenland, a firn aquifer was observed with significant implications for mass balance estimation for the ice sheet. I map the aquifer extent using similar airborne ice-sounding radars, analyze its temporal variability, and simulate the flow of water in the aquifer.

1.1.1. Southeast Greenland recent accumulation rate history

This chapter builds on the recent work by Burgess et al. (2010), who highlighted the importance of Southeast Greenland when estimating accumulation rates for the entire Greenland ice sheet. The Southeast part of Greenland represents 30% of the entire ice sheet accumulation and interannual variability (Burgess et al., 2010). In this region, the bulk of the accumulation is near the southeast coast with coastal storms bringing a significant amount of moisture toward the ice sheet interior, with accumulation rates simulated up to 5 m w.eq. y^{-1} (e.g., Rae et al., 2012). However, with strong interannual variability, regional climate models do not always simulate the correct accurate amount of yearly snow water equivalent in this region. Differences between models are up to 1.5 m w.eq y^{-1}, representing a non-negligible mass uncertainty in the ice sheet yearly balance (Box et al., 2013). By conducting two separate snowmobile traverses in spring 2010 and 2011 in southeast Greenland, we reduce the accumulation-rate uncertainties in this region and improve estimates of the ice sheet mass budget. The 2010 and 2011 Arctic Circle Traverses (ACT) follow on from the original 2004 ACT traverse (Spikes et al., 2007), where during each traverse we extracted a total of three 50-m firn cores and used seasonal variations of specific chemical species to date the cores (McConnell et al., 2002). After sampling the firn core along an elevation gradient, we used a 400-MHz

ground-penetrating radar (GPR) to trace continuous isochronous internal horizons in order to fully capture the spatial variability in accumulation. Below 2000 m a.s.l., the firn-core dating is challenged by the presence of surface melt and meltwater vertically percolating into the underlying snowpack. Only high winter snowfall regions could prevent the meltwater from reaching the previous summer firn layer and not perturbing the snow/firn chemistry used for dating.

1.1.2. Greenland firn aquifer

Based on a successful 2010 season when one firn core collected at 1800 m elevation was successfully dated, lower elevation drill sites were targeted. In the early spring of 2011, we drilled a firn core at 1500 m a.s.l. and a firn aquifer was identified with a water table at 10-m depth below the snow surface. After finding the subsurface water, using a 400-MHz GPR, we identified a spatially extensive bright reflector at a similar depth in the vicinity of the firn-core site. A few days later, this widespread firn aquifer was confirmed when we drilled at another location a few kilometers upstream from the first location. At the second location, the GPR bright horizon was at ~25 m depth, matching the drilling depth where subsurface water was also found. Eleven days prior to this discovery, a 750-MHz radar system onboard the NASA Operation IceBridge (OIB) airplane flew a similar line to our ground radar. This distinct bright reflector was also observed, and I correlated it to the ground observations. This correlation and the abundance of the OIB flights over the ice sheet allowed the mapping of this feature elsewhere than at the field location.

To date, two manuscripts have been published by the 'firn aquifer team'. A first manuscript, by Forster et al. (2014), presents the aquifer characteristics and an initial mapping. Further field investigations led to a second manuscript by Koenig et al. (2014), where a volume of liquid water within the aquifer was estimated. While these two manuscripts are not included directly in this PhD dissertation as stand-alone chapters, I significantly contributed to their preparation and publication.

The firn aquifer stores a significant amount of liquid water for more than a year in the lower part of the accumulation zone (wet-snow zone), which leads to uncertainty in estimates of meltwater runoff into the ocean. The storage of this significant volume of water at depth could be partly responsible for the discrepancies between mass loss simulated by regional climate models and the satellite-derived mass loss from altimetry and gravimetry (Harper, 2014). This chapter provides an updated map of the firn aquifer using three airborne radar campaigns (2011-2013) as well as repeated ground and airborne observations. I identified that the first observations of the firn aquifer were made in 1993 and were not only synchronous to the last decade of enhanced surface melt. Lateral flow within the firn aquifer is imaged and connections with crevasse networks are presented.

1.1.3. West Antarctica recent snow accumulation rate history

West Antarctica is also a rapidly changing region that needs better measurements to reduce uncertainties in surface mass balance. In the field, we used a similar sampling strategy to the ACT in Greenland, collecting high-frequency radar data and shallow firn cores. Two Satellite Era Accumulation Traverses (SEAT) were completed in 2010 and

2011, travelling from Central WAIS toward the Amundsen Sea. The main research objectives for this chapter are the following: (1) Confirm the annual accumulation signal from the airborne radar (Medley et al., 2013). (2) Compare firn-core-derived accumulation rates with radar-derived accumulation rates. (3) Capture spatio-temporal changes in accumulation over the last 30 years. (4) Confirm that firn-core observations can be representative to a small region (<1 km^2) by using detailed radar grids around the core site.

Based on the SEAT firn cores obtained in 2010, Burgener et al. (2013) noticed an unexpected but significantly decreasing trend of accumulation for the last 40 years, despite the fact that air temperature has been increasing during the same period at the nearby Byrd station (Bromwich et al., 2013). However, observations across WAIS do not show any consistent trend in accumulation. Recent observations over the Antarctic Peninsula at the Gomez ice core site found a significant increase of accumulation (Thomas et al., 2009), but in the Amundsen sea sector (upstream of Thwaites and Pine Island Glaciers), no accumulation trend is found (Medley et al., 2014). However, the signal-to-noise ratio remains low, challenging the establishment of a clear trend since high interannual variability and short time period available could mask the trend. In this chapter, I will present the high-frequency radar data and I will derive past snow accumulation rates in order to bring spatial context to the single-point firn-core observations.

1.2. Radar background

This work uses RAdio Detection And Ranging (RADAR) techniques to image subsurface features in the radio and microwave frequency ranges over snow and ice.

Historically, application of radar to glaciological problems began in the 1960s, at the same time as the International Geophysical Year in 1957 (Waite and Schmidt, 1962). While flying over the ice sheets, airplane pilots realized that their high-frequency radar altimeters were transparent to the snow surface interface, leading to an overestimation of the distance between the airplane and the snow surface (Waite and Schmidt, 1962). Since then, radio-echo soundings have been developed for a wide range of application between seasonal snow and deep ice sheet internal layers mapping (e.g., Jol, 2008, chapter 12). Nonmagnetic, low conductivity materials like dry snow and ice provide excellent mediums for radar investigations, but are sometimes challenged by liquid water in snow and ice where absorption loss is higher due to a strong dielectric contrast and an increase of the ice temperature to near 0°C. For temperate ice, lower-frequency (1-32 MHz) radar systems have been successfully used to image subsurface structure, for example in Alaska and Iceland (Sverrisson et al., 1980; Rignot et al., 2013b).

1.2.1. Electromagnetic waves and dielectric constant

An electromagnetic (EM) wave is composed of two fields, an electric field and a magnetic field that are perpendicular to each other. An EM wave is characterized by its wavelength (λ) and its frequency (υ); the relationship between the two is $= c/\lambda$, where c is the speed of light (~$3x10^8$ m s^{-1}). In 3-D space and at a given time, the EM field has a direction of propagation and a magnitude. The polarization describes the magnitude and direction of the EM wave as a function of space and time. If the propagation is along a straight line, the polarization is linear. If the electric and magnetic fields rotate along the propagation axis, the polarization is circular, and can also be ellipsoidal (along an

ellipse). But for a natural source of radiation, the EM wave follows a random polarization (Rees, 1990).

When the EM radiation interacts with a surface, which can be the air/snow interface or a buried surface, three forms of interactions are present as illustrated in Figure 1.1. The absorption process takes a certain amount of energy and transfers it to the material that absorbs by it. The reflection is a result of in part the incoming energy that is reflected back toward the sensor. Finally some energy is transmitted and will travel through the second medium.

Each material will have a different relative permittivity (dielectric constant) and electric conductivity characteristics; therefore, the velocity of an EM wave and the quantity of energy (absorbed vs. transmitted) will change depending on the material (Mätzler 2006). For example, salty water and dry snow will have different conductivity and dielectric constant values residing in a different attenuation due to their properties. The velocity of an EM wave across a given material depends on the dielectric constant (ε) and the magnetic susceptibility (μ) following equation (1.1). If the material is nonmagnetic, which is the case of most of the materials studied at the Earth surface, $\mu = 1$ and the equation (1.1) can be simplified.

The dielectric constant has two parts (see equation 1.2), the real part (ε') that varies between materials and the imaginary part (ε'') that will be zero for the air, but will have an impact for other mediums; for example, ε'' can vary between 10^{-4} and 10^{-2} for dry snow. If we consider the imaginary part negligible, the velocity of the EM wave in a given medium can be approximated by equation (1.3).

$$v = 1/\sqrt{\mu * \varepsilon} \qquad (1.1)$$

$$\text{with } \varepsilon = \varepsilon' - i\varepsilon'' \qquad (1.2)$$

$$v_f = c/\sqrt{\varepsilon'} \qquad (1.3)$$

Lower dielectric constants result in faster propagation through a material. For example, an EM wave penetrates faster through snow (ε'=1.5 to 2.4) than through ice (ε'=3.15).

1.2.2. Penetration depth

One way to define the penetration depth is related to the transmitted power. The "power penetration depth" of a material corresponds to the depth when the initial transmitted power is reduced to e^{-1} or (37%) of its initial value ($P(z) = P_0/e$). Therefore, the penetration depth is independent of the strength of the initial transmit power value. The penetration depth of a material depends on the total extinction loss rate. The extinction coefficient is the sum of the absorption coefficient and the scattering coefficient (Ulaby et al., 1981).

For microwave radiation, penetration depth of an electromagnetic (EM) wave is essentially dependent on wavelength of the radar (active) or the radiometer (passive) used. Shorter wavelengths (higher frequencies) will increase vertical resolution but allow smaller penetration depths (Surdyk, 2002). For the East Antarctic Plateau, the penetration depth ranges between 0.74 and 2m at 37GHz and 2.5-5 m at 19 GHz (Brucker et al., 2011). Below 10 GHz, penetration depths are greater, for example between 20 and 40 m at 6.6 GHz.

The penetration depth in a dry-snow environment is limited by losses due to scattering and absorption. Scattering is caused by reflection, refraction, or diffraction

processes, which distribute the incoming energy toward other directions than receiver, in a radar case. Absorption occurs when the electrical conductivity of the medium is non-zero. Both processes are dependent on the size of individual snow grains, the temperature, and the snow density. Surdyk (2002) performed a sensitivity test of the penetration depths for the three variables. At frequencies below about 10GHz, the important variables affecting penetration depths are the temperature and the interface reflections due to density changes (Surdyk, 2002). Between 10 and 20 GHz, the three variables have a non-negligible influence on penetration depth since they are interdependent. For example, higher surface temperature can produce larger snow grains, reducing penetration depth. Finally, higher than 20 GHz, snow-grain size represents the main factor influencing the penetration depth during the experiments (Surdyk, 2002). At an ice-sheet scale, it has been observed that the penetration depth for Greenland snow would be half the penetration depth for Antarctic snow (Surdyk, 2002). In addition, the interdependence between penetration depth and snow thermal conductivity plays a role for uncertainty estimates, since an uncertainty on the conductivity propagates into an uncertainty on the propagation depth (Picard et al., 2009).

To image the bedrock below an ice sheet, lower frequencies are used. At these frequencies, in the radio bands, dielectric absorption, volume scattering from air bubbles, depolarization, and reflections from the internal layers are the main sources of signal extinction at depth (e.g., Paden et al., 2005). The dielectric absorption remains the main cause of extinction of the EM waves at the radio frequencies. The loss from spherical spreading and dielectric loss must be compensated by sufficient signal-to-noise ratio near the bedrock. The transmitted power-to-received power ratio decreases with depth.

Increasing transmitted power (as well as gain) could improve the return loss at depth; techniques like arraying two transmit antennas in the along-track direction were successful (Paden et al., 2005).

1.2.3. Radar systems

In this dissertation, different radar systems will be used depending on the application and the resolution needed. The Greenland chapters present results from internal layers detected with a 400-MHz GPR that I used to derive snow accumulation rate histories and map the surface of the firn aquifer in Southeast Greenland (Miège et al., 2013; Forster et al., 2014). With a ~30-cm vertical resolution, this GPR allowed near-annual accumulation rates to be estimated in high-accumulation regions (>1 m w.eq. yr^{-1}; Spikes et al., 2004; 2007; Miège et al., 2013). To explore the regional variability of the firn aquifer, we use the NASA Operation IceBridge 750 MHz Accumulation Radar. With a 65-cm vertical resolution, this radar can successfully image the firn aquifer (Forster et al., 2014).

For the Antarctic chapter, higher-frequency systems were used to map annual horizons in low accumulation regions (< 0.25 m w.eq. y^{-1}). Instead of a single pulse radar system, frequency-modulated continuous-wave (FMCW) radars were preferred. This other generation of radars has been designed specifically for cryospheric research questions (e.g., Marshall and Koh, 2008). During fieldwork, two FMCW radars were simultaneously imaging the snow surface and subsurface. A "Ku-band" radar was operating at a frequency range of 12.5–18.5 GHz and "Snow" Radar was operating at a lower frequency range (2-8 GHz). Penetration depth was limited to 20-30 m but

corresponded to the firn-core depth (< 20 m) and the vertical resolution was about ~4 cm in dry snow (Rodriguez-Morales, 2013).

1.3. Accumulation variability and uncertainties

I investigate the spatio-temporal variations of accumulation using ice cores and radars and compare them with snow accumulation outputs from numerical models with different spatial footprints and temporal resolutions. In the following, I describe the firn-core method and the radar method to estimate accumulation rate, and I discuss the accumulation variability due to climate variability as well as the uncertainties associated.

Firn cores allow the sampling of the last 30-50 years of accumulation history depending on the averaged accumulation rate at a given point location. By looking at the seasonal cycle of chemical components used as temporal proxies, for example hydrogen peroxide, the non-sea-salt sulfur-to-sodium ratio, and water stable isotopes, a depth-age scale can be retrieved with about one year resolution. Summer surface melt or other surface snow processes can perturb the annual cycle and can challenge establishing a depth-age scale, as the chemistry peaks are not always sharp. Rupper et al. (2015) discussed the uncertainties associated with the mean, trend, and variability of snow accumulation for a region in West Antarctica using five shallow firn-core records. This study found that peak-identification and peak-date uncertainties affect trend estimates and interannual variability in accumulation. At a firn-core scale (a single point), the interannual variability is due to a combination of climate variability (storm and snowfall frequencies and intensities), wind redistribution, snow sublimation, and dating uncertainties. Therefore, the standard deviations from the mean accumulation for 30-40

years do not solely represent climate variability. In addition, a single core lacks spatial variability, and contains glaciological noise due to snow processes like wind redistribution and snow sublimation, which can alter the interannual signal based on location on an often undulated (~10 km wavelength) snow surface. To retrieve information about the spatial variability of accumulation rates and assess the robustness of a temporal trend, multiple firn cores can be collected in different locations near the primary core site, in an effort to represent variability over a larger region. Correlation coefficients are used to measure the strength and direction of a linear relationship between two variables. If correlation coefficients between firn cores of a same region are close to 1, it means that the different accumulation records capture the same climate variability. In addition, the coefficient of determination (r^2 value) will be useful to provide the proportion of the variation of one variable that could predict another one. By looking at the correlation between the accumulation record of a firn core and a regional climate pattern like the North Atlantic Oscillation (NAO), we aim to quantify whether the moisture source origin and variability of a certain region are due to regional climate patterns. For example, if the correlation coefficient (r) is equal to 0.8, then the coefficient of determination (r^2) will be equal to 0.64, meaning that 64% of the total variation is explained by the relationship between the climate pattern and the accumulation records. Different temporal filters such as a 5-year triangular filter could improve the correlation coefficients by filtering out part of the glaciological noise from the signal.

The spatial variability of accumulation is further explored using ground-penetrating radars deployed either from the ground or from an airplane. Depending on the vertical resolution of the radar, the sampling location, the averaged accumulation rate,

and the snow surface conditions (with or without the presence of melt over a year), internal horizons detected by radar will have a multiyear, annual, to subannual resolution. Over the dry firn of West Antarctica, the ability of tracing annual layers allows the retrieval of the full temporal variability of the signal to directly compare with the firn cores and also climate reanalysis (Medley et al., 2013). Medley et al. (2013) found a good agreement between the radar-derived accumulation rates and global climate reanalysis data (e.g., ERA-interim, MERRA) capturing a similar temporal variability. In addition, the regional climate model RACMO2 has a finer resolution and therefore is able to better capture the spatial changes of accumulation. If only multiyear accumulation rates are derived from radar data, the temporal variability will be averaged out; therefore, the variation from the mean will be smaller for specific time periods. The radar-derived accumulation method captures the temporal variability with a degree of averaging dependent on the radar data and captures the spatial variability with a better resolution than typical 25 km grids used for climate simulations. At least two sources of variation are present in the data, which are the real variability and the errors from measurements. The two variation sources can be difficult to untangle to only extract the signal of the spatiotemporal variability due to climate variability. While inferring temporal variations in accumulation, if an internal annual layer is not traced, the subsequent accumulation rates will be higher for this specific time. As the tracing process is done manually, an error is difficult to quantify. In addition, the radar travel-time-to-depth conversion is dependent on the medium characteristics, which depend on density changes in the firn. If a steady-state spatially invariant density profile is used, spatial density changes at small scale will not be taken into account, which introduces uncertainties that are challenging to

quantify. For example, an area with density higher than normal will tend to underestimate the thickness between two layers and also overestimate the conversion in snow water equivalent.

Finally, numerical climate models also capture temporal and spatial variability of accumulation with a particular spatial and temporal resolution. I will compare my firn-core and radar-derived accumulation rates to regional climate model-derived accumulation rates to understand if averaged accumulation rates are captured by my two independent methods.

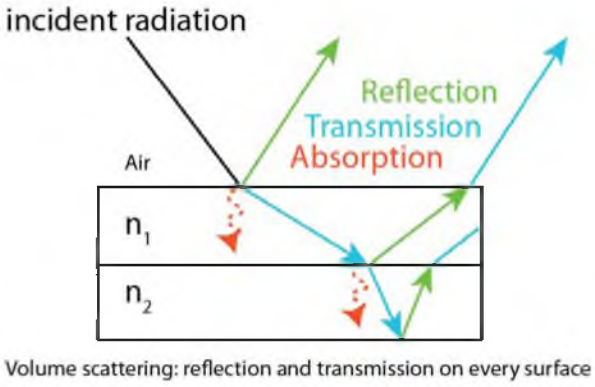

Figure 1.1: Illustration of the EM wave interacting with a specific medium with electromagnetic properties n_1 and another material of properties n_2. The three forms of interactions are presented here, and there is a reflection at every interface.

1.4. References

Box, J. E. et al. (2013), Greenland ice sheet mass balance reconstruction. Part I: Net Snow Accumulation (1600–2009), *J. Climate*, *26*(11), 3919–3934, doi:10.1175/JCLI-D-12-00373.1.

Van den broeke, M., J. Bamber, J. Ettema, E. Rignot, E. Schrama, W. J. Van De Berg, E. Van Meijgaard, I. Velicogna, and B. Wouters (2009), Partitioning recent Greenland mass loss, *Science*, *326*(5955), 984–986, doi:10.1126/science.1178176.

Bromwich, D. H., J. P. Nicolas, A. J. Monaghan, M. A. Lazzara, L. M. Keller, G. A. Weidner, and A. B. Wilson (2013), Central West Antarctica among the most rapidly warming regions on Earth, *Nature Geosci*, *6*(2), 139–145, doi:10.1038/ngeo1671.

Brucker, L., G. Picard, L. Arnaud, J.-M. Barnola, M. Schneebeli, H. Brunjail, E. Lefebvre, and M. Fily (2011), Modeling time series of microwave brightness temperature at Dome C, Antarctica, using vertically resolved snow temperature and microstructure measurements, *Journal of Glaciology*, *57*(201), 171–182, doi:10.3189/002214311795306736.

Burgener, L. et al. (2013), An observed negative trend in West Antarctic accumulation rates from 1975 to 2010: Evidence from new observed and simulated records, *Journal of Geophysical Research: Atmospheres*, *118*(10), 4205–4216, doi:10.1002/jgrd.50362.

Burgess, E. W., R. R. Forster, J. E. Box, E. Mosley-Thompson, D. H. Bromwich, R. C. Bales, and L. C. Smith (2010), A spatially calibrated model of annual accumulation rate on the Greenland Ice Sheet (1958–2007), *Journal of Geophysical Research: Earth Surface*, *115*(F2), n/a–n/a, doi:10.1029/2009JF001293.

Enderlin, E. M., I. M. Howat, S. Jeong, M.-J. Noh, J. H. van Angelen, and M. R. van den Broeke (2014), An improved mass budget for the Greenland ice sheet, *Geophys. Res. Lett.*, *41*(3), 2013GL059010, doi:10.1002/2013GL059010.

Forster, R. R. et al. (2014), Extensive liquid meltwater storage in firn within the Greenland ice sheet, *Nature Geosci*, *7*(2), 95–98, doi:10.1038/ngeo2043.

Frezzotti, M., C. Scarchilli, S. Becagli, M. Proposito, and S. Urbini (2013), A synthesis of the Antarctic surface mass balance during the last 800 yr, *The Cryosphere*, *7*(1), 303–319, doi:10.5194/tc-7-303-2013.

Gardner, A. S. et al. (2013), A reconciled estimate of glacier contributions to sea level rise: 2003 to 2009, *Science*, *340*(6134), 852–857, doi:10.1126/science.1234532.

Hanna E, P Huybrechts, K Steffen, J Cappelen, R Huff, C Shuman, T Irvine-Fynn, S Wise, M Griffiths (2008), Increased runoff from melt from the Greenland ice sheet: A response to global warming, *Journal of Climate*, *21*, 331–341, doi:10.1175/2007JCLI1964.1.

Harper, J. (2014), Cryosphere: Greenland's lurking aquifer, *Nature Geosci*, *7*(2), 86–87, doi:10.1038/ngeo2061.

Helsen, M. M., M. R. Van Den Broeke, R. S. W. Van De Wal, W. J. Van De Berg, E. Van Meijgaard, C. H. Davis, Y. Li, and I. Goodwin (2008), Elevation changes in Antarctica mainly determined by accumulation variability, *Science*, *320*(5883), 1626–1629, doi:10.1126/science.1153894.

Jol, H. M. (2008), *Ground Penetrating Radar Theory and Applications*, Elsevier.

Joughin, I., B. E. Smith, and B. Medley (2014), Marine ice sheet collapse potentially under way for the Thwaites Glacier Basin, West Antarctica, *Science*, *344*(6185), 735–738, doi:10.1126/science.1249055.

Koenig, L. S., C. Miège, R. R. Forster, and L. Brucker (2014), Initial in situ measurements of perennial meltwater storage in the Greenland firn aquifer, *Geophysical Research Letters*, *41*, 1–5, doi:10.1002/2013GL058083.

Kuipers Munneke, P., G. Picard, M. R. van den Broeke, J. T. M. Lenaerts, and E. van Meijgaard (2012), Insignificant change in Antarctic snowmelt volume since 1979, *Geophys. Res. Lett.*, *39*(1), L01501, doi:10.1029/2011GL050207.

Marshall, H.-P., and G. Koh (2008), FMCW radars for snow research, *Cold Regions Science and Technology*, *52*(2), 118–131, doi:10.1016/j.coldregions.2007.04.008.

Mätzler, C. (2006), Thermal microwave radiation applications for remote sensing, *Institution of Engineering and Technology*, London.

McConnell, J. R., G. W. Lamorey, S. W. Lambert, and K. C. Taylor (2002), Continuous ice-core chemical analyses using inductively coupled plasma mass spectrometry, *Environ. Sci. Technol.*, *36*(1), 7–11, doi:10.1021/es011088z.

Medley, B. et al. (2013), Airborne-radar and ice-core observations of annual snow accumulation over Thwaites Glacier, West Antarctica confirm the spatiotemporal variability of global and regional atmospheric models, *Geophysical Research Letters*, *40*(14), 3649–3654, doi:10.1002/grl.50706.

Medley, B. et al. (2014), Constraining the recent mass balance of Pine Island and Thwaites glaciers, West Antarctica, with airborne observations of snow accumulation, *The Cryosphere*, *8*(4), 1375–1392, doi:10.5194/tc-8-1375-2014.

Meier, M. F., M. B. Dyurgerov, U. K. Rick, S. O'Neel, W. T. Pfeffer, R. S. Anderson, S. P. Anderson, and A. F. Glazovsky (2007), Glaciers dominate eustatic sea-level rise in the 21st century, *Science*, *317*(5841), 1064–1067, doi:10.1126/science.1143906.

Miège, C., R. R. Forster, J. E. Box, E. W. Burgess, J. R. McConnell, D. R. Pasteris, and V. B. Spikes (2013), Southeast Greenland high accumulation rates derived from firn cores and ground-penetrating radar, *Annals of Glaciology*, *54*(63), 322–332, doi:10.3189/2013AoG63A358.

Nghiem, S. V., D. K. Hall, T. L. Mote, M. Tedesco, M. R. Albert, K. Keegan, C. A. Shuman, N. E. DiGirolamo, and G. Neumann (2012), The extreme melt across the Greenland ice sheet in 2012, *Geophysical Research Letters*, *39*(20), doi:10.1029/2012GL053611.

Paden, J. D., C. T. Allen, S. Gogineni, K. C. Jezek, D. Dahl-Jensen, and L. B. Larsen (2005), Wideband measurements of ice sheet attenuation and basal scattering, *IEEE Geoscience and Remote Sensing Letters*, *2*(2), 164–168, doi:10.1109/LGRS.2004.842474.

Picard, G., L. Brucker, M. Fily, H. Gallée, and G. Krinner (2009), Modeling time series of microwave brightness temperature in Antarctica, *Journal of Glaciology*, *55*(191), 537–551, doi:10.3189/002214309788816678.

Rees, W. G. (1990), Physical Principles of Remote Sensing, *Cambridge University Press*.

Rignot, E., S. Jacobs, J. Mouginot, and B. Scheuchl (2013a), Ice-Shelf melting around Antarctica, *Science*, *341*(6143), 266–270, doi:10.1126/science.1235798.

Rignot, E., J. Mouginot, C. F. Larsen, Y. Gim, and D. Kirchner (2013b), Low-frequency radar sounding of temperate ice masses in Southern Alaska, *Geophysical Research Letters*, *40*(20), 5399–5405, doi:10.1002/2013GL057452.

Rignot, E., J. Mouginot, M. Morlighem, H. Seroussi, and B. Scheuchl (2014), Widespread, rapid grounding line retreat of Pine Island, Thwaites, Smith, and Kohler glaciers, West Antarctica, from 1992 to 2011, *Geophys. Res. Lett.*, *41*(10), 3502–3509, doi:10.1002/2014GL060140.

Rodriguez-Morales, F. et al. (2013), Advanced multifrequency radar instrumentation for polar research, *IEEE Transactions on Geoscience and Remote Sensing*, doi:10.1109/TGRS.2013.2266415.

Rupper, S., W. F. Christensen, E. J. Bickmore, L. Burgener, L. Koenig, M. Koutnik, C. Miège, and R. Forster (2015), The effect of dating uncertainties on net accumulation estimates from firn cores, *Journal of Glaciology*, *61*(225), 163–172.

Scambos et al. (2009), Ice shelf disintegration by plate bending and hydro-fracture: Satellite observations and model results of the 2008 Wilkins ice shelf break-ups, *Earth and Planetary Science Letters*, *280*, 51–60, doi:10.1016/j.epsl.2008.12.027.

Shepherd, A. et al. (2012), A reconciled estimate of ice-sheet mass balance, *Science*, *338*(6111), 1183–1189, doi:10.1126/science.1228102.

Spikes, V. B., G. S. Hamilton, S. A. Arcone, S. Kaspari, and P. A. Mayewski (2004), Variability in accumulation rates from GPR profiling on the West Antarctic plateau, *Annals of Glaciology*, *39*(1), 238–244, doi:10.3189/172756404781814393.

Spikes, V. B., J. R. McConnell, and J. R. Banta (2007), Annual layer mapping and net snowfall measurements across the southern Greenland ice sheet using shallow radar and ice cores, *AGU Fall Meeting Abstracts*, *-1*, 0087.

Steig, E. J., D. P. Schneider, S. D. Rutherford, M. E. Mann, J. C. Comiso, and D. T. Shindell (2009), Warming of the Antarctic ice-sheet surface since the 1957 International Geophysical Year, *Nature*, *457*(7228), 459–462, doi:10.1038/nature07669.

Stocker, T.F, D. Qin, G. - K. Plattner, M. Tignor, S.K. Allen, J. Bosc hung, A. Nauels, Y. Xia, V. Bex, and P.M. Midgley (2013), Climate Change 2013: The Physical Science Basis. Contribution of Working Group I to the Fifth Assessment Report of the Intergovernmental Panel on Climate Change, *Cambridge University Press, Cambridge, United Kingdom and New York, NY, USA,*, 1535, doi:10.1017/CBO9781107415324.

Surdyk, S. (2002), Using microwave brightness temperature to detect short-term surface air temperature changes in Antarctica: An analytical approach, *Remote Sensing of Environment*, *80*(2), 256–271, doi:10.1016/S0034-4257(01)00308-X.

Sverrisson M, Johannsson AE, and Bjornsson H (1980), Radio-echo equipment for depth sounding of temperate glaciers, *Journal of Glaciology*, *25*(93), 477–486.

Thomas, E. R., P. F. Dennis, T. J. Bracegirdle, and C. Franzke (2009), Ice core evidence for significant 100-year regional warming on the Antarctic Peninsula, *Geophys. Res. Lett.*, *36*(20), L20704, doi:10.1029/2009GL040104.

Ulaby, F. T., R. K. Moore, and A. K. Fung (1981), Microwave Remote Sensing: Active and Passive, *Addison-Wesley Publishing Company, Advanced Book Program/World Science Division*.

Waite, A. H., and S. J. Schmidt (1962), Gross errors in height indication from pulsed radar altimeters operating over thick ice or snow, *Proceedings of the IRE*, *50*(6), 1515–1520, doi:10.1109/JRPROC.1962.288195.

Wake, L. M., P. Huybrechts, J. E. Box, E. Hanna, I. Janssens, and G. A. Milne (2009), Surface mass-balance changes of the Greenland ice sheet since 1866, *Annals of Glaciology*, *50*(50), 178–184, doi:10.3189/172756409787769636.

CHAPTER 2[1]

SOUTHEAST GREENLAND HIGH ACCUMULATION RATES DERIVED FROM FIRN CORES AND GROUND-PENETRATING RADAR

2.1. Abstract

Despite having only 14% of the Greenland Ice Sheet by area, the southeast sector has the highest accumulation rates, and therefore receives ~30% of the total snow accumulation. We present accumulation rates obtained during our 2010 Arctic Circle Traverse derived from three 50 m firn cores dated using geochemical analysis. We tracked continuous internal reflection horizons between the firn cores using a 400 MHz ground-penetrating radar (GPR). GPR data combined with depth-age scales from the firn cores provide accumulation rates along a 70-km transect. We followed an elevation gradient from ~2350 m to ~1830 m to understand how progressive surface melt may affect the ability to chemically date the firn cores and trace the internal layers with GPR. From the firn cores, we find a 52% (~0.43 m yr^{-1} w.e.) increase in average snow accumulation and greater interannual variability at the lower site compared to the upper

[1] This chapter is reprinted from *Annals of Glaciology*, with permission of the International Glaciological Society. Miège et al. (2013), Southeast Greenland high accumulation rates derived from firn cores and ground-penetrating radar. *Annals of Glaciology* 54(63), 322-332. The comments from Reinhard Drews and an anonymous reviewer improved the manuscript.

site. The GPR profiling reveals that accumulation rates are influenced by topographic undulations on the surface with up to 23% variability over 7 km. These measurements confirm the presence of high accumulation rates in the Southeast as predicted by the calibrated regional climate model Polar MM5.

2.2. Introduction

In recent decades significant air and ocean warming has been observed in Greenland (e.g. Meehl et al., 2007; Levitus et al., 2009), causing mass loss to accelerate on the ice sheet by surface melting, runoff, and ice discharge (e.g. van den Broeke et al., 2009; Rignot et al., 2011). The current Greenland ice sheet mass loss is estimated to range between 191 ± 23 Gt yr^{-1} and 240 ± 28 Gt yr^{-1} by combining NASA's Ice, Cloud land Elevation Satellite (ICESat) elevation measurements, firn compaction, and modelled surface density (Sørensen et al., 2011). The Gravity Recovery and Climate Experiment (GRACE) mission provided an independent check that confirmed the Greenland ice sheet loss of 219 ± 38 Gt yr-1 for 2002-2009 (Chen J.L. et al., 2011). In the last decade, about half of the mass loss is due to ice dynamics and the remaining half is due to surface mass-balance processes (van den Broeke et al., 2009). Surface mass balance for the Greenland ice sheet can be approximated by snowfall (accumulation) minus ablation, and its interannual variability over the 1957-2008 period is very large, with a standard deviation (σ) of 107 Gt yr^{-1} (Ettema et al., 2009).

Accumulation is the only mass input to the Greenland ice sheet, and its magnitude, spatial, and temporal distributions are poorly constrained, specifically in the southeast sector (e.g. Burgess et al., 2010). Measurement uncertainty of the accumulation

input to the ice sheet means that there is uncertainty in the total mass budget of Greenland. The mass budget needs to be estimated in order to understand ice-sheet behavior, which is a critical question. Since accumulation may increase with future warming (e.g. Meehl et al., 2007), reducing uncertainty in ice-sheet accumulation and better estimating the total mass budget is also critical. Recently, for the 2007-2009 time period, the southeast sector of the ice sheet has lost 172 ± 44 Gt yr^{-1}, which is a large part of the total mass loss over the whole ice sheet (Chen J.L. et al., 2011). However, an increase of accumulation rates that could offset this mass loss has not yet been observed.

We present snow accumulation rates derived from new firn cores and GPR measurements across poorly sampled areas of the southeastern Greenland ice sheet. The objectives of this study are to confirm the modelled high snow accumulation rates and to quantify the spatial and temporal variations in snow accumulation over the past 30 years. Below we introduce previous work on Greenland accumulation estimates and on GPR studies, which serve as the context for our study.

2.2.1. Accumulation-rate measurements

Accumulation rates over the Greenland ice sheet have been studied with a variety of methods. We discuss three of these methods, and highlight the need for additional in-situ measurements in the southeast sector of the ice sheet. In the first method, accumulation maps are generated by interpolating in-situ point measurements. Ice cores and snow pits, located in the upper accumulation area, are the most common observations. Along the coast of Greenland, the Danish Meteorological Institute maintains meteorological stations to measure accumulation from solid precipitation

minus evaporation. Benson (1962) and Ohmura and Reeh (1991) produced initial snow accumulation maps from these limited observations. Since then there has been increased spatial and temporal resolution of those accumulation maps using updated ice-core data, an increasing number of coastal weather stations, and more sophisticated interpolation techniques (Ohmura et al., 1999; Calanca et al., 2000; McConnell et al., 2001; Bales et al. 2001; Cogley, 2004; Bales et al., 2009). In the second method, regional climate models are used to simulate recent climate (typically since 1958 because of the availability of reliable reanalysis fields) of the ice sheet and also provide accumulation maps (Fettweis, 2007; Hines and Bromwich, 2008; Ettema et al., 2010; Lucas-Picher et al., 2012). However, all the different modelled snow accumulation outputs do not fully agree, and the lack of in-situ measurements in the southeast sector does not yet allow model comparison and validation (Rae et al., 2012). For example, the Regional Atmospheric Climate Model (RACMO2) (Ettema et al., 2009) modelled higher accumulation in Southeast Greenland compared to estimates from Box et al. (2006) using the Fifth Generation Mesoscale Model modified for polar climates (Polar MM5), or to Fettweis (2007) using the Modèle Atmosphérique Régional (MAR). A hybrid technique uses the discrepancies between regional climate model outputs and in-situ measurements to generate correction factors to produce calibrated accumulation maps (Box et al., 2006; Burgess et al., 2010). In the third method, accumulation maps are reconstructed by using meteorological reanalysis, for example ERA-40 (e.g. Hanna et al., 2006), 20CR (e.g. Hanna et al., 2011), and ERA-interim (e.g. Chen L. et al., 2011).

The southeast sector of the ice sheet represents only 14% of the total ice sheet area and accounts for 31% of total accumulated mass and 32% of annual accumulation

variability (Burgess et al., 2010). Only 2% of the available firn-core data of the Greenland ice sheet are found in the southeast sector, but no firn-core data are found below 2000 meters of elevation, where higher accumulation rates are predicted: over 2 m yr^{-1} water equivalent (w.e.) (Burgess et al., 2010) and reaching up to 5 m yr^{-1} w.e. (Rae et al., 2012). It is difficult to estimate accumulation close to the Southeast Greenland coast, where orographic precipitation dominates and topography is complex (e.g. Burgess et al., 2010; Lucas-Pichier et al., 2012). These studies emphasized the need for in-situ measurements to constrain climate models in this sector. In addition, Hanna et al. (2011) noted the lack of validation data for climate models and showed that uncertainties in Southeast Greenland accumulation are the greatest where accumulation rates are the highest, and where both accumulation and topographic gradients are significant.

2.2.2. Ground Penetrating Radar (GPR)

GPR allows us to capture spatial variability in accumulation over distances of tens to hundreds of km. Small-scale spatial variability in accumulation (~5-10 km), mostly due to snow redistribution and surface undulations, is not captured in point measurements from cores and is not taken into account in regional climate models with large grid cells (~5-25 km). The spatial variability of snow accumulation can be observed in GPR transects that show continuous internal reflection horizons (IRHs) (e.g. Arcone et al., 2004, 2005b; Dunse et al. 2008). IRHs at relatively shallow depths (<50 meters) are primarily due to density contrasts (e.g. Eisen et al., 2003; Arcone et al., 2005b). The isochronous nature of the IRHs has been confirmed using the depth-age scale from firn cores located at both ends of the GPR profile (Spikes et al., 2004; Eisen et al., 2006).

In the southeast sector of the ice sheet, for an elevation range between ~1840 m to ~2350 m, two major snow facies are found in our GPR profile. At elevations above 2000 m, the dry-snow facies is represented with no or little melt (~1-3 cm melt layers). At lower elevation, percolation facies are found where surface snow melts and travels downward through the snow pack until it refreezes (e.g. Benson, 1962), which likely produces vertical ice pipes and horizontal ice layers. Recent GPR studies in West Greenland documented the presence of ice layers within the firn (e.g. Parry et al., 2007; Dunse et al. 2008; Brown et al., 2011). These features complicate tracing of continuous IRHs in the firn depending upon melt intensity, spatial scale, and radar frequency. Dunse et al. (2008), using GPRs with frequency of 500 and 800 MHz, were able to track IRHs down to 10 m depth. Brown et al. (2011) found no correlation between IRHs and firn stratigraphy in the higher elevation part of the percolation zone in West Greenland and assumed the IRHs were multi-annual features (2-10 years) in the lower part of the percolation zone. These studies highlight the challenges in identifying isochronous IRHs from GPR profiles, and tracking them over many kilometers. However, all of these studies were conducted in regions where accumulation rates are relatively low compared to southeast Greenland. In the southeastern sector, high accumulation rates can prevent multi-annual melt features from dominating the GPR reflections at shallow depths (< 50 meters).

2.3. Arctic Circle Traverse 2010

Our study took place in the southeast sector of the Greenland ice sheet (Figure 2.1), where few field investigations have been reported, mostly due to high accumulation

rates in this region that discouraged long-term climate-data collection. We conducted the 500 km Arctic Circle Traverse 2010 (ACT-10) by snowmobile, starting at the DYE-2 station (now called "Raven") and moving toward the southeast ice-sheet margin. The data presented here were collected from 26 April to 9 May 2010, prior to surface melting that could have confounded propagation of the radar signal into the subsurface. ACT-10 repeated and extended the first ACT from 2004, which crossed the ice divide at the location called "Saddle" (Spikes et al., 2007). In 2010, three 50 m firn cores were collected (Table 2.1), and surface-based GPR was used to track continuous IRHs between the core sites. Our transect is located > 110 km away from the open ocean. Surface mean temperature is -19.3 ± 0.2 °C (Box et al., 2009), obtained from the NASA-SE weather station that is located ~55 km north from ACT10-C (see Figure 2.1). The mean wind speed recorded by the NASA-SE weather station is 5.5 m s^{-1} and its dominant direction has an azimuth of 315° (Steffen and Box, 2001), which is characteristic of the katabatic wind flow regime that is prevalent in this sector of the ice sheet. While GPR data were collected on the return segment of the traverse from ACT10-A to DYE-2 (250 km), this study focuses on the lowest elevation eastern segments between ACT10-A and ACT10-C (Figure 2.1) where accumulation rates have been predicted to be the highest (Burgess et al., 2010; Rae et al., 2012).

The ACT-10 traverse route covered a relatively slow-moving portion of the ice sheet. Observed surface velocities, for 2008-2009, are in the 50-100 m yr^{-1} range, between ACT10-C to ACT10-A (Rignot and Mouginot, 2012). We determined the flow-line direction based on surface-elevation contours from the DEM produced by Bamber et al. (2001); our GPR profile is approximately parallel to the current flow direction. The

average ice thickness along the ACT10-A to ACT10-C transect is 1520 ± 4.5 m (Leuschen and Allen, 2011). Here we assume that the observed structure of the IRHs is only due to variations in accumulation, and not due to ice dynamics. This simplification can be made because of the high accumulation in this area and the minimal internal deformation at these depths corresponding to a short period of time analyzed (1995-2010).

2.4. Methods

2.4.1. Firn Cores

Three 82 mm diameter firn cores (ACT10-A, -B, -C) were drilled with an ECLIPSE drill (designed by Icefield Instruments Inc.), starting 2 meters below the surface in a trench to allow room for core-barrel clearance. The upper 2 meters were sampled manually using the core barrel. In the field, ~1 meter core sections were labeled and bagged before being shipped frozen to the Desert Research Institute Ultra-trace Chemistry Laboratory. Then, the core sections were processed and analyzed for a broad range of elements and chemical species, which were used to develop a precise depth-age relationship and annual accumulation rates (Table 2.1). First, the cores were cut into rectangular samples, each ~1 m by ~35 mm by ~35 mm. The samples from each site were weighed, used for the depth-density profile, and then analyzed using a continuous flow analysis system with an effective depth resolution of ~10 mm (McConnell et al., 2002; Banta and McConnell, 2007; McConnell et al., 2007). This system is composed of two high resolution inductively coupled plasma mass spectrometers and a number of fluorimeters, spectrophotometers, and other instruments (Banta and McConnell, 2007). Indicators of continental dust (Al, Mg, Ca, Fe), sea salts (Na, Mg, Ca, S), industrial

pollution (Pb, Tl, Cd, S, nitrate), explosive volcanism (S), biomass burning (black carbon, ammonium, nitrate), and atmospheric photochemistry (hydrogen peroxide; H2O2) are used for annual layer counting since most, if not all, of the chemical proxies show pronounced annual cycles in concentration. In regions with high accumulation rates such as Southeast Greenland, H2O2 is often the preferred proxy because of its very distinct annual concentration cycle and consistent mid-winter minimum (McConnell and Bales, 2004). Here we relied primarily on the annual H2O2 cycle for annual dating but secondarily used chemical proxies to confirm annual-layer identification in the few cases of unclear H2O2 cycles. The most commonly used secondary proxy was the non-sea salt sulfur to sodium ratio (nssS/Na), which showed a very strong annual cycle due to the occurrence of anti-correlated annual cycles in the nssS and Na species. Over the southeast sector of the ice sheet, extensive summer melting, revealed by the presence of thick ice layers (> 10 cm), has the potential to disrupt firn stratigraphy. Accumulation from one year may percolate down and refreeze in a different annual layer, confounding water equivalence measurements using annual glaciochemical signals. However, in our study area, accumulation rates are generally high enough and percolating surface melt water penetrate less than the full depth of a given year's accumulation. Because of the multiple chemical parameters available and the high snow accumulation rate, the maximum dating uncertainty is estimated to be one year.

An annual depth-age relationship is deduced from chemistry-peak identification and, a posteriori, is used to test for isochronal accuracy in the GPR profile between two firn cores. Since the H2O2 peak does not occur at the exact beginning of the year, a fractional year, with 0.1 year resolution, is required to capture the full variability in snow

accumulation. To convert the snow depth to accumulation at each core site for each year, an exponential function is fit to the density profile (see section 3.3 for further details on density analysis).

2.4.2. GPS and GPS data

The GPR system used for ACT-10 was the Geophysical Survey Systems, Inc. (GSSI) SIR-3000 controller and a 400 MHz center frequency antenna, with an 800 MHz bandwidth. The vertical resolution for the dry Antarctic firn is estimated ~35 cm (Arcone et al., 2004; Spikes et al., 2004), which is less than the thickness between two annual layers in our study area. The sampling interval was set at 6 traces per second, 2048 vertical samples per trace. As the expedition moved across the ice sheet at ~ 3 m s^{-1}, the deduced trace spacing is ~ 0.5 m. In addition, to increase the signal-to-noise ratio, an initial stacking of 6 traces was performed. A time-dependent gain was used to compensate for signal attenuation by the firn. The time window was 500 ns, with 2048 samples/trace giving a sampling interval of ~0.24 ns, with an average penetration depth of ~45 m.

In post processing, additional horizontal spatial averaging was done by stacking 8 traces, in addition to the original stacking of 6 traces in the field, thus each final trace has been averaged from 48 initial traces. This spatial averaging aims to increase the signal-to-noise ratio and minimize the influence of layer variations and cm-scale vertical ice layers present in the percolation zone, as described by Humphrey et al. (2012).

Coupled to the GPR measurements, a Trimble R7 geodetic-quality Global Positioning System (GPS) receiver was used to track the location of the GPR profile

every 5 seconds, corresponding to one point for ~ 15 meters (for a travel speed ~ 3 m s^{-1}). The GPS receiver was mounted on the snowmobile towing the GPR sled. Each GPR trace is georeferenced using processed GPS data that have been interpolated based on the time when GPR data collection began (obtained from the kinematic GPS receiver) and the trace acquisition rate. GPS data processing was done using the Canadian Spatial Reference Service - Precise Point Positioning (CSRS-PPP). This processor uses GPS orbit and clock information to enhance positioning precisions in the International Terrestrial Reference Frame (ITRF) via a kinematic processing mode. Uncertainties in the GPS positions are given within one standard deviation for the ACT10-A to ACT10-C transect. The maximum standard deviations are 0.07 m for latitude and longitude (~0.02 m in average) and 0.22 m for elevation (~0.06 m in average).

2.4.3. Accumulation-rate calculation

Depth-age profiles from three firn cores collected along the GPR profile (Figure 2.2) are used to confirm that the IRHs are isochrones (see section 4.3 for details on isochronal accuracy). Only the most prominent IRHs, which were the easiest to trace in the GPR profile, were used for digitizing (Figure 2.2). Manual layer picking was preferred because it provided better operator control when IRHs were laterally discontinuous. While manually picking, if a short lateral discontinuity (<100 meters) was observed in the GPR profile, the operator used the two IRHs located directly above and below the tracked IRH as a guide to estimate the tracked IRH depth. Three possible explanations for the partial disruption of an IRH include: 1) topographic undulations on the surface of the ice sheet may result in more pronounced folds at depth (Figure 2.2),

which can induce a two-way-travel time (TWT) phase delay of as much as half the wavelength for only a 0.4° incidence angle for a given dip that reduces return strengths and causes destructive interference (Spikes et al., 2004). 2) The presence of ice layers, due to heterogeneous meltwater infiltration, may disrupt the lateral continuity of an IRH (see section 2.4.2 for details). 3) The surface roughness can cause vertical artifacts, for example, when the radar sled lost contact with the snow surface due to sastrugi, making the IRHs more difficult to track.

For an individual digitized radar horizon, several steps are required to obtain accumulation rates. At each firn-core site, the conversion of the radar TWT to distance below the surface is computed based on the core-density profile, through the relationship between velocity in the firn v_f and firn density profile $\rho(z)$ (Kovacs et al., 1995):

$$v_f = c/\sqrt{\varepsilon'} \qquad (2.1)$$

$$\varepsilon' = (1 + 0.845\rho(z))^2 \qquad (2.2)$$

where c represents the speed of light in a vacuum, and ε' is the real part of the dielectric constant (permittivity).

The density profiles for the ACT-10 firn cores, represented in Figure 2.4, were derived from ~1 m sections of the firn core (section 2.3.1). We used an exponential fit to smooth and interpolate the density profile with depth:

$$\rho(z) = \rho_s + \alpha_1 * e^{(\beta_1 * z)} + \alpha_2 * e^{(\beta_2 * z)} \qquad (2.3)$$

where ρ_s is the density at the surface, α and β are the fitting parameters, and is the depth of the profile (Hörhold et al., 2011).

This fitted density profile is used for the TWT-depth conversion. Estimated snow depth for the radar signal is known at each core site and then linearly interpolated along

the transect for each radar trace. To account for all three firn cores, we made two linear interpolations of the density profile, one between ACT10-A and ACT10-B and the second between ACT10-B and ACT10-C. To determine the snow accumulation rate between two time periods, the depth of the upper horizon is subtracted from the depth of the lower horizon. Then, the calculated snow thickness is converted to a water equivalent depth using the interpolated density profile for each trace.

For defining each time period, absolute ages are assigned to an IRH from the three firn cores depth-age scale. A conventional way to express the age of a tracked isochrone is to use the calendar year, reasonable in areas with low accumulation where isochrones are closer together (e.g. Spikes et al., 2004). In the southeast sector of the ice sheet, high accumulation rates allow us to express the age of each IRH in fractional years, increasing the precision of the accumulation-rate calculations. The GPR-derived annual accumulation rates depend primarily on the age of each tracked IRH. The estimated seasonality (fractional year) for different IRHs (shown in Figure 2.2), is not consistent from one horizon to another, varying from 0.2 to 0.7 years.

2.5. Results

2.5.1. GPR-derived accumulation rates

Mean accumulation rates, derived from the firn cores, at each core site are 1.26, 1.09 and 0.83 m yr^{-1} w.e. for ACT10-A, ACT10-B, and ACT0-C, respectively (Table 2.1). They are in agreement with the accumulation rates estimated by the calibrated Polar MM5 on the pixel corresponding to each core site (Table 2.1). Accumulation rates are calculated along the traverse from ACT10-A to ACT10-C, from the radar profile (Figure

2.2) over different time periods (Figure 2.3). They are smoothed to remove digitizing noise with a moving-average filter that was 20 traces wide. The accumulation rates presented for each period highlight an increasing trend in accumulation as elevation decreases, closer to the southeast ice margin. On average, a 52% increase in accumulation (+0.43 m yr^{-1} w.e.) is observed along the 70-km line between ACT10-C to ACT10-A for the 1992.2 to 2008.5 time period. The spatial variability in accumulation rates over this time period has a standard deviation of 0.13 m yr^{-1} w.e. A maximum local spatial variability in accumulation is found over a 7 km distance with 0.24 m yr^{-1} w.e. representing 23% of the annual mean (Figure 2.3). As for temporal variability, an increase of accumulation may be expected in the last decades due to the increase of surface temperature (Box et al., 2012). However, we found no significant trend in accumulation rate from the firn cores over their respective time periods spanning the last 25-35 years.

The wide range (~ 0.26 m yr^{-1} w.e. on average) of accumulation rates between the different time periods, shown in Figure 2.3, is mainly due to the presence or absence of an anomalous accumulation year. For example, 2003, is known to be a high accumulation year (Box et al. 2005). The high accumulation over the 2002.2-2006.2 period is primarily driven by the anomalously high accumulation of 2003. In contrast, the 2006.2-2008.5 period is the lowest accumulation period.

2.5.2. Influence of ice layers

Firn-core dating and GPR-derived accumulation rates are challenged by the increase of surface melt as meltwater penetrates within the firn layer and refreezes. For

the firn-core dating, at core sites such as ACT10-A (1825 m), accumulation rates are high (1.26 m yr^{-1} w.e.) and melt water penetrates less (~20 %) than the full depth of the present year's accumulation. For the IRH tracking on the GPR profile, the spatial variation of the density is difficult to estimate in the percolation zone because of heterogeneous water infiltration at small scales (~1-5 m) (Humphrey et al., 2012). The presence of thicker ice layers at lower elevation site (ACT10-A) is illustrated in Figure 2.4 where the ~1 m density measurements deviate the most from the exponential fit. It becomes more difficult to track IRHs at greater depths (35-45 m) as the surface elevation decreases and thicker ice layers become more common. On the contrary, near ACT10-C, we find more laterally-homogenous IRHs with few ice layers (Figure 2.2). Understanding how firn stratigraphy affects the GPR signal is beyond the scope of this study, even if it remains an important upcoming challenge while mapping annual accumulation rates. These issues have been discussed for West Greenland by Brown et al. (2011).

2.5.3. Uncertainty estimates

Different sources of uncertainties affect the estimation of the IRH depth and therefore the estimation of GPR-derived accumulation rates.

1. The vertical density profile at each core site is estimated from the mass of ~1 m firn-core segments (Figure 2.4). To avoid a bias from a single core segment dominated by ice layers, we use an exponential fit to the density profile. A fitted density profile is needed, specifically at lower elevation sites where intense melt layers are interspersed between lower density firn producing a sporadic depth-density series (Figure 2.4). The lowest coefficient of determination (r^2) between the exponential fit and the density-depth

data is 0.87 at ACT10-A. The root mean square error (RMSE) for ACT10-A, ACT10-B, and ACT10-C are 37.63, 26.12, and 12.21 kg m^{-3}, respectively. A higher RMSE is expected for the presence of thick ice layers, with the original data deviating more from the fitted profile. Using an averaged RMSE (25.3 kg m^{-3}), deviating at 4% from an averaged density, we obtain an average depth uncertainty of ±24 cm from the surface to the depth of the deepest tracked IRH (~35 m).

2. In addition to the vertical exponential interpolation of density, an uncertainty is introduced while interpolating the density profile horizontally between two core sites. Snow stratigraphy and implied density are spatially variable at a meter scale, specifically in the percolation zone with the presence of heterogeneous infiltration forming ice layers and potential vertical channels by refreezing. By interpolating the density profile between two firn-core sites and stacking radar traces, the uncertainties are minimized. While comparing the fitted density profiles, the maximum standard deviation obtained is 31.18 kg m^{-3} between the ACT10-A, ACT10-B, and ACT10-C fitted density profiles, yielding an average depth uncertainty of ± 28 cm.

3. Layer picking and digitizing are performed manually, and therefore its uncertainty is difficult to quantify. Most of the IRHs observed are made of distinct wavelets with consistent phase polarity sequence: negative/positive/negative, corresponding to a 1.5 wavelet cycle (Arcone et al., 2005a). Deduced from the 1.5 cycle wavelet length, the GPR vertical resolution (separation of two IRHs) is ~ 35 cm for the dry polar firn, with the wavelet response characterizing a single interface (Arcone et al., 2004). Along the ACT-10 transect, assuming that we are tracking the same IRH, the maximum 1.5 cycle wavelet lengths were ~ 10 vertical samples, about 2.5 ns or ~25 cm,

which is less than the 35-cm vertical resolution of the GPR. Ideally, the high accumulation rates in this area create sufficient vertical separation between annual layers that it becomes possible to track an IRH for most years. Even for the lower accumulation site, the minimum annual firn layer thickness is 73.2 cm, more than twice the vertical resolution of the GPR.

4. The age of an IRH is given at ±1 year from the firn-core chemistry dating. Then, despite this 1-year uncertainty in the absolute age, the isochronal accuracy of the IRHs is determined at the three ACT-10 cores sites. The age of a continuous IRH is determined at each end of the radar profile, using the depth-age scales from the firn cores. The difference between the two years at each side of the radar profile (ACT10-A and ACT10-C) is calculated to give the precision of this isochronal tracking. The firn core between the two end points (ACT10-B) is used to confirm the result. The mean difference of the IRHs tracked for this GPR profile is ± 0.14 years with a maximum difference of 0.37 years, indicating that the IRHs are continuous and isochronal.

Finally, we estimate an average total depth uncertainty of 37 cm from the density vertical uncertainty (point 1 above) and the density horizontal uncertainty (point 2 above), using an orthogonal error propagation law, giving a ~20% (± 0.23 m w.e.) uncertainty in the GPR-derived accumulation rates for an averaged density (640 kg m^{-3}). We didn't include the core dating uncertainty in this estimation, given the fact that each tracked IRH ends up with the almost same age (point 4 above) at the three firn-core sites along the profile and we are estimating the uncertainty of the accumulation rates derived from the technique of GPR interpolation between dated cores.

2.6. Discussion

2.6.1. Comparison with a regional climate model

The ACT-10 accumulation rates are compared to modelled accumulation-rate output from Polar MM5, which was calibrated to existing firn-core data by Burgess et al. (2010). Calibrated Polar MM5 is favoured in this study because it accounts for orographic precipitation that other modelled accumulation outputs underestimate (Burgess et al., 2010). The closest grid cells to the traverse line are used to produce an accumulation profile between ACT10-A and ACT10-C. Here, we focus on two IRH intervals with low and high accumulation rates (years 2006.2 – 2008.5, and years 2002.2 – 2006.2, respectively) and an interval from the bottom IRH to the surface to provide a long-interval average accumulation record (years 1992.5 – 2008.2). These three periods show spatial and temporal differences in accumulation from the GPR profile (Figure 2.5). For the 1992.5 – 2008.2 period, calibrated Polar MM5 accumulation rates are in agreement with our fitted GPR-derived accumulation rates (Figure 2.5). However, the 24-km grid resolution of the model does not resolve the ~10 km and smaller-scale variation in accumulation. Examining a shorter period from 2002.2-2006.2, the calibrated Polar MM5 underestimated accumulation by ~20% (~0.24 ± 0.16 m yr^{-1} w.e.) at the highest accumulation (and lowest elevation) site (Figure 2.5). The linear fit to the ACT-10 accumulation is steeper than the fit to calibrated Polar MM5. We think this is a consequence either of the limited horizontal resolution of Polar MM5 (24 km) and/or the calibration methods used by Burgess et al. (2010). Yet, for the period 2006.2 – 2008.5, calibrated Polar MM5 overestimates accumulation. The maximum RMSE associated with the GPR-derived results represents 0.17 m yr^{-1} w.e. for the 2002.2 – 2006.2 period. This

value is in agreement with calibrated Polar MM5 error estimate, which is 0.16 m yr^{-1} w.e. along the entire traverse route, verifying the model prediction over the southeast ice sheet.

2.6.2. Local topographic influence

Accumulation rates are higher in topographic depressions (shaded bars in Figure 2.3). Some combinations of wind redistribution of snow and water-vapor flux likely create this accumulation pattern. Over the Antarctic ice sheet, King et al. (2004) showed that topography, snow precipitation, wind direction, and speed resulted in significant snow redistribution that lead to high spatial variability in snow accumulation over distances as short as a few kilometers. The degree to which surface slope and accumulation rate correlate depends on how the GPR profile is oriented relative to the direction of the dominant wind (Spikes et al., 2004; Arcone et al., 2005b). In our study region, wind direction is essentially from ~315° (from the NASA-SE station), which is on average parallel to the GPR profile. But, for the last 10 km of the study transect (toward ACT10-C), the main wind direction may diverge up to ~30° with the GPR profile direction. This difference could be an explanation of amplitude differences and a slight phase shift between the accumulation rates and the surface-slope derivative (Figure 2.6). The second derivative of the surface-elevation profile yields the topographic curvature corresponding to the convexity or concavity of the terrain. Positive values represent concavity, where the terrain has a local depression, and negative values represent convexity, where the terrain has a local high (Figure 2.6). The GPR-derived accumulation rates were detrended to remove the overall increasing accumulation rate along the studied

transect. This convexity/concavity index shows a good agreement with the accumulation pattern. Higher accumulation correlates with concavity (positive values), with a correlation coefficient (r) of 0.58 (Figure 2.6).

Although the amplitude and local maxima/minima shifts between accumulation values and the convexity/concavity of the terrain do not correlate perfectly along the entire profile, it is generally true that the GPR-derived accumulation rates are lower if the surface is convex and higher if it is concave. This pattern is consistent with wind scouring from the tops of undulations and redeposition into adjacent depressions (or else there is less scouring in depressions). Here, scouring refers to some combination of sublimation loss and wind redistribution.

2.6.3. Temporal variability

Temporal variability is investigated here using only the firn cores and is compared to the calibrated Polar MM5 (Table 2.1). We find that the GPR data do not clearly resolve annual accumulation rates because of the difficulties tracking IRHs due to the increasing presence of ice layers as elevation decreases. The agreement between the averaged firn-core accumulation rates and the accumulation rates from calibrated Polar MM5 over corresponding time periods is characterized by correlation coefficients (r) ranging from 0.625 to 0.803 and RMSE ranging from 0.11 to 0.25 m yr^{-1} w.e. (Figure 2.7). At the lowest elevation core site, ACT10-A, the calibrated Polar MM5 underestimated the mean accumulation rate by 5% (0.06 m yr^{-1} w.e.).

Atmospheric reanalysis and ice-core data indicate an increase in snow accumulation rates on the ice sheet since 1958 (Hanna et al., 2008; Box et al., 2012). But,

no significant increasing temporal trends were identified over the length of our ACT-10 firn-core records. The ACT-10 cores are less than 40 years in duration and seem dominated by high interannual variability (Figure 2.7). An observation from Figure 2.7 reveals the presence of year 2003 as a strong positive accumulation anomaly, in ACT-10 firn cores. This high accumulation year was related to persistent low atmospheric pressure on the southern tip of the ice sheet from September 2002 to April 2003 (Box et al., 2005). During this time period, large accumulation events are recorded by automatic weather stations, such as NASA-SE (located ~ 55 km north of ACT10-C). For example, one event deposited 65 cm of fresh snow over 7 hours followed by strong winds compacting the snowpack down to 40 cm (Box et al., 2005). High accumulation years like 2003 have implications for the following summer melt rates by maintaining a higher albedo, minimizing the impact of observed warming (e.g., Box et al., 2009) on increased melting.

The interannual variability observed in the firn cores is high, especially at the lowest elevation site (ACT10-A) with a standard deviation of 0.373 m yr^{-1} w.e. (~30% of the mean). The calibrated Polar MM5 data at the corresponding grid cells have a standard deviation of 0.152, 0.123, and 0.084 m yr^{-1} w.e. for ACT10-A, ACT10-B, and ACT10-C, respectively (Table 2.1). This interannual variability in the southeast is large enough to significantly impact the total mass budget of the entire ice sheet, accounting for ~30% of the ice sheet total interannual variability in accumulation (Burgess et al., 2010).

However, the modelled accumulation rates show ~50% less variability compared to the firn cores. The Polar MM5 interannual variability is lower than the firn-core observations because of the month-long model integration (Burgess et al., 2010),

producing ~30% lower interannual variability in Polar MM5 than in earlier configurations in which daily integrations are made (Box et al., 2006). In addition, this interannual variability discrepancy between the firn core and the model can be explained by the large model horizontal grid resolution compared to the point measurements of the firn cores. At the firn-core site, spatial variations due to wind redistribution result in incoherent "glaciological noise" (Mosley-Thompson et al., 2001) in the firn-core data that is also not captured by a 24 km grid-cell of Polar MM5. To reduce this incoherent noise, a common practice is to use multiyear average filters (Banta and McConnell, 2007). However, despite minimizing incoherent noise, these filters eliminate some of the high-frequency coherent signal, such as the presence of anomalous high accumulation years, e.g. 2003. We find correlation coefficient values between firn cores of $r = 0.84$ for ACT10-A vs. ACT10-B; $r = 0.75$ for ACT10-A vs. ACT10-C; and $r = 0.88$ for ACT10-B vs. ACT10-C, all associated with <10-5 p-values, which are statistically significant (at $p < 0.01$), for common time periods. These relatively high correlation coefficients ($r > 0.75$) between firn core time series support that both the firn cores and calibrated Polar MM5 capture a common climate.

Comparing a regional accumulation record with a large-scale atmospheric circulation pattern is a commonly-used process to identify precipitation source regions as well as understanding how the observed interannual variability may affect the annual surface mass-balance estimates (e.g. Mosley-Thompson et al., 2005). The North Atlantic Oscillation (NAO), a dominant mode of regional atmospheric variability around Greenland, exerts a significant yet complex spatial and temporal influence on Greenland precipitation (e.g. Appenzeller et al., 1998; Hutterli et al., 2005; Mosley-Thompson et al.,

2005; Banta and McConnell, 2007). The NAO is the difference in atmospheric pressure at sea level between the Icelandic Low pressure system and the Azores High pressure system, and it indicates changes in the intensity and direction of the North Atlantic storm tracks (Hurrell, 1995). The influence of the NAO on accumulation varies spatially and temporally for the Greenland ice sheet (Mosley-Thompson et al., 2005). Hutterli et al. (2005) identified four regions over the Greenland ice sheet with distinct sources of accumulation variability with only the western sector of the Greenland ice sheet that presents an inverse relationship with a NAO pattern. The other regions are affected by other large-scale patterns, like the southeast region, where accumulation is positively correlated with a high-pressure anomaly over the Greenland Sea.

Despite the short time span of the cores (last 25 to 35 years), a comparison between the firn-core records and the December-March NAO index of Hurrel (1995), consistent with Box (2006), shows a negative correlation. Using this seasonal NAO index gives a ~0.2 higher correlation compared to using the annual NAO index. While the correlation coefficients are low: r = -0.21 for ACT10-A, r = -0.25 for ACT10-B, and r = -0.38 for ACT10-C; their p-values (1-p ranging from 0.68 to 0.98) suggest that the captured signal is real. Mosley-Thompson et al. (2005) demonstrated that the use of a temporal smoothing filter (5-year triangular filter) improved the correlation coefficients. Applying this filter to the ACT-10 firn-core data, we find a similar result with higher correlation coefficients: r = -0.40 for ACT10-A, r = - 0.33 for ACT10-B, and r = -0.59 for ACT10-C. These low initial correlations may imply that the origin of moisture source in the southeast is not explained by the NAO alone.

2.7. Conclusions

The presence of three new annual accumulation records from our ACT-10 cores, as well as spatial accumulation rates from our GPR profile provide necessary in-situ measurements in the southeast sector of the Greenland ice sheet. Since the accumulation rate in our study site was greater than the vertical-resolution of our GPR system, we expected to be able to track annual reflection horizons in our GPR profile. While this was possible at higher elevations along our transect, we found that this was not always possible at lower elevations because the presence of >10-cm thick melt layers likely caused spatial discontinuity of IRHs.

The obtained in-situ measurements of accumulation would contribute to further validation efforts and help reduce Greenland accumulation model uncertainties in the southeast sector, where accumulation rates are the highest on the ice sheet. Radar profiling along a 70-km transect between our firn cores indicates a 52% (~0.43 m yr-1 w.e.) increase in accumulation from the higher elevation site (ACT10-C at 2350 m) to the lower site (ACT10-A at 1830 m). Maximum spatial variability estimated from the GPR, which is not captured by widely-spaced single-point measurements such as firn cores, is found to be 23% (up to 0.24 m yr-1 w.e. in this case) over distances as short as 7 km. This shows that firn-core data alone may not be adequate to infer regional accumulation rates, as local topography and wind redistribution must be considered. Surface convexity is found to be a useful predictor of undulation-scale accumulation variability, with the highest local accumulation rates associated with local depressions (concavities).

No significant temporal trend exists in the firn-core data. The mean accumulation rates, of up to 1.26 m yr-1 w.e., from the firn cores are in a good agreement with

calibrated Polar MM5 output, but the amplitude of the interannual variability observed in firn cores is substantially reduced in the model output; interannual variability in the calibrated Polar MM5 is ~50% less than measured in the firn cores. This is mainly due to a combination of "glaciological noise" in the firn-core data, and the smoothing effect of using different model-integration strategies for Polar MM5. Further, the discrepancy in the interannual-variability amplitude, for the calibrated Polar MM5 and the firn cores, increases toward the coast as accumulation rates increase.

The three ACT-10 firn-core accumulation records, strongly inter-correlated ($r > 0.75$), are likely to be affected by a common climate. Initial comparisons between the accumulation records and seasonal NAO indices show low correlations, implying that the accumulation in Southeast Greenland for the last decades is likely not controlled by the NAO alone.

2.8. Acknowledgements

We thank the Chief Editor, Gwenn Flowers, and the Scientific Editor, Catherine Ritz, for comments and handling of our manuscript. We thank Reinhard Drews and an anonymous reviewer for many insights and comments that substantially improved the manuscript. This work was supported by National Science Foundation Office of Polar Programs Award ARC-090946 and ARC-0909499. Clément Miège is funded under the NASA Earth and Space Science Fellowship program. We thank Susan Zager and others at CH2MHill Polar Field Services for logistical assistance and Terry Gacke and others at IDDO for ice drilling expertise and enthusiastic help with the expedition.

Table 2.1: ACT-10 firn cores. Mean annual accumulation rates are given with one standard deviation for firn cores and for calibrated Polar MM5, representing the range of the annual values in each time series. Calibrated Polar MM5 and firn core mean accumulation rates have been calculated from the bottom age of each firn core until 2008.

NAMES	Latitude	Longitude	Elevation (m)	Length (m)	Mean accumulation (m yr^{-1} w.e.) Firn cores	Polar MM5	Time span (yr)
ACT10-A	65°41'N	41°28'W	1825	47	1.26 ± 0.731	1.19 ± 0.298	1985 - 2010
ACT10-B	65°46'N	41°52'W	1999	49	1.09 ± 0.519	1.08 ± 0.241	1980 - 2010
ACT10-C	65°59'N	42°46'W	2354	49	0.83 ± 0.310	0.83 ± 0.165	1973 - 2010

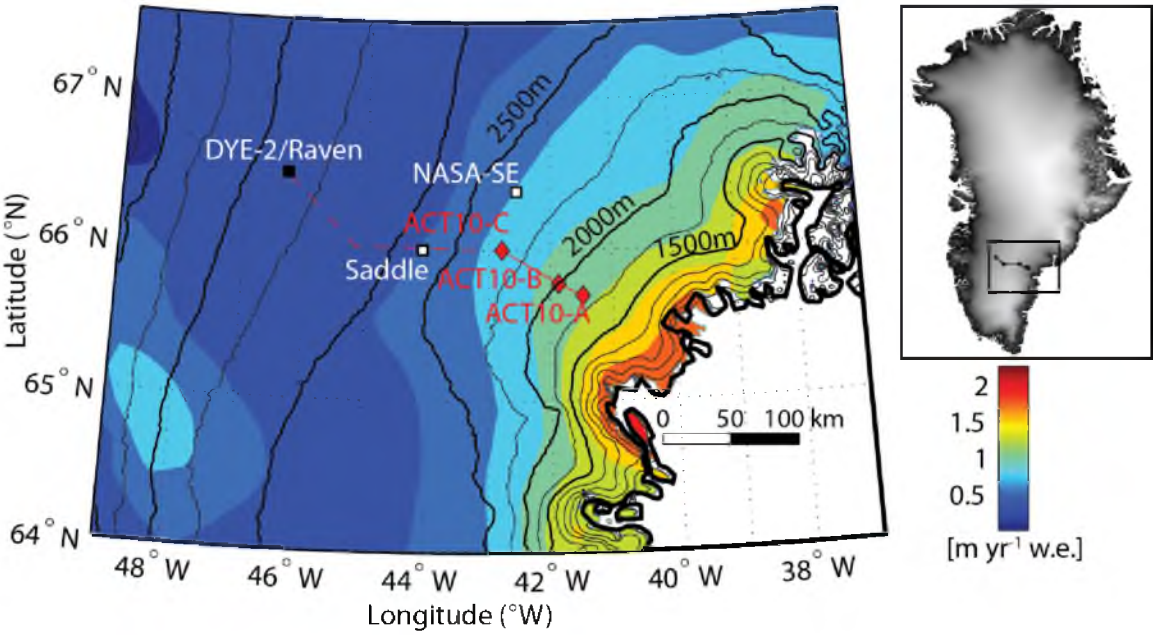

Figure 2.1: Study site in Southeast Greenland with the ACT-10 route, which started at DYE-2 (black square). The red solid line represents the 70 km GPR data presented in this paper. The red dashed line represents the rest of the traverse route, which is not discussed here. The red diamonds are the locations of firn cores drilled as part of this project. The black lines are elevation contours with 250 m spacing from Bamber et al. (2001). NASA-SE and Saddle weather stations (see text) are represented by white squares. The background is the mean (1958-2008) accumulation rates modelled by Burgess et al. (2010) in m yr^{-1} w.e.

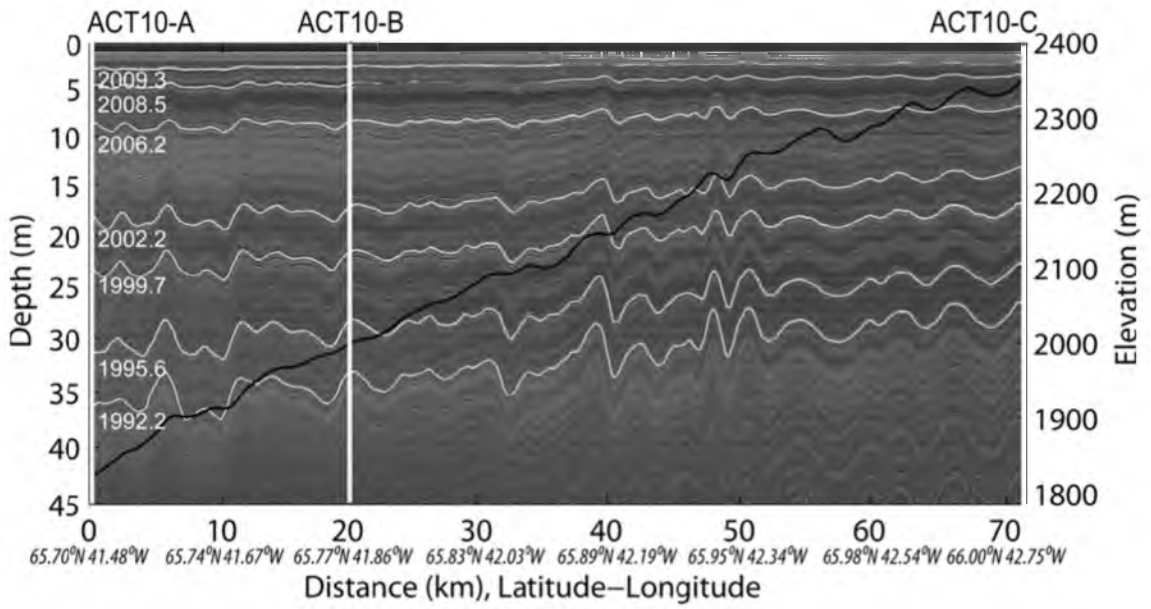

Figure 2.2: GPR profile between ACT10-A and ACT10-C. A total of seven different IRHs (white dashed lines) are tracked for the entire radar profile. Each isochronous layer is dated using the depth-age scale at the three core sites and an averaged fractional age is obtained (white characters). Firn-core sites are represented by white vertical lines. ACT10-A and ACT10-C are on the left and right side of the profile, respectively. The depth scale represented on the vertical axis is calculated from the TWT-depth conversion (see section 3.3) for the ACT10-A firn core. The black line corresponds to the elevation profile associated to GPR profile.

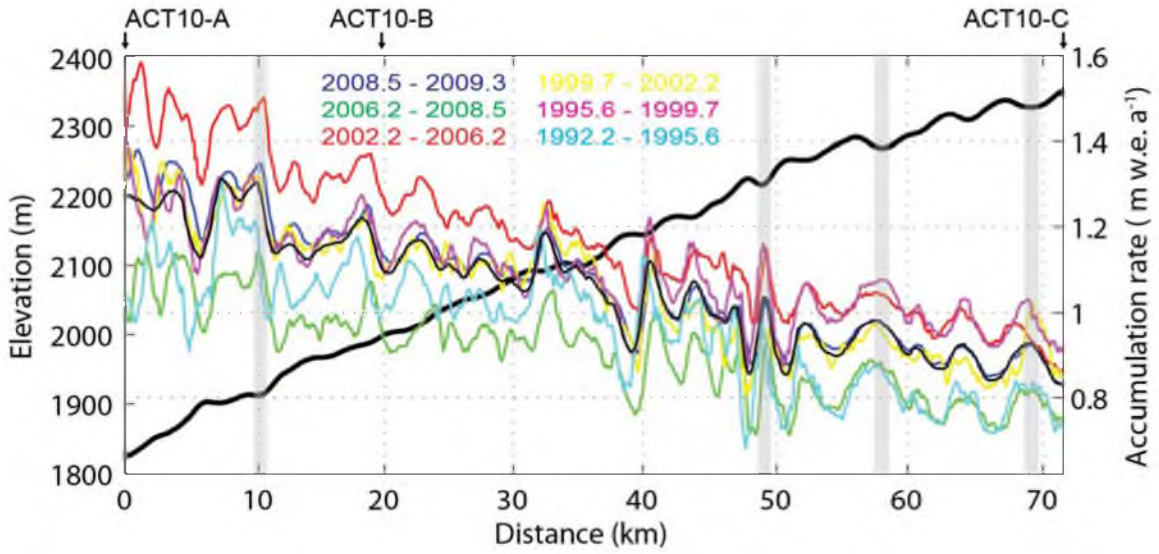

Figure 2.3: Temporal and spatial variability in snow accumulation rates for six time periods revealed by GPR profiling between firn cores ACT10-A and ACT11-C, the thin black line represent the averaged-accumulation for the whole time period 1992.2 – 2009.3. The thick black line represents the elevation profile. The four gray shaded vertical bars illustrate four examples, along the GPR profile, of the presence of high accumulation peaks located in topographic depressions, highlighting the role of wind redistribution of snow.

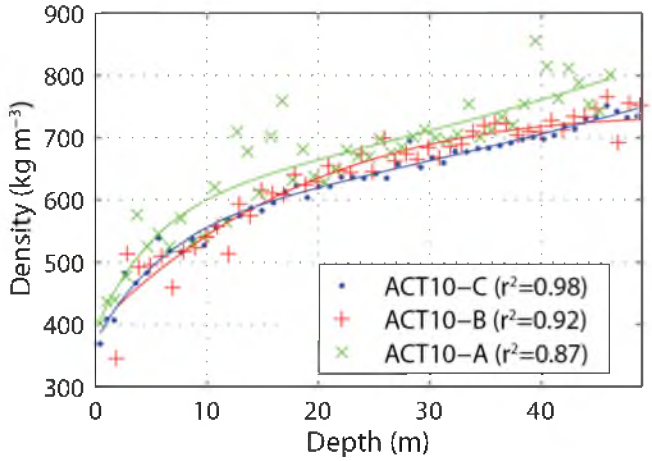

Figure 2.4: ~1 m density measurements made at each firn-core site associated with colored lines representing the exponential fit. Fitted-density profiles are used for the TWT-depth conversion and accumulation-rate estimation in water equivalent (section 3.3). Coefficients of determination (r^2) are associated for each firn-core site. Lower coefficients of determination indicate that short-scale density fluctuations increase.

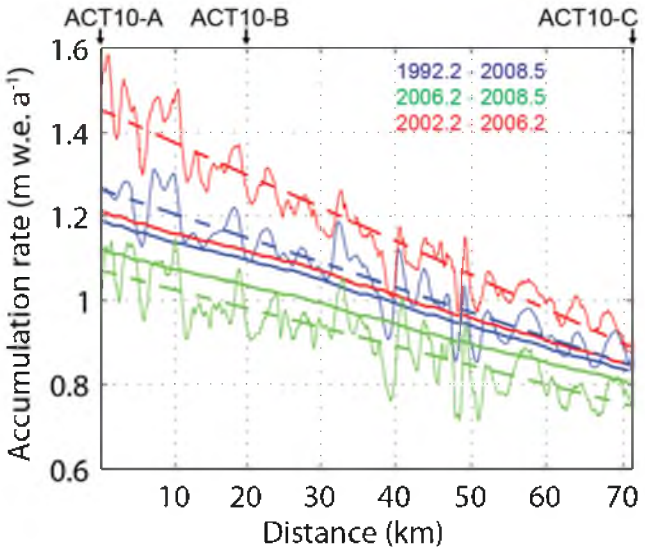

Figure 2.5: Comparison between calibrated Polar MM5 (solid line) and accumulation rates derived from GPR (solid curves), along the GPR transect, for three different time periods, showing the accumulation-rate variability. The periods chosen are the lowest (green) and highest (red) mean accumulation rates and the long-term average (blue). A linear fit (dashed line) is added for each period. The same time span is used for calibrated Polar MM5 and GPR accumulation rates.

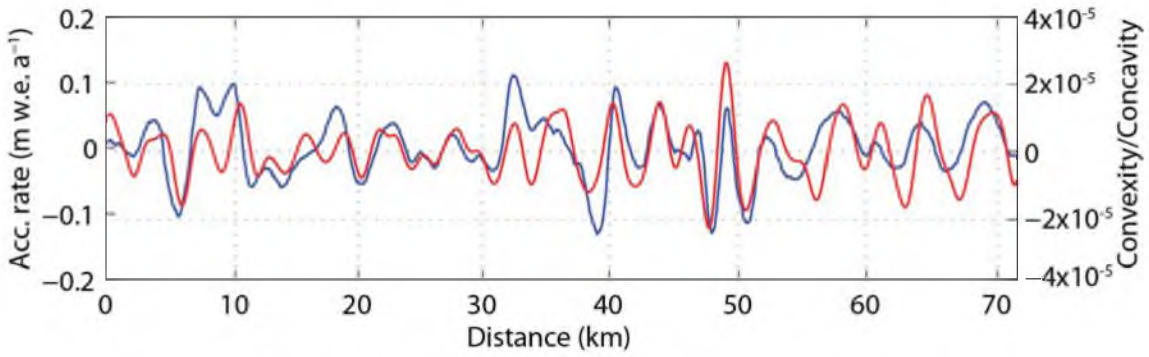

Figure 2.6: Comparison between convexity/concavity index (red) and the detrended annual accumulation rate from the radar (blue) for the ACT10-A to ACT10-C transect. To calculate the convexity/concavity index, outliers were removed and a Gaussian smoothing function was applied, with 1 σ width of the Gaussian equal to ~ 0.2 km (σ = 70.5 GPR horizontal traces).

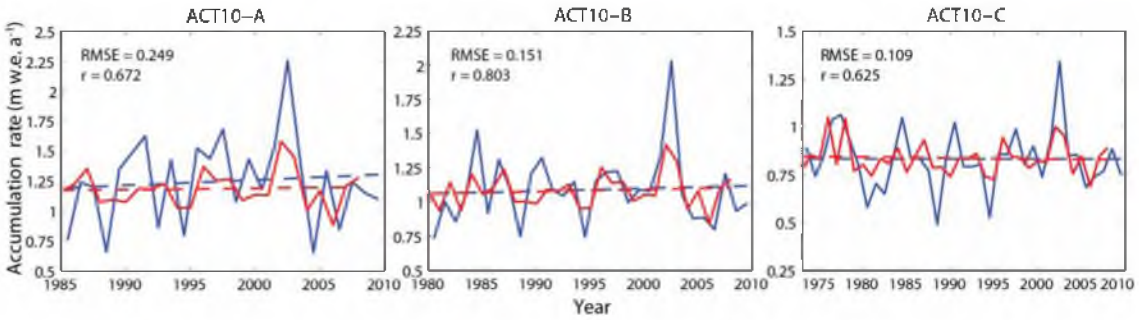

Figure 2.7: Comparison of the temporal variation of accumulation between Polar MM5 (red) and firn cores (blue), for each core site, from low elevation to high elevation, ACT10-A, ACT10-B, and ACT10-C, respectively. Dashed lines present a linear fit to the data for Polar MM5 (red) and firn cores (blue). There is a change in vertical scale between cores.

2.9. References

Appenzeller, C., J. Schwander, S. Sommer, and T. F. Stocker (1998), The North Atlantic Oscillation and its imprint on precipitation and ice accumulation in Greenland, *Geophys. Res. Lett.*, *25*(11), 1939–1942, doi:10.1029/98GL01227.

Arcone, S. A., V. B. Spikes, G. S. Hamilton, and P. A. Mayewski (2004), Stratigraphic continuity in 400 MHz short-pulse radar profiles of firn in West Antarctica, *Annals of Glaciology*, *39*(1), 195–200, doi:10.3189/172756404781813925.

Arcone, S. A., V. B. Spikes, and G. S. Hamilton (2005a), Phase structure of radar stratigraphic horizons within Antarctic firn, *Annals of Glaciology*, *41*(1), 10–16, doi:10.3189/172756405781813267.

Arcone, S. A., V. B. Spikes, and G. S. Hamilton (2005b), Stratigraphic variation within polar firn caused by differential accumulation and ice flow: Interpretation of a 400 MHz short-pulse radar profile from West Antarctica, *Journal of Glaciology*, *51*(174), 407–422, doi:10.3189/172756505781829151.

Bales, R. C., J. R. McConnell, E. Mosley-Thompson, and B. Csatho (2001), Accumulation over the Greenland ice sheet from historical and recent records, *Journal of Geophysical Research D: Atmospheres*, *106*(24), 33813.

Bales, R. C., Q. Guo, D. Shen, J. R. McConnell, G. Du, J. F. Burkart, V. B. Spikes, E. Hanna, and J. Cappelen (2009), Annual accumulation for Greenland updated using ice core data developed during 2000-2006 and analysis of daily coastal meteorological data, *Journal of Geophysical Research*, doi:10.1029/2008JD011208

Bamber, J. L., S. Ekholm, and W. B. Krabill (2001), A new, high-resolution digital elevation model of Greenland fully validated with airborne laser altimeter data, *J. Geophys. Res.*, *106*(B4), PP. 6733–6745, doi:200110.1029/2000JB900365.

Banta, J. R., and J. R. McConnell (2007), Annual accumulation over recent centuries at four sites in central Greenland, *J. Geophys. Res.*, *112*, 9 PP., doi:200710.1029/2006JD007887.

Benson, C. S. (1962), *Stratigraphic studies in the snow and firn of the Greenland Ice Sheet. U.S. Snow, Ice and Permafrost Research Establishment*, U.S. Snow, Ice and Permafrost Research Establishment Research Rep.

Box, J., L. Yang, J. Rogers, D. Bromwich, L.-S. Bai, K. Steffen, J. Stroeve, and S.-H. Wang (2005), Extreme precipitation events over Greenland: Consequences to ice sheet mass balance, in *85th AMS Annual Meeting, American Meteorological Society - Combined Preprints*, pp. 3981–3984.

Box, J. E., D. H. Bromwich, B. A. Veenhuis, Le-Sheng Bai, J. C. Stroeve, J. C. Rogers, K. Steffen, T. Haran, and Sheng-Hung Wang (2006), Greenland ice sheet surface mass balance variability (1988–2004) from Calibrated Polar MM5 Output., *Journal of Climate*, *19*(12), 2783–2800, doi:Article.

Box, J. E. (2006), Greenland ice sheet surface mass-balance variability: 19912003, *Annals of Glaciology*, *42*(1), 90–94, doi:10.3189/172756405781812772.

Box, J. E., L. Yang, D. H. Bromwich, and L.-S. Bai (2009), Greenland ice sheet surface air temperature variability: 1840–2007*, *Journal of Climate*, *22*(14), 4029–4049, doi:10.1175/2009JCLI2816.1.

Box, J.E., N. Cressie, D.H. Bromwich, J. Jung, M. van den Broeke, J.H. van Angelen, R.R. Forster, C. Miège, E. Mosley-Thompson, B. Vinther, J.R. McConnell (2012), Greenland ice sheet mass balance reconstruction. Part I: net snow accumulation (1600-2009), *Journal of Climate*. Accepted.

Brown, J., J. Harper, W. T. Pfeffer, N. Humphrey, and J. Bradford (2011), High-resolution study of layering within the percolation and soaked facies of the Greenland ice sheet, *Annals of Glaciology*, *52*(59), 35–42, doi:10.3189/172756411799096286.

Burgess, E. W., R. R. Forster, J. E. Box, E. Mosley-Thompson, D. H. Bromwich, R. C. Bales, and L. C. Smith (2010), A spatially calibrated model of annual accumulation rate on the Greenland Ice Sheet (1958–2007), *Journal of Geophysical Research*, *115*(F2), doi:10.1029/2009JF001293.

Calanca, P., H. Gilgen, S. Ekholm, and A. Ohmura (2000), Gridded temperature and accumulation distributions for Greenland for use in cryospheric models, *Annals of Glaciology*, *31*, 118.

Chen, J. L., C. R. Wilson, and B. D. Tapley (2011), Interannual variability of Greenland ice losses from satellite gravimetry, *J. Geophys. Res.*, *116*, 11 PP., doi:201110.1029/2010JB007789.

Chen, L., O. M. Johannessen, H. Wang, and A. Ohmura (2011), Accumulation over the Greenland Ice Sheet as represented in reanalysis data, *Advances in Atmospheric Sciences*, *28*(5), 1030–1038, doi:10.1007/s00376-010-0150-9.

Cogley, J. G. (2004), Greenland accumulation: An error model, *J. Geophys. Res.*, *109*, 15 PP., doi:200410.1029/2003JD004449.

Dunse, T., O. Eisen, V. Helm, W. Rack, D. Steinhage, and V. Parry (2008), Characteristics and small-scale variability of GPR signals and their relation to snow accumulation in Greenland's percolation zone, *Journal of Glaciology*, *54*(185), 333–342, doi:10.3189/002214308784886207.

Eisen, O., F. Wilhelms, U. Nixdorf, and H. Miller (2003), Revealing the nature of radar reflections in ice: DEP-based FDTD forward modeling, *Geophys. Res. Lett.*, *30*, 4 PP., doi:200310.1029/2002GL016403.

Eisen, O., F. Wilhelms, D. Steinhage, and J. Schwander (2006), Improved method to determine radio-echo sounding reflector depths from ice-core profiles of permittivity and conductivity, *Journal of Glaciology*, *52*(177), 299–310, doi:10.3189/172756506781828674.

Ettema, J., M. R. van den Broeke, E. van Meijgaard, W. J. van de Berg, J. L. Bamber, J. E. Box, and R. C. Bales (2009), Higher surface mass balance of the Greenland ice sheet revealed by high-resolution climate modeling, *Geophys. Res. Lett.*, *36*, 5 PP., doi:200910.1029/2009GL038110.

Ettema, J., M. R. van den Broeke, E. van Meijgaard, and W. J. van de Berg (2010), Climate of the Greenland ice sheet using a high-resolution climate model – Part 2: Near-surface climate and energy balance, *The Cryosphere Discussions*, *4*(2), 603–639, doi:10.5194/tcd-4-603-2010.

Fettweis, X. (2007), Reconstruction of the 1979–2006 Greenland ice sheet surface mass balance using the regional climate model MAR, *The Cryosphere*, *1*(1), 21–40, doi:10.5194/tc-1-21-2007.

Hanna, E., J. McConnell, S. Das, J. Cappelen, and A. Stephens (2006), Observed and modeled Greenland ice sheet snow accumulation, 1958–2003, and links with regional climate forcing, *Journal of Climate*, *19*(3), 344–358, doi:10.1175/JCLI3615.1.

Hanna, E., P. Huybrechts, K. Steffen, J. Cappelen, R. Huff, C. Shuman, T. Irvine-Fynn, S. Wise, and M. Griffiths (2008), Increased runoff from melt from the Greenland ice sheet: A response to global warming, *Journal of Climate*, *21*(2), 331–341, doi:10.1175/2007JCLI1964.1.

Hanna, E. et al. (2011), Greenland Ice Sheet surface mass balance 1870 to 2010 based on Twentieth Century Reanalysis, and links with global climate forcing, *J. Geophys. Res.*, *116*, 20 PP., doi:201110.1029/2011JD016387.

Hines, K. M., and D. H. Bromwich (2008), Development and testing of polar weather research and forecasting (WRF) model. Part I: Greenland ice sheet meteorology, *Monthly Weather Review*, *136*(6), 1971–1989.

Hörhold, M. W., S. Kipfstuhl, F. Wilhelms, J. Freitag, and A. Frenzel (2011), The densification of layered polar firn, *J. Geophys. Res.*, *116*, 15 PP., doi:201110.1029/2009JF001630.

Humphrey, N. F., J. T. Harper, and W. T. Pfeffer (2012), Thermal tracking of meltwater retention in Greenland's accumulation area, *J. Geophys. Res.*, *117*, 11 PP., doi:201210.1029/2011JF002083.

Hurrell, J. W. (1995), Decadal trends in the north Atlantic oscillation: Regional temperatures and precipitation, *Science*, *269*(5224), 676–679.

Hutterli, M. A., C. C. Raible, and T. F. Stocker (2005), Reconstructing climate variability from Greenland ice sheet accumulation: An ERA40 study, *Geophys. Res. Lett.*, *32*(23), L23712, doi:10.1029/2005GL024745.

King, J. C., P. S. Anderson, D. G. Vaughan, G. W. Mann, S. D. Mobbs, and S. B. Vosper (2004), Wind-borne redistribution of snow across an Antarctic ice rise, *J. Geophys. Res.*, *109*, 12 PP., doi:200410.1029/2003JD004361.

Kovacs A., Gow A.J., and Morey R.M., The in-situ dielectric constant of polar firn revisited, *Cold Regions Science and Technology*, *23*(3), 245–256, doi:10.1016/0165-232X(94)00016-Q.

Levitus, S., J. I. Antonov, T. P. Boyer, R. A. Locarnini, H. E. Garcia, and A. V. Mishonov (2009), Global ocean heat content 1955–2008 in light of recently revealed instrumentation problems, *Geophys. Res. Lett.*, *36*, 5 PP., doi:200910.1029/2008GL037155.

Leuschen, C. and C. Allen (2010). IceBridge MCoRDS L2 Ice Thickness. Boulder, Colorado USA: NASA Distributed Active Archive Center at the National Snow and Ice Data Center. Digital media. http://nsidc.org/data/irmcr2.html

Lucas-Picher, P., M. Wulff-Nielsen, J. H. Christensen, G. Aðalgeirsdóttir, R. Mottram, and S. B. Simonsen (2012), Very high resolution regional climate model simulations over Greenland: Identifying added value, *J. Geophys. Res.*, *117*, 16 PP., doi:201210.1029/2011JD016267.

McConnell, J. R., and R. C. Bales (2004), Investigation of chemical transfer processes between atmosphere and snow at South Pole, *National Oceanic and Atmospheric Administration (NOAA) Climate Monitoring and Diagnostics Laboratory, Summary Report 2002– 2003*(27), 153–154.

McConnell, J. R., R. C. Bales, D. Belle-Oudry, J. D. Kyne, G. Lamorey, E. Hanna, and E. Mosley-Thompson (2001), Annual net snow accumulation over southern Greenland from 1975 to 1998, *Journal of Geophysical Research D: Atmospheres*, *106*(24), 33827–33837.

McConnell, J. R., G. W. Lamorey, S. W. Lambert, and K. C. Taylor (2002), Continuous ice-core chemical analyses using inductively coupled plasma mass spectrometry, *Environ. Sci. Technol.*, *36*(1), 7–11, doi:10.1021/es011088z.

McConnell, J. R., R. Edwards, G. L. Kok, M. G. Flanner, C. S. Zender, E. S. Saltzman, J. R. Banta, D. R. Pasteris, M. M. Carter, and J. D. W. Kahl (2007), 20th-Century industrial black carbon emissions altered arctic climate forcing, *Science*, *317*(5843), 1381–1384, doi:10.1126/science.1144856.

Meehl, G. A. and 13 others (2007), Global climate projections. In: Climate change 2007: The physical science basis, in Contribution of Working Group I to the Fourth Assessment Report of the Intergovernmental Panel on Climate Change. In Solomon S and 7 others eds. Cambridge University Press, Cambridge, United Kingdom and New York, NY, USA

Mosley-Thompson, E., K. Steffen, L. G. Thompson, R. Edwards, D. Bathke, J. R. McConnell, R. C. Bales, and P. N. Lin (2001), Local to regional-scale variability of annual net accumulation on the Greenland ice sheet from PARCA cores, *Journal of Geophysical Research D: Atmospheres*, *106*(24), 33839.

Mosley-Thompson, E., C. R. Readinger, P. Craigmile, L. G. Thompson, and C. A. Calder (2005), Regional sensitivity of Greenland precipitation to NAO variability, *Geophysical research letters*, *32*(24), L24707.1–L24707.4.

Ohmura, A., and N. Reeh (1991), New precipitation and accumulation maps of Greenland, *Journal of Glaciology*, *37*(125), 140.

Ohmura, A., P. Calanca, M. Wild, and M. Anklin (1999), Precipitation, Accumulation and Mass Balance of the Greenland Ice Sheet, *Zeitschrift fuer Gletscherkunde und Glaziologie*, *35*, 1–20.

Parry, V., P. Nienow, D. Mair, J. Scott, B. Hubbard, K. Steffen, and D. Wingham (2007), Investigations of meltwater refreezing and density variations in the snowpack and firn within the percolation zone of the Greenland ice sheet, *Annals of Glaciology*, *46*(1), 61–68, doi:10.3189/172756407782871332.

Rae, J. G. L. et al. (2012), Greenland ice sheet surface mass balance: Evaluating simulations and making projections with regional climate models, *The Cryosphere*, *6*(6), 1275–1294, doi:10.5194/tc-6-1275-2012.

Rignot, E., and J. Mouginot (2012), Ice flow in Greenland for the International Polar Year 2008–2009, *Geophys. Res. Lett.*, *39*(11), L11501, doi:10.1029/2012GL051634.

Rignot, E., I. Velicogna, M. R. van den Broeke, A. Monaghan, and J. Lenaerts (2011), Acceleration of the contribution of the Greenland and Antarctic ice sheets to sea level rise, *Geophys. Res. Lett.*, *38*(5), L05503, doi:10.1029/2011GL046583.

Sørensen, L. S., S. B. Simonsen, K. Nielsen, P. Lucas-Picher, G. Spada, G. Adalgeirsdottir, R. Forsberg, and C. S. Hvidberg (2011), Mass balance of the

Greenland ice sheet (2003–2008) from ICESat data – the impact of interpolation, sampling and firn density, *The Cryosphere*, *5*(1), 173–186, doi:10.5194/tc-5-173-2011.

Spikes, V. B., G. S. Hamilton, S. A. Arcone, S. Kaspari, and P. A. Mayewski (2004), Variability in accumulation rates from GPR profiling on the West Antarctic plateau, *Annals of Glaciology*, *39*(1), 238–244, doi:10.3189/172756404781814393.

Spikes, V. B., J. R. McConnell, and J. R. Banta (2007), Annual layer mapping and net snowfall measurements across the southern Greenland ice sheet using shallow radar and ice cores, *AGU Fall Meeting Abstracts*, *-1*, 0087.

Steffen, K., and J. Box (2001), Surface climatology of the Greenland Ice Sheet: Greenland Climate Network 1995–1999, *J. Geophys. Res.*, *106*(D24), 33951–33,964, doi:10.1029/2001JD900161.

Van den Broeke, M., J. Bamber, J. Ettema, E. Rignot, E. Schrama, W. J. Van De Berg, E. Van Meijgaard, I. Velicogna, and B. Wouters (2009), Partitioning recent Greenland mass loss, *Science*, *326*(5955), 984–986, doi:10.1126/science.1178176.

CHAPTER 3[2]

SPATIAL EXTENT AND TEMPORAL VARIABILITY OF THE GREENLAND FIRN AQUIFER DETECTED BY GROUND AND AIRBORNE RADARS

3.1. Abstract

Widespread perennial firn aquifers are found in an elevation range of ~1200-2000 m within the lower percolation zone of the Greenland ice sheet. Aquifers are predominantly found in the high snow-accumulation regions of southeast and south Greenland. Prior to melt onset, we map the aquifer extent and quantify the water-table interannual variations using surface-based and airborne radars. The aquifers are mapped along a linear distance of 2420 km over three NASA Operation IceBridge (OIB) campaigns (2011-13) and the average depth to the water table is 22±8 m. At our Southeast Greenland field site, we found that the water table was spatially stable between 2011 and 2014, fluctuating less than 2.5 m vertically. Upstream of Helheim glacier, a spatially stable aquifer is inferred from missing bed echoes from 1993-2008. After 2008, this aquifer expands to higher elevations and after spring 2012, drainage of its lower-

[2] This chapter has been submitted under the same title to the Journal of Geophysical Research: Earth Surface in January 2015 with authors C. Miège, R. Forster, L. Brucker, L. Koenig, D. Solomon, J. Paden, J. Box, E. Burgess, J. Miller, L. McNerney, N. Brautigam, R. Fausto, and S. Gogineni.

elevation portion is suspected. Combining radar data with surface-elevation profiles, we find that in general, firn aquifers are initiated by strong surface slope gradients. The water flows laterally in an unconfined aquifer, topographically driven by ice-sheet surface undulations until water encounters crevasses. Our hydraulic simulations suggest local flow cells are formed within the aquifer and some water is discharged at the steep-to-flat transitions. The firn is saturated with water at the firn-ice transition, which delivers heat downward. Water drainage into crevasses is suspected from repeated radar profiles, but the volume and volumetric flow rate of water are unknown.

Key Points:

- A ~28,500 km^2 firn aquifer is mapped using radar for 2011-2013
- Upstream of Helheim Glacier, an aquifer is evident since 1993
- A partial drainage of this Helheim firn aquifer is suspected after 2012

3.2. Introduction

For the last two decades, the Greenland ice sheet has lost mass at an increasing rate [e.g., *Rignot et al.*, 2011]. For the same period, a reconciled mass loss is estimated at 142±49 Gt y^{-1} [*Shepherd et al.*, 2012]. With air temperature increasing over the ice sheet the mass loss is dominated by surface melt [*Hanna et al.*, 2013]. In the 2009-2012 period, ~70% of the ice-sheet mass loss has come from surface melt and the remaining from ice discharge [*Enderlin et al.*, 2014]. Melt extent records show Greenland surface melt has increased over the last decade with recent strong advection of warm air from the south during summer [e.g., *Box et al.*, 2011; *Tedesco et al.*, 2011]. In recent years, the Greenland ice sheet's largest melt extent occurred in July 2012 when 98.6% of its area

experienced at least a brief surface melt [*Tedesco et al.*, 2013]. The summer meltwater volume, retention proportion, and transport pathways are variable in space and time. These hydrological characteristics directly impact ice-sheet mass balance, ice-flow dynamics, sea-level-rise contribution, and remain poorly understood [e.g., *Rennermalm et al.*, 2013]. In Southeast and South Greenland, widespread firn aquifers have been observed in high accumulation regions (~1.2 m w.eq. y^{-1}) of the percolation zone [*Forster et al.*, 2014]. The firn aquifer persists at depth throughout the entire year and stores water and heat at depth within the firn.

3.2.1. Greenland percolation zone

The percolation zone corresponds to the part of the accumulation zone where surface water is generated and percolates into the subsurface (snow or firn) before refreezing and forming ice lenses [*Benson* 1962; *Cogley et al.*, 2011]. Coincident with the recent warming, surface melt is not only occurring in the lower-elevation margins of the ice sheet, but it is also migrating toward the interior, higher elevations of the ice sheet. Consequently, the dry-snow zone is predicted to retreat and the percolation zone is predicted to expand in future decades [*McGrath et al.*, 2013]. Within the percolation zone, two sub-areas are defined depending on the amount of melt produced. At relatively high elevations (~2000 m) in the upper percolation zone, air temperatures exceed 0°C for only a few days per year and the subsequent meltwater percolates to a depth less than 1.5 m and refreezes in the snow [*Parry et al.*, 2007; *Brown et al.*, 2011]. In the lower part of the percolation zone (~1500 m), the amount of meltwater increased due to several weeks

of summer surface melt, allowing meltwater to percolate to greater depths [*Humphrey et al.*, 2012].

The percolation of water into the snow and firn is a nonuniform process in space and time [e.g., *Colbeck* 1975]. Temperatures above 0°C lead to surface melt, and resulting meltwater drains downward through porous snow enhancing destructive snow metamorphism [e.g., *Raymond and Tusima*, 1979]. Two competing forces exist: gravity pulls water down while surface tensions (capillary forces) hold a small amount of water within the snow and firn microstructure. Cold-room experiments suggest that capillary forces hold up to ~10% of water in wet snow, and that the holding capacity decreases at depth with an increase of snow/firn density [*Coléou and Lessaffre*, 1998]. The same experiments found a water-saturated layer at the bottom of each snow sample holding a greater amount of water for corresponding bulk densities of 900-950 kg m^{-3}. In firn conditions, *Schneider and Jansson* [2004] reported higher irreducible water content for lower porosity. For the Greenland percolation zone, the firn stratigraphy is heterogeneous and characterized by ice lenses (horizontal) and ice columns/pipes (vertical). The ice inclusions offer preferential pathways for meltwater to travel, changing firn physical properties in their immediate vicinity [*Pfeffer and Humphrey*, 1996; *Humphrey et al.*, 2012]. Following a network of ice lenses and columns, meltwater percolates toward deeper horizons (>10 m) and bypasses preexisting ice lenses. At greater depths (>10 m), a water-saturated layer persists in the firn and may remain liquid year-round in the inter-granular space [*Humphrey et al.*, 2012], similar to a groundwater aquifer [*Forster et al.*, 2014].

3.2.2. Firn aquifers

The presence of water in firn aquifers is well documented for mountain glaciers [e.g., *Fountain and Walder*, 1998; *Jansson et al.*, 2003]. Examples for temperate glaciers include: Vernagtferner, Oetztal Alps [*Oerter and Moser*, 1982] and South Cascade Glacier, WA, U.S.A. [*Fountain*, 1989]. Polythermal glaciers like Storglaciären in Northern Sweden also store water in a firn aquifer [*Schneider*, 1999; *Schneider and Jansson*, 2004]. A firn aquifer in a glacier forms when enough meltwater (or rain) percolates from the surface to the firn/ice transition where a quasi-impermeable barrier is found. From there, the water table rises as more surface water is supplied from the surface melt in the summer. Water flows laterally under hydraulic gradients, following the glacier slope and eventually draining into nearby crevasses. The water table decays after surface melting ceases, reaching a minimum in late winter. *Fountain* [1996] reports a complete draining of the aquifer by late November. The firn water storage duration is between a few days to less than a year [*Jansson et al.*, 2003]. The thickness of the firn aquifer is related to the hydraulic gradient (water table slope) and the efficiency of the englacial network allowing water to exit the glacier system [*Jansson et al.*, 2003]. Despite their existence in different types of glaciers, firn aquifers present relatively similar hydraulic characteristics, reflecting a similar snow grain metamorphism rate in response to water input [*Fountain and Walder*, 1998]. Firn hydraulic conductivity occurs at values spanning 1 to 5 x 10^{-5} m s^{-1} with an average porosity of 0.15 [*Fountain and Walder*, 1998]. In the aquifer, water is found to occupy 40% of the pore space while air still accounts for 60% of the total void volume [*Fountain et al.*, 1989]. Depth to the water table from the snow surface depends on elevation and location in the glacier. Upstream,

water tables can be found as deep as 40 m [*Fountain and Walder*, 1998]. Percolation vertical velocities are found in a range of 0.12 to 0.35 m h^{-1} in the firn, equivalent to ~40 h to bring water from the surface to a water table at 10 m depth [*Schneider*, 1999]. The horizontal hydraulic gradients have been averaged to 5.7° for Storglaciären [*Schneider*, 1999].

The Greenland firn aquifer is more extensive spatially than its glacier analogues, usually between 10 and 20 km on a given along-flow direction with an averaged slope less than 1° [*Forster et al.*, 2014]. Assuming a similar hydraulic conductivity value as glaciers and weak hydraulic gradients, it could take months for water at the high-elevation end of the water-saturated firn layer to exit the glacial system [*Humphrey et al.*, 2012]. Over the course of a year, the water present in the Greenland firn aquifer does not fully drain. The water persists over the winter, and thus is perennial, in contrast to mountain glaciers. At the end of the winter, the Greenland firn aquifer stores a non-negligible mass (140±20 Gt) of water [*Koenig et al.*, 2014]. This observation contrasts with temperate glacier aquifers where the presence of water in the firn aquifer is seasonal, restricted to the summer months, corresponding to a shorter-term storage system (<1 year) and a limited buffering effect as the water exits the firn [*Fountain* 1996; *Jansson et al.,* 2003]. As simulated by *Kuipers Munneke et al.* [2014], a perennial firn aquifer only exists in regions with moderate to strong summer surface melt and high snow accumulation, which provide both fall insulation and wider pore space at depth.

3.2.3. Radar imaging of ice-sheet water tables

For typical groundwater aquifer investigations in coarse-textured soils, ground-penetrating radar (GPR) is often used as a geophysical nondestructive technique to supplement conventional depth-to-water table measurements [e.g., *Doolittle et al.*, 2006]. In our study, the water table is imaged using a combination of ground and airborne radars. The presence of water in the firn slows electromagnetic wave propagation as it increases the medium's dielectric constant [*Smith and Evans*, 1972]. In the case of wet snow, the real part of the dielectric constant (permittivity, ε') increases with the liquid water content [*Bradford et al.*, 2009]. The strong dielectric contrast between liquid water (ε_w'=80) and the dry firn (ε_f'=2.4) results in an attenuation of the transmitted radar signal. *Smith and Evans* [1972] calculated a dielectric constant of ε_f'=15.2 for soaked-firn conditions. The electromagnetic wave attenuation (reflection and/or absorption) is related to the water volume and water conductivity in the firn and depends on the frequency of the radar system used [*Smith and Evans*, 1972]. For all frequencies used in this study, a high-amplitude reflector is due to the significant reflection of the electromagnetic wave when encountering liquid water in the subsurface. The advantage of this technique is the continuous mapping of the water table elevation, giving a continuous measurement of the hydraulic head.

3.2.4. Objectives

This study focuses on the Greenland firn aquifer extent and temporal evolution using a combination of airborne radar and ground data (GPR and firn cores). We provide an updated map of the Greenland firn aquifer extent using three years of airborne radar

data. We study the temporal evolution of the water table over repeated airborne and ground tracks between 2011 and 2014. We present the connections between the firn aquifer and the crevasse network. We infer evidence of the firn aquifer existing in the early 1990s from archived depth-sounding radar data, and we simulate lateral flow within the firn aquifer. Only the interannual changes are investigated here, with an aquifer at its lowest filling capacity throughout the year. Since airborne data collection occurs each year before the melt onset in March/April, examining seasonal aquifer variability is beyond the scope of this study.

3.3. Field site

The surface-based measurements were made on the southeastern Greenland ice sheet (66.18°N, 39.04°W, ~1560 m a.s.l.), 50 km west from Sermilik Fjord (Figure 3.1). This site was chosen for firn-core extraction to verify the high simulated accumulation rates (1.44±0.30 m w.eq. y^{-1}) and large interannual variations in the region [*Burgess et al.*, 2010], which were confirmed with 50-m dry firn cores [*Miège et al.*, 2013]. At this location, the annual number of melt days was 35±20 days over the 1979-2012 period, with a significant increase surface-melt duration in the last decade (Figure 3.1, top-right inset). For the 2010-2013 period, summer 2011 was within the 1979-2012 average melt duration, whereas 2010 and 2012 witness extensive melt (Figure 3.1, top-right inset). In 2013, melt started early June, but it only persisted for 10 days more than the 1981-2010 average [Mote, nsidc.org/greenland-today/]. As a result of surface melt and dynamic thinning, altimetry observations showed a surface lowering at a rate of ~1 m y^{-1} for 2003-2009 [*Sørensen et al.*, 2011; *Csatho et al.*, 2014].

Our field work was conducted in April to early May each year, prior to melt onset, when the firn aquifer is assumed to be at the seasonal minimum capacity. Fifteen kilometers west of our location, the ice thickness is about 1000 m, according to the observation from the OIB 2012 multi-channel coherent radar depth sounder (MCoRDS) [*Gogineni*, 2012]. A surface velocity of 7.5 cm d^{-1} was measured over 10 days in April 2014, giving a linearly extrapolated velocity of ~30 m y^{-1}, with an azimuth of 55°. In 2011, during the third Arctic Circle Traverse (ACT), a 2.6-km line, between the firn cores ACT-11A and ACT11-A2, was surveyed by GPR (Figure 3.1). In April 2013 and 2014, this same line was resurveyed using a similar GPR system to investigate the temporal variability of the firn aquifer.

3.4. Data

3.4.1. Airborne data

Most of the airborne radar data presented in this study were collected each year during April-May between 2011 and 2013 as part of OIB. Four different radar systems designed by the Center for Remote Sensing (CReSIS) with different frequency ranges were operated simultaneously on the NASA aircraft [*Rodriguez-Morales et al.*, 2013]. We use ultra-high-frequency radar referred to as the Accumulation Radar (AR). It operates at a center frequency of 750MHz with a bandwidth of about 300 MHz. The ultra-wideband width enables imaging of internal features including the water table with a 65 cm vertical resolution [*Rodriguez-Morales et al.*, 2013]. In the along-track dimension, the data product spacing is 35.8 m for a platform velocity of 140 m s^{-1}. For smooth, quasi-specular targets (i.e., internal layers), the across-track resolution is equal to

the first Fresnel zone, which is 20 m at 750 MHz and 500 m height [*Leuschen*, 2011]. The snow surface was identified and picked in the radar data using an amplitude threshold at the base of the surface return. This threshold had to be adjusted for each OIB campaign; no other changes were made in data processing. Radar hardware changes between 2011 and 2014 involved attenuator setting changes, but do not impact our analysis.

In addition to the AR, we use the radar depth sounder (MCoRDS), which operates at 195 MHz during the OIB campaigns. We also use older RDS data (150 MHz) prior to OIB, to retrieve evidence of the firn aquifer in the 1990s by identifying areas where bed echoes (and internal layers) are missing or weakened due to water in the firn column. Archived depth sounder data are made publicly available since 1993 by CReSIS (data.cresis.ku.edu).

We also used the NASA Airborne Topographic Mapper (ATM) LIDAR [*Krabill*, 2011] operating simultaneously with the AR and the RDS to retrieve the along-track surface elevation profile. The spatial resolution is about 50 m and the accuracy of the measured elevation is 8.5 cm [*Krabill et al.*, 2002]. At nadir, the elevation profile is resampled to be synchronized with individual traces from the radar data. Using the surface elevation, we calculate the depth of the water table.

3.4.2. Ground-based data

Surface-based radar measurements were made using a 400-MHz GPR from Geophysical Survey Systems, Inc. (GSSI). The layer interface separation resolution is 35 cm for the dry Antarctic firn [*Spikes et al.*, 2004]. We sampled at a rate of 6 traces s^{-1},

and collected 2048 samples per trace for 500 ns, yielding a ~0.24 ns sample interval. Two different types of surveys were performed: one using a snowmobile in 2011 moving at about ~3 m s^{-1} and one using skis in 2013 and 2014 moving slower between 1 and 2 m s^{-1}. The averaged trace spacing was about 0.5 m via snowmobile and 0.3 m via skis. To reduce noise in both surveys, each trace corresponds to a real-time stacking average of 6 traces taken over the same target almost instantaneously. In addition, time-dependent gain was used to compensate for signal attenuation within the firn. In post-processing, an additional stacking (8 times) increased signal-to-noise ratio, bringing the trace interval between 4.0 m (snowmobile) and 2.4 m (skis). The first 13 samples (~3.2 ns) of each trace are removed to account for the signal travelling through the hardware and cable. No additional filtering was applied to the GPR data as the water layer represents a bright target that contrasts well with the dry firn located above.

Simultaneous to the GPR data collection, we used a Trimble R7 rover GPS in a kinematic mode for horizontal and vertical geolocation. Positions were recorded with a 5 s interval, corresponding to a sampling interval of ~15 m by snowmobile and ~7.5 m while traveling by skis. The online Canadian Spatial Reference Service (CSRS) is chosen to process the GPS data with a precise point positioning (PPP) approach. It uses precise global navigation satellite system (GNSS) orbit ephemerides (near real time) and clock information together with precise undifferenced carrier-phase observations to improve the accuracy of the collected GPS data points [*Mireault et al.*, 2008]. Uncertainties are related within one standard deviation of each transect and averaged here for the three field seasons: latitude and longitude: 3.5 cm and elevation: 7.0 cm. The GPS is

synchronized to the GPR by assigning to each radar trace a linearly interpolated position and elevation.

A total of five firn density profiles were obtained from our firn cores in the study region between 2010 and 2013 (Figure 3.1). Each core section was weighed to retrieve a depth-density profile. In 2010 and 2011, the vertical resolution was ~1 m [*Miège et al.*, 2013], while it was about ~20 cm in 2013 [*Koenig et al.*, 2014]. In the wet-snow zone, ice lenses and pipes are found in the firn cores. Seasonal snow depth (snow/firn transition) is estimated from the extracted cores when small (<0.8 mm) dry-snow grains transition to larger (>1.5 mm) grains with rounded angles, showing evidence of previous melting. Seasonal snow depth was about 280 cm on 6 April 2013 and 300 cm on 10 April 2014.

Finally, we use temperature, ablation, and snowfall measurements collected from the two automatic weather stations (AWS) in Southeast Greenland, part of the PROMICE network [*Ahlstrøm et al.*, 2008, www.promice.org]. TAS_L station (65.64°N, 38.90°W, ~270 m a.s.l.) and TAS_U station (65.70°N, 38.87°W, ~570 m a.s.l.) are located in the ablation area of the ice sheet, ~50 km south from our field site.

3.5. Methods

3.5.1. Radar travel time to depth conversion

The depth of the aquifer surface is estimated from the two-way-travel time (TWT) of the radar electromagnetic wave between the snow surface and the water-table surface. For nonmagnetic and low-loss dielectric mediums like snow and firn, the velocity (v) of an electromagnetic wave can be approximated as the ratio of the velocity in a vacuum (c ~0.3 m ns^{-1}) to the square root of the permittivity (ε') of the medium (Equation (1)).

$$v = c/\sqrt{\varepsilon'} \qquad (1)$$

A first-order depth estimate is obtained using a constant dielectric value throughout the firn of ε'=2.4 and the associated electromagnetic velocity is 0.194 m ns^{-1}. This velocity is comparable to velocity values (0.196 m ns^{-1}) used in the western ice sheet lower percolation zone [*Brown et al.,* 2011]. To refine this depth estimate, we use an empirical relationship, Equation (2), to calculate ε' knowing the density (ρ) [*Kovacs et al.*, 1995].

$$\varepsilon' = (1 + 0.845\rho(z))^2 \qquad (2)$$

The steady-state composite density profile (Figure 3.2) used in this study is based on five dry cores extracted, either above the water-table surface (ACT11-A and A2, FA13-B, FA-14) or less than 20 km upstream of the firn aquifer (ACT10-A and ACT11-B) [*Forster et al.*, 2014; *Koenig et al.*, 2014]. By using a composite-averaged density profile, we attempt to minimize the impact of small-scale spatial density heterogeneities in the firn of the lower percolation zone. Indeed, at the different firn-core locations, we observed ice lenses up to 40 cm thick, and ice pipes in the firn below the seasonal snow. To smooth their impact on the density profile, we use a bi-exponential relationship to fit the data within one standard deviation (Figure 3.2).

At greater depth (28 m), a significant difference (~1 m) exists between the density-adjusted velocity conversion compared to the constant velocity conversion (see Figure 3.3, green dashed line). This difference increases up to 3 m for 500 ns (~50 m). In this study, to better account for the densification at depth, we use the density adjusted conversion method to retrieve the depth to the water table. The presence of interstitial water within the snow microstructure has an impact on the TWT to depth conversion as it

will slow down the transmitted electromagnetic waves [*Bradford et al.*, 2009]. Here, we are focusing on the surface of the water table only; and we make the assumption that the firn above the water table is cold and dry.

3.5.2. Firn aquifer extent

We delineate the firn aquifer lateral extent of the radar-derived map using polygons. We combine the 3 years of OIB data allowing us to increase the aquifer coverage and two types of polygons are chosen. In regions with extensive OIB coverage, we combine along-surface slope flights and across-surface slope flights to pick the high- and low-elevation edges, and its latitudinal extent. Extrapolation of the aquifer area is done between two parallel flightlines if the aquifer is detected in both flightlines. In regions with less radar coverage and isolated flightlines, polygons are represented with a rectangular/square box with a 5-10 km width. Isolated aquifers detected by AR for only 1 year and for a linear distance less than 5 km were not included in a polygon. On the other hand, similar length gaps can be found within the wider polygons (Figure 3.6). A total of 35 polygons were created with areas ranging from 25 km^2 to 13,500 km^2 as shown in Figure 3.6.

3.5.3. Water table uncertainties

During the 2011 fieldwork, two firn cores ACT11-A (1 May 2011) and ACT11-A2 (30 April 2011) were extracted (Figure 3.1). For these two cores their last meter-long core segment was retrieved in water saturated firn conditions at 25.3±1 m and at 10.4±1 m depth, respectively. On May 2, 2011 the GPR imaged a bright reflector at similar

depths of 25.0±0.7 m and 9.7±0.3 m. In addition, thirteen days prior to the field campaign, OIB flew over the field site with the AR, allowing a direct comparison between the GPR and the AR (Figure 3.4) [*Forster et al.*, 2014]. Over an 18-km transect, the average difference between the two water table depths is 26 cm with a standard deviation of 34 cm. The significant correlation (r = 0.99) between the water-table depth observations from the two radars allows firn aquifer mapping in locations where only AR data exists [*Forster et al.*, 2014].

There are two major challenges associated with the detection of the firn aquifer using the AR data: (1) Presence or absence of the firn aquifer; and (2), if present, depth of the water table. The uncertainty quantification is difficult since the layer picking is not automated and thus a subjective bias is introduced by the operator. A total distance of ~140,000 km is flown during each OIB campaign (2011-2013). For each flightline, we observe individual radar frames manually and look for similar firn aquifer reflection patterns to the known 2011 profile, at a depth range of 5-50 m. We define a water table when a continuous strong reflector can be followed for more than 0.5 km horizontally. To quantify the bias introduced from the layer tracing, the entire 2011 OIB data were traced twice, by two different operators using two different tracing methods (manual vs. semi-automatic). The semi-automatic method used the layer-picker algorithm developed by *Ivanoff and Koenig* at NASA Goddard. The picker is similar to an edge-detection method, based on differences between lower and upper frequencies to accentuate the peaks. The automatic picker performed well in regions with a clear water-table signal, but manual tracing was required for weaker return signals. While comparing these two methods, ~75% agreement in space is found relative to the presence of the firn aquifer.

The main differences between the layer traces from the two methods are due to defining the edges of the water table where the strength of the reflector tends to diminish gradually.

The data quality and subsequent water table selection are dependent on airplane survey conditions, such as turbulence and turning geometry. For example, a roll above 10° prevents detection of internal layers and hence identification of the firn aquifer. Imaging the deeper parts the firn aquifer is challenging due to the penetration depth of the AR. In general, an aquifer deeper than 40 m in the percolation zone is not always well imaged in the AR profile. This is mainly because weak returns from internal layers are masked by surface clutter (off-vertical surface) at the edges of the percolation zone. Layer depth uncertainty comes from two sources: TWT to depth conversion (Section 4.1) and layer picking. The TWT to depth conversion uncertainty is associated with the density profile used. For example, within $\pm 1\sigma$ of density, the uncertainty of is ±40 cm for an averaged depth to the water table at 20 m, the uncertainty is up to 1 m for the first 50 m (see Figure 3.3, gray dashed lines). For the AR, the layer picking was repeated twice for 2011 and the unsmoothed average depth difference was 60 cm for the ~1000 km of radar data (~50,000 radar traces). Internal continuous horizons collected by GPR were brighter and more distinct, improving layer picking uncertainty. The repeated picking test over a 5 km segment shows difference of 7 cm (or 3 samples) in average. Finally, we calculate averaged error propagations (sum of square root errors) based on the two uncorrelated uncertainties of 72 cm for the AR and 41 cm for the GPR.

3.5.4. Bed echoes missing from beneath firn aquifer regions

The presence of a saturated liquid water layer within the ice sheet firn inhibits radar's ability to image the bedrock at the base of the ice sheet, even at lower frequencies [*Rodriguez-Morales et al.*, 2013]. The AR and MCoRDS systems have been operating simultaneously since 2010, onboard the NASA P-3 aircraft, enabling a direct comparison of the two systems in aquifer regions. This comparison is illustrated in Figure 3.5 for a transect collected in spring 2012, on the southern arm of the Helheim glacier (between red arrows on Figure 3.1). A good agreement is found between weakened/intermittent/missing bed echoes and the presence of a water-saturated layer (Figure 3.5). This observation motivates us to retrieve archived airborne data collected by CReSIS since 1993 when only the RDS system was operating. Here, we focus our analysis on the Helheim Glacier where firn aquifer has been detected during the 2011-2013 period. With this method only the presence or absence of the water layer is inferred, without estimating the depth to the water table. However, other causes for missing bed echoes cannot be fully excluded: 1) Lower radar sensitivity is found in older datasets since radar systems and processing techniques have improved over time. 2) Prior to 2006, the radiometric quality of the data is unknown and could vary between range lines due to radar-system changes and signal-processing changes. 3) We cannot exclude possible changes in basal conditions. We minimize the impact of these other causes by finding that surface and surface multiple do not change in strength significantly at the aquifer transition. In addition, the relative differences of ice-bottom scattering are negligible without the aquifer between two points as the relative ice-bottom scattering between the

same points is large when the aquifer is present at one point. Finally, the internal layers seem to disappear at the same time, suggesting that it cannot be related to changes in basal conditions alone (Figure 3.5).

3.5.5. 2-D hydrological flow model

The radar mapping of the water table gives us the opportunity to investigate water lateral flow in the firn aquifer. The radar data combined with laser altimetry provide a continuous 2-D measurement of the water surface relative to the surface topography along an ice-flow line. Spatial undulations of the water table, which are stable year-to-year, could imply that local flow cells are created in the aquifer with a similar scale to spatial undulations in the surface topography (typically less than 10 km). The flow-cell lateral limits are marked with water recharge and discharge locations related to the surface topography. We test this hypothesis using a terrestrial 2-D finite-element groundwater model, SEEP2D, which is part of the Groundwater Modeling System (GMS) package [*Jones*, 1999]. This model has been developed and used for terrestrial aquifer simulations in both confined and unconfined circumstances. A 1st type boundary condition was used, by assigning a head value to each node along the upper boundary. The head value corresponds to the water surface elevation inferred from the radar (every 16 m in average). Hydraulic conductivity values of $1x10^{-5}$ m s^{-1} are used homogeneously throughout the aquifer [*Fountain and Walder*, 1998], and we assume a constant aquifer thickness of 25 m [*Koenig et al.*, 2014]. To summarize, three main assumptions are made for this simulation: steady state, constant firn aquifer thickness, and constant hydraulic conductivity.

3.6. Results

3.6.1. Firn aquifer map

Three OIB seasons (2011, 2012, and 2013) are used to map the presence of a firn aquifer over the Greenland ice sheet. In 2011, a total of about ~800 km of radar profiles with the presence of water within the firn is revealed mainly in Southeast Greenland for a total area of 13,600 km^2 (Figure 3.6b). After the 2012 airborne campaign, the firn aquifer delineation is improved for the southern tip (Figure 3.6a) and revealed in East Greenland (Figure 3.6c). The Sukkertoppen ice cap, ~100 km southwest of Kangerlussuaq, has higher accumulation rates and thus also maintains liquid water at depth (~185 km^2) over the 2010-11 and 2011-12 winters (not surveyed in 2013). Rare occurrences of firn aquifer exist in Northwest Greenland (~85 km^2), while no aquifers were identified in Northeast Greenland (Figure 3.6). The Geikie plateau (east Greenland) presents a few isolated locations with perennial firn water storage.

With a mean elevation at 1660±275 m, most of the firn aquifer is restricted spatially below the 2000 m contour line, except for the southern tip of the ice sheet with locations around ~2000 m (Figure 3.6). A total linear distance of 2420 km of firn aquifer has been imaged between the three spring airborne surveys, representing a total area of 28,500 km^2 (Table 3.1). The surface elevation distribution of the firn aquifer is skewed toward higher elevations; this distribution varies between years (Figure 3.7). Skewed distributions could also originate from OIB campaign's specific objectives and regional focus. The depth to the water table presents a normal distribution, with a mean of 22±7 m, consistent from year to year (Figure 3.7). The total delineated water-table area based

on AR is ~60% less than the RACMO2 model estimate (70,000 km^2) for the persisting liquid water content in the firn layer for April 2011 [*Forster et al.*, 2014]. On the one hand, the area derived by the radar observation is biased by the flightline location as future flightlines could reveal a greater spatial extent of the firn aquifer. On the other hand, RACMO2 tends to simulate liquid water held at depth in crevassed locations where the AR does not record the presence of an aquifer. In addition, RACMO2 coarser spatial resolution (11-km pixels) and absence of lateral flow simulations tend to overestimate the aquifer extent. The radar-derived area estimate implies that the volume of 140±20 Gt of water stored in the aquifer estimated by *Koenig et al.* [2014], based on the 70,000-km^2 model estimate, could be half the reported value.

3.6.2. Aquifer hydraulic properties

Using the radar data, we can deduce information on the aquifer hydraulic properties, like its confined/unconfined behavior. In the radar data, the internal layers, due to density contrasts, are only imaged above the water table. At the dry/wet transition, the dominant reflection followed by attenuation in the saturated firn prevents tracing internal layers below the water table. Therefore, the bottom of the aquifer, which is defined as the transition of water-saturated firn to glacial ice (due to compaction) [*Koenig et al.*, 2014], cannot be detected at the GPR and AR frequencies (400 MHz and 750 MHz, respectively) (Figure 3.4). From Figure 3.4a (topographically corrected in Figure 3.9, left), we note that the internal reflection horizons, caused by density contrasts and interpreted as isochrones when calculating accumulation rates, intersect the water table and are not ending while encountering water. Few brighter internal layers are preserved

within the aquifer. This observation is consistent with the firn cores extracted in the aquifer in 2013 that presents a preserved stratigraphy with ice layers of different thicknesses. However, the depths of the preserved layers below the water-table surface are over-estimated since the electromagnetic signal slows down when encountering water and the TWT-depth conversion is set up for dry conditions. The water table intersecting with pre-existing internal layering implies 1) a lateral flow of water influenced by the surface slope and 2) an unconfined behavior of the aquifer at least in some parts, where the water is not constrained by laterally extensive refrozen ice layers. The spatial pattern of the water table tends to confirm the unconfined behavior observed in glacier aquifers [*Fountain and Walder*, 1998].

The unconfined aquifer assumption allows continuous head estimates to be made directly from the depth to the water table along the radar profile. The horizontal hydraulic gradient is equivalent to the water table slope. Figure 3.8 illustrates the variability of the water table imaged by AR over a 25 km along-flow transect and corrected for topography. Small-scale surface undulations have a dominant effect on the depth to water surface. For example, over ~5 km distance, <50 m of elevation changes lead to water surface changes of 20 m (Figure 3.8). At a larger scale (~25 km), we find a deeper aquifer in the higher-elevation portion compared to the lower-elevation portion of the profile (20 to 25 km). This is consistent with observations on mountain glacier aquifers over shorter distances [*Fountain* 1989]. Along this profile, the average surface slope is 0.64° and the averaged hydraulic gradient is 0.61°, about 10 times lower on average than mountain glacier aquifers [*Schneider* 1909]. The depth to the water table local minima agrees with

null surface slope. This relationship is typical and can be seen along other flightlines discussed later (Figure 3.10).

3.6.3. Temporal evolution

Radar measurements repeated at the same locations allow us to monitor firn aquifer spatial variations over time. RDS data obtained between 1993 and 2013 are only used to infer the presence or absence of the aquifer over time. AR and GPR are only available for the 2011-2014 period, and due to finer range (vertical resolution) these observations are also used to monitor variability in the water table depth. Only the interannual variability is investigated here since measurements are made once a year. Since the airplane/snowmobile/ski tracks were not exactly superposed between years (up to 220 m of spatial differences), we linearly interpolate the radar data to the same profile to avoid image distortions.

A GPR profile (~2.5 km), originally collected in May 2011, has been re-surveyed with the same GPR in April 2013 and April 2014 between firn core locations ACT11-A and -A2 (Figure 3.9). There was no field season in 2012, but the transect was flown by OIB and allowed us to fill the temporal gap with AR data. Along this transect the snow surface lowered 0.4, 1.4, and 1.0 m for 2011-2012, 2012-2013, and 2013-2014, respectively (Figure 3.9). The water table does not follow the same lowering trend. After a 0.7 m averaged vertical lowering between 2011 and 2012, the water table was found 1.2 m closer to the surface in 2013. Later, in 2014, the water-table is found on average 2.5 m deeper than in 2013 (Figure 3.9). In addition, we compare the vertical stratigraphy from firn cores extracted above the water table to observe changes in ice lenses to firn ratio over time (Table 3.2). This examination was made by only distinguishing snow/firn and

ice. From the snow surface to the water table, ice lenses represent less than 10% in average of the stratigraphy and no increase of this ratio has been observed over the short 2-year period, but including the stronger 2012 melt year (Table 3.2).

We also analyze the firn aquifer spatial variations directly upstream of the south arm of Helheim Glacier, since the glacier has been repeatedly airborne surveyed since 1993 (Figure 3.10). Over a 22-km along-flow profile, we find that bed echoes are missing in the radar observations for a ~5-km segment (from 14 to 19 km) in 1993-2003, indicating the presumed presence of the firn aquifer. For 2006-2008, the aquifer is restricted to a narrower width of ~3 km, and its expansion to higher elevations is observed in 2012 (Figure 3.10). In 2013, the bed is revealed in most of the previously undetected segments (from 11 to 19 km), inferring that a significant volume of liquid water has likely drained out of the firn or refroze in place. The bed/no bed transitions are consistent over time, and correspond to significant slope gradients observed at 3 km (2013) and 14 km (1993, 2003) on Figure 3.10. The locally higher slopes allow enough water to move laterally through the steeper parts and start pooling in flatter parts. This behavior is observed in topographically driven water flow in unconfined system [*Toth*, 1963]. Upstream of Helheim, the snow surface remained relatively constant between 1993 and 2003 based on the ATM data onboard the airplane [*Krabill*, 2011]. An important lowering between 7 m (upper end of the profile) and 18 m (lower end) of the profile is observed between 2003 and 2013 [*Krabill*, 2011]. This surface thinning is associated with the short-lived acceleration of Helheim Glacier [*Howat et al.*, 2008; *Enderlin et al.*, 2014].

The AR provides additional details on the water table between 2011 and 2014 (Figure 3.11). The water table is relatively stable between 2011 and 2012; a 3-km extension upstream is observed in 2012. At the low-elevation end, the water table undulates, following the surface topography, and ends up increasing its depth before encountering crevasses where the bright return disappears (~16 km on Figure 3.11). In 2013, consistent with MCoRDS observations (Figure 3.10), the water table is substantially diminished or missing between 12 and 16 km. On the upstream end of the profile (1 to 5 km), the water table rose ~5 m in 2013 compared to 2012.

3.6.4. Lateral boundaries

The lateral limits (spatial extent) of the aquifer are studied using the GPR (upper-elevation limit) and the AR (lower-elevation limit). AR allows data collection in crevassed terrain, whereas the GPR provides greater penetration depth and images finer details at the upper end of the firn aquifer. The upper-elevation transition (~1700 m for the ACT traverse) between dry and wet firn is progressive and diffuse. In Figure 3.4b, two brighter reflectors are found at depths, between 28 and 38 m, but present some short discontinuities. The low-elevation end of the aquifer is only imaged here using AR data, coupled with high-resolution visible satellite imagery. The upper crevasses are imaged by AR, represented by vertical brighter stripes locally disrupting the internal layers (Figures 3.12 and 3.13). Combining the AR profile with 0.5-m resolution images, we observe that the lower-elevation edge of water table corresponds with the initial encounter of crevasses, implying drainage of water in subjacent crevasses. The crevasse depths are unknown, and our current measurements do not allow us to investigate the fate of the

water as it exits the aquifer. In Figure 3.13, for the Helheim case, the upper crevasses (km 4-5) are located on a steeper section and a brighter reflector is observed when the slope decreases (km 5-6). This observation indicates presence of liquid water downslope of the first crevasses, deducing that the crevasse depth did not reach the aquifer surface (< 20 m). The relationship between firn aquifer and crevasses is further addressed in the discussion section.

3.6.5. 2-D simulated flow

SEEP2D simulates flow of water within the firn aquifer while using variables, assumptions, and boundary conditions described in the method section. Figure 3.14 shows simulated local flow cells that develop similar to topographically driven water flow [*Toth*, 1963]. The flow cell size is dependent on surface undulations (slope) and the spacing between flowlines decreases with increasing water velocity. To interpret the ground-water simulation, we assume that Darcy's law is valid and there is no flow into or out of the plane of the cross section (i.e., 2D flow). Following Darcy's law, the volumetric flow rate Q (m^3 s^{-1}) of an incompressible fluid is calculated under stationary conditions within a porous medium of area A (m^2) and length ΔL (m) under a head difference ΔH (m).

$$Q = K\,A\,\frac{\Delta H}{\Delta L} \qquad (3)$$

We obtain an averaged total flow rate (Q) of 3,305 m^3 y^{-1} per meter of profile, based on hydraulic conductivity (K) values of $1x10^{-5}$ m s^{-1}. Following Equation (3), the flow is directly proportional to the assumed value of hydraulic conductivity taken from glacier aquifers. Since K has not been measured at our field site, we present the total

simulated flow rate as a first-order estimate only. Fluctuations in head translate to variations of drainage rates and therefore, the drainage rate is not constant throughout the aquifer. The local flow cells are strongly related to the local topography (Figure 3.14). Local surface depressions (vertical arrows on Figure 3.14) act as local recharge and discharge of the firn aquifer.

3.7. Discussion

3.7.1. Firn aquifer stability

The firn aquifer stability is studied at two specific locations, corresponding to the radar profiles upstream of Helheim and at our field location where repeated data are available. At the field location, the firn aquifer appears stable between 2011 and 2012, the snow surface lowered each year, and the water surface also lowered. The stability of the depth to water between these two years implies water discharge would accommodate new meltwater input, if any. The vertical rise (+1.2 m) of the water table observed in spring 2013 is likely due to a combination of an increase of surface melt in summer 2012 compared to 2011 and a reduction in snowfall prior to the data collection. Using the nearby AWSs, we confirm that the accumulated snowfall was 40% less in 2013 compared to the 2008-2014 average and the annual mass-loss in 2011 was ~5% below average, whereas 2012 was ~20% above average. However, the rise of the water table observed in 2013 could not only be caused by an increase of water volume storage. In fact, *Schneider* [1999] observed that the rise of the water table was of the same magnitude as the rise of firn/ice transition (~1.5 m y^{-1}) for the Storglaciären firn aquifer. In this study, the lack of radar signal penetration in the aquifer prevented us from making this observation. The

following winter (2013-2014) corresponded to another low snowfall season (50% less than 2008-2014 average) from the AWS data, but the aquifer is lowered to greater depth (-2.5 m). This lowering can be related to the lateral water movement in the aquifer, depleting the water from these elevations, associated with a limited input of new meltwater. From the AWS data, 2013 represented a relatively low melt year with an ablation rate 20% below average, confirming that less meltwater was produced.

The OIB repeated radar surveys located in the vicinity of Helheim Glacier present a strong case for partial drainage of the firn aquifer after spring 2012. Between 2012 and 2013, the aquifer disappeared at low elevations, but its water surface rose at higher elevations (Figure 3.11). The absence of radar reflectors can be due to (1) water drainage, (2) refreezing, or (3) lack of penetration of the AR signal. We favor the drainage hypothesis by ruling out the other two possibilities. First, it seems unlikely that after the above-average summer melt of 2012, significant quantities of water in the firn, which has been warmed for a few years, could refreeze at depth in less than one year. A liquid to solid phase change will produce a significant amount of latent heat to maintain the firn at near-temperate temperatures. A winter colder than average that would allow temperatures to penetrate at greater depth via conduction was not observed in the AWS temperature data. Second, the absence of a radar reflector can be due to thick ice layers preventing the radar signal to reach greater depth (>10 m). Since the radar attenuation depends on frequency, in the scenario where the AR signal at 750 MHz could be attenuated before getting to the depth of the water, the lower frequency MCoRDS system (195 MHz) should have been affected by the water. However, the MCoRDS profile presents a clear bed-echo return over the lower part of the profile, ruling out this third possibility (Figure

3.11). Therefore, we favor the first hypothesis consisting of draining the lower part of the aquifer. This drainage of a ~4-km section of the aquifer implies hydraulic gradients and hydraulic conductivity to be high enough to mobilize this volume of water and transport it out of the firn. If the low-elevation end of the firn aquifer is drained of its water for a few years, we could envisage a migration of the aquifer to higher elevations. The competing element is the seasonal production of meltwater supplying the water table. Even if summer 2013 melt was detected below average by the AWS located at TAS_L and TAS_U, 2014 melt season was above average and could lead to a possible refill of the aquifer in its lower-elevation parts for spring 2015.

3.7.2. Lateral deep water flow

The hydraulic gradient is a key driver of the water flow over the relatively flat surface of the Greenland ice sheet. For mountain-glacier aquifers, the hydraulic gradients can be up to 10 times greater for smaller lateral spatial extent; therefore, routing meltwater in a more efficient manner toward an exit prevents liquid water from overwintering. The hydraulic gradient is related to the firn aquifer thickness. For example, for mountain-glacier analogues, on Aletschgletscher, Switzerland, the lower hydraulic gradients result in a +2-m thicker aquifer compared to Storglaciären, Sweden, which is slightly steeper [*Jansson et al.*, 2003]. This observation is in agreement with the 25-m thick aquifer used in our simulation where the hydraulic gradient is lower than 1° in average. However, as the hydraulic gradients vary spatially following ice-sheet surface undulations, the aquifer thickness would not be kept constant.

In the percolation zone, the presence of ice lenses complicates water percolation. Horizontal ice lenses disrupt the vertical flow of water, which starts to flow horizontally [*Conway and Benedict*, 1994]. On the Devon ice cap and West Greenland, thick and continuous ice lenses are formed and meltwater pools above them, flows laterally upon surface topography, and ends up running off or refreezing at the end of the melt season [*Gascon et al.*, 2013]. At our field location, during the spring 2014, we observe with GPR the slow downstream migration of liquid water at depth, following hydraulic gradients (Figure 3.15). In this figure, the water surface happens to diverge from the water table while the surface slope is reaching 0°. A thick ice layer, which creates an impermeable boundary, could have been encountered by the water. The water pools on this horizon and expends laterally, slowly flowing downstream at the firn ice interface, saturating the above firn. This feature is interpreted as a perched water layer on top of the firn aquifer. The sharp end of the reflector on the flat side of the radar profile implies that the data collected happened during the water migration. In concordance with low hydraulic gradients, we infer a slow lateral motion during the winter, but we did not monitor its changes in real time. This observation is consistent with observations from *Humphrey et al.* [2012] that deep pore water slowly migrates down glacier under low hydraulic gradients.

Based on our hydraulic simulations, flow cells have been revealed, with transition to flatter locations allowing local discharge to occur, indicating local flow behavior in the larger firn aquifer (Figure 3.14). Such local discharge features in the form of thicker ice layers or perched water table (Figure 3.15) with a possible surface expression have not been observed at our field location. In west Greenland, *Humphrey et al.* [2012] observed

the presence of pingo-type features (usually found in permafrost) forming at similar locations to our local water discharge simulations (Figure 3.14), when the slope transitions from steep to flat. In Southeast Greenland, the frequent snowfalls occurring before and during spring fieldwork could mask a possible pingo's surface expression, and no GPR evidences of this feature have been detected yet.

3.7.3. Previous existence of the aquifer

Evidence of the firn aquifer as early as airborne radar records exist for Southeast Greenland (in 1993) implies the nonsynchronicity of the aquifer formation and the increased melt of the last decade (2002-2012). However, the recent aquifer expansion (in locations where repeated data exist) implies that its extent may be influenced by the recent surface melt increases over the last decade. Prior to 2012, the aquifer was limited to a 3-km strip for the area upstream of Helheim Glacier (Figure 3.10). For 2004-2006, a 2-km long drainage of the low-elevation part is suspected based on the Figure 3.10. The lack of measurements between 2009 and 2012 does not allow inspection of the timing of the aquifer upstream expansion. However, the spatial variability of the firn aquifer, linked to the surface undulations and hydraulic gradient, guides the presence of an aquifer where only significant slope gradients seem to allow its formation (vertical black arrows on Figure 3.10).

Past firn aquifers, prior to the instrumentation record, will leave an imprint at greater depth as heat is trapped during the phase transition from water-saturated firn to ice. The high snow accumulation of these regions allows the firn to be buried at a faster rate compared to low-accumulation regions. The slow lateral flow of water down glacier

is competing with compaction squeezing the water out of the pore space during the densification process [*Koenig et al.*, 2014]. Over longer time scales, the signature of a buried water-saturated layer in the firn should remain at greater depth and warmer ice would be observed. This ice imprint of such temperate conditions in the firn has been recently recorded by *Lüthi et al.*, [2014] in the ablation zone of the western Greenland ice sheet. The direct impact of warmer ice is related to the cryo-hydrologic warming [*Phillips et al.*, 2013].

3.7.4. Firn aquifer impacts

The aquifer impacts ice sheet mass balance in three ways: firn densification, contribution to runoff, and ice dynamics. Increased firn densification and its warming is noted for the last decades over the Greenland ice sheet [*Harper et al.*, 2012; *Polashenski et al.*, 2014] and the Devon ice cap [*Bezeau et al.*, 2013] percolation zones. The repeated ATM observations of the flightline upstream of Helheim (45 km from calving front) (Figure 3.10) give a relatively stable snow surface between 1998 and 2003 followed by a 10-m lowering between 2003 and 2013. For the last decade, dynamic thinning and firn densification are important [*Csatho et al.*, 2014]. For the percolation zone in West Greenland, the available pore space in the firn is being filled with meltwater that refreezes, temporally filling the firn by an increased presence of ice lenses until capacity is reached [*Harper et al.*, 2012]. For the aquifer detected at our field location, with a limited period of investigation (2011-2013), we obtained surface elevation changes (Figure 3.9) and firn-core ice fraction to the top of the water table (Table 3.2). Despite the surface lowering, we did not observe a significant interannual increase of the ice fraction

in the snow/firn stratigraphy above the aquifer due to refreezing of water in the firn, even after the important summer melt year of 2012. In an aquifer configuration, the liquid water content might not be refreezing as much in the firn once the seasonal snow is traversed by meltwater. The holding capacity of the firn by capillary forces is lower (~4%) and the water makes its way at a faster rate to the firn/ice transition [*Schneider and Jansson*, 2004]. At greater depth, the water is less subject to refreezing in the fall since freshly fallen snow will keep insulating a previously warmed firn.

If the meltwater does not contribute to significantly increase the ice fraction of the firn above the water table by refreezing, slow runoff of the water at depth under low hydraulic gradient is suggested. It is not clear from the radar dataset what the fate of the water drained from the firn aquifer is. When crevasses are encountered along aquifer flightlines, in most cases, no more bright reflectors are found at depth, suggesting that the water could have drained into the crevasses and either refroze in them or found englacial pathways toward the glacier bed. On smaller-scale mountain glaciers, the firn aquifer is intimately linked to the englacial network via crevasses and moulins [*Fountain and Walder*, 1998], allowing meltwater to access the bed after being delayed in the aquifer. In Greenland, similar englacial pathways have been observed [e.g., *Catania and Neumann*, 2010]. However, meltwater exiting the aquifer and reaching the bedrock has not been observed yet. The consequences of delaying/suppressing meltwater flow to the bed can be related to seasonal changes in glacier velocity in Southeast Greenland [*Moon et al.*, 2014]. For the studied aquifer location, the ice thickness is > 800 m and mainly moulins can bring water to depth, but their formation seems limited due to important ice thickness and water supply. Indeed, enough water would need to flow at a high rate to keep up with

the crevasse penetration rate to bring aquifer water to the bed [e.g., *van der Veen*, 2007]. The drainage event inferred between spring 2012 and 2013 using radar data does not provide the temporal resolution to determine if the drainage was constant throughout the fall and winter or if it led to a more sudden release event. However, the low hydraulic gradients combined with a low hydraulic conductivity favor the first hypothesis.

3.8. Conclusions

Widespread firn aquifers can be detected directly or inferred over high accumulation regions of the Greenland ice sheet by a variety of radars systems: a 195 MHz radar depth sounder, a 750 MHz Accumulation Radar, and a 400 MHz ground penetrating radar. A total linear distance of 2420 km of the firn aquifer has been observed and mapped using the AR between spring 2011 and spring 2013 in the lower part of the percolation zone (wet-snow zone). The firn aquifer is found at an average elevation of 1600±220 m (±1σ) and the average depth to the water table (top of the aquifer) is 22±8 m (±1σ). Driven by low hydraulic gradients (average of 0.6°), the water in the aquifer travels down glacier following the ice-sheet surface undulations. For the 2011-2014 period at the field site, the water table remained spatially stable and only fluctuated vertically (less than 2.5 m) due to the ice-sheet surface conditions (melt and accumulation). The water table rose after the 2012 summer surface melt and declined two years later, in the spring of 2014. Within the firn aquifer, local flow cells are simulated and their lateral limits are related to the surface topography with water recharge and discharge located at the steep-to-flat transitions. Strong surface slope gradients are likely required to collect enough meltwater to initiate a firn aquifer. Upstream of Helheim

glacier, the presence of an aquifer is inferred from missing bed echoes in 1993 using CReSIS archived data. The aquifer remained spatially stable between 1993 and 2008. After 2008, this aquifer expands to higher elevations due to increased surface melt toward the interior of the ice sheet producing enough water to reach greater depth in the deep pore space of the firn. After spring 2012, drainage of its lower-elevation portion is suspected. The fate of the water leaving the aquifer and its connection to englacial pathways is unknown. The storage of meltwater from the aquifer in crevasses would warm the ice in their vicinity by refreezing and releasing latent heat. If the amount of water draining out of the aquifer into a crevasse is sufficient for hydrofracturing, the water could reach the bed and impact the ice dynamics.

The densification scheme observed in West Greenland consisting of filling available pore space with refrozen meltwater [*Harper et al.*, 2012] cannot be fully applied here as the water will transit for a certain time within the firn without refreezing and will potentially exit the aquifer at lower elevations. This process needs to be taken into account in order to convert surface changes to mass changes. Additional field observations are required to better constrain the hydraulic variables (conductivity, water age, and residence time), water volume mobilized in the aquifer, and quantify volumetric flow rate out of the aquifer system.

3.9. Acknowledgements

Thanks to NASA Operation IceBridge mission and the CReSIS radar team, for the high-quality airborne data that made this study possible. C. Miège acknowledges NASA ESS Fellowship program (NNX11AL64H). US National Science Foundation with grants

OPP-0909499 and EAGER-1311655 supported work in 2011 and 2013, respectively. J. Box and R. Fausto are supported by the Det Frie Forskningsråd of Denmark grant DFF – 4002-00234. Thanks to the 2011 and 2013 field team members: B. Ballard, T. Gacke, and J. Kyne. Thanks to the following institutions for fieldwork support: CH2MHILL, IDDO, 109th Air National Guard, Air Greenland, UNAVCO. Thanks to G. Roth at the Polar Geospatial Center for preparing the DigitalGlobe© images. The firn aquifer map and depth to the water table will be available for download at nsidc.org/acadis after publication.

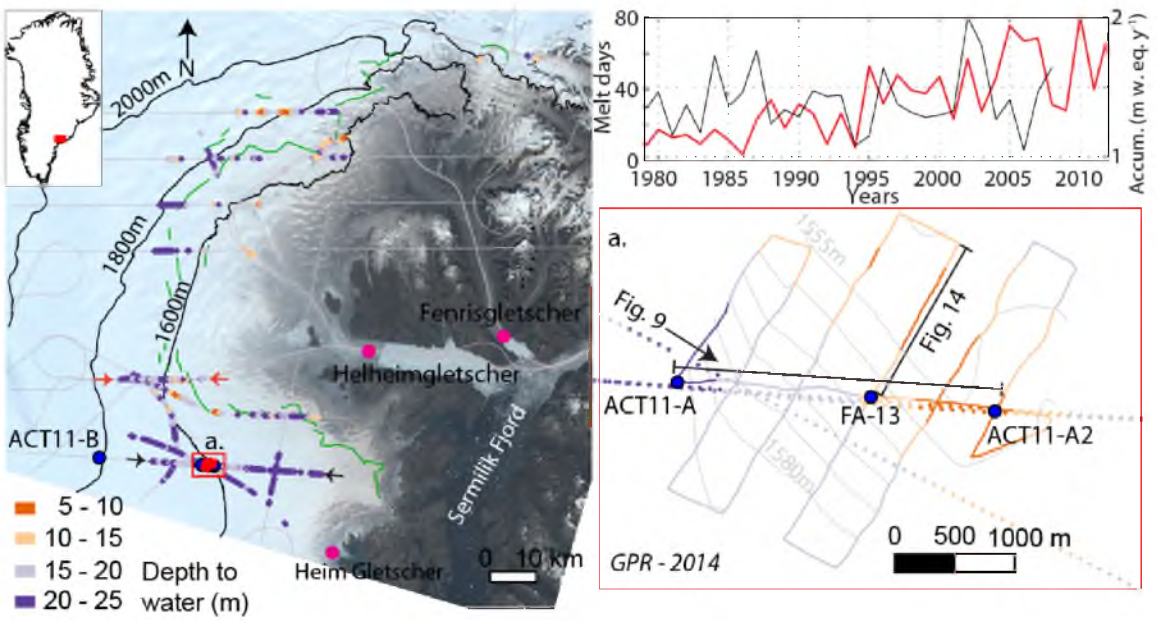

Figure 3.1: Landsat 8 composite image (on 21 August 2014) over the field site area. Firn aquifer locations are color coded by depth to the water table. OIB flight lines are gray. Firn core locations are represented by blue dots, with a two-digit number corresponding to year of collection. Green lines indicate last upstream crevasse visible from L-band SAR imagery [*Moon and Joughin* 2008]. Elevation contours (black) are from the 30-m resolution GIMP DEM [*Howat et al.*, 2014]. Magenta circles indicate main outlet glaciers [*Rignot and Mouginot*, 2012]. Inset a) detail inside red box with diamonds for airborne depth to water table and lines for the 2014 GPR. Gray elevation contours are obtained from linear interpolation of the GPS grid. Top right inset represents number of melt days (red) [*Mote*, 2014] and simulated accumulation rates (black) [*Burgess et al.*, 2010] at the FA-13 firn core.

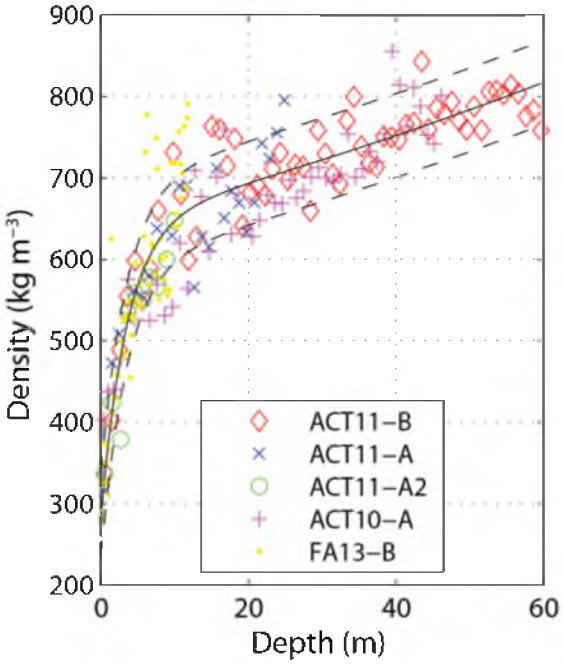

Figure 3.2: Density profiles for five firn cores extracted in Southeast Greenland (Figure 3.1) used for the TWT to depth conversion. Only ACT10-A and ACT11-B are not drilled above the firn aquifer. We use a bi-exponential function to fit the data (solid black) ± 1 standard deviation (dash).

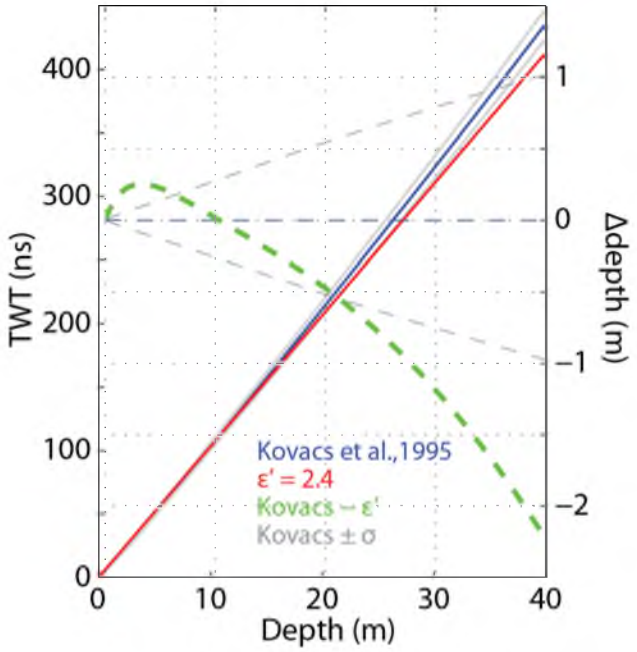

Figure 3.3: Two-way-travel time as a function of depth calculated with two methods: density adjusted (blue) or with a constant dielectric constant at depth (red). Solid lines are related to the left-y axis (TWT), whereas dashed lines are related to the right-y axis (Δdepth). Using an invariant dielectric constant correction can introduce an error up to 2 m at 40-m depth (thick green). 1 σ from the density profile (±53.3 kg m^{-3}) leads to a maximum uncertainty of ±1 m at 40-m depth (gray lines).

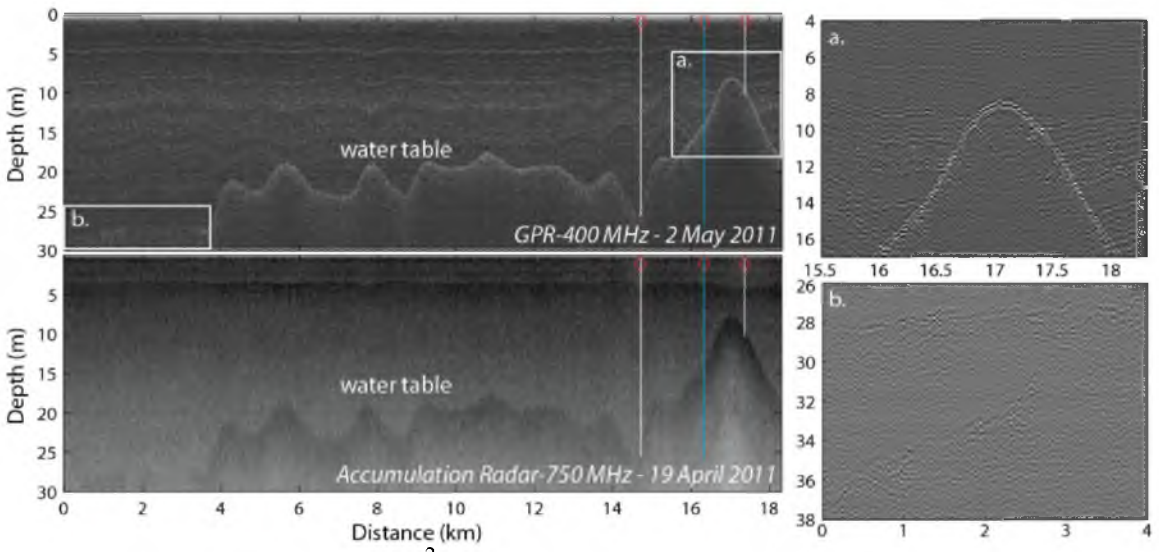

Figure 3.4: Direct comparison (r^2=0.99) between GPR (400 MHz; May 2, 2011) and AR (750 MHz; April 19, 2011) over an 18-km portion of ACT-11 traverse (transect is located between the two black arrows on the map of Figure 3.1). The 3 boreholes (red diamonds) confirm the presence of water at the bright reflector depth. Insets a) and b) show details of the GPR data over certain distances and depths.

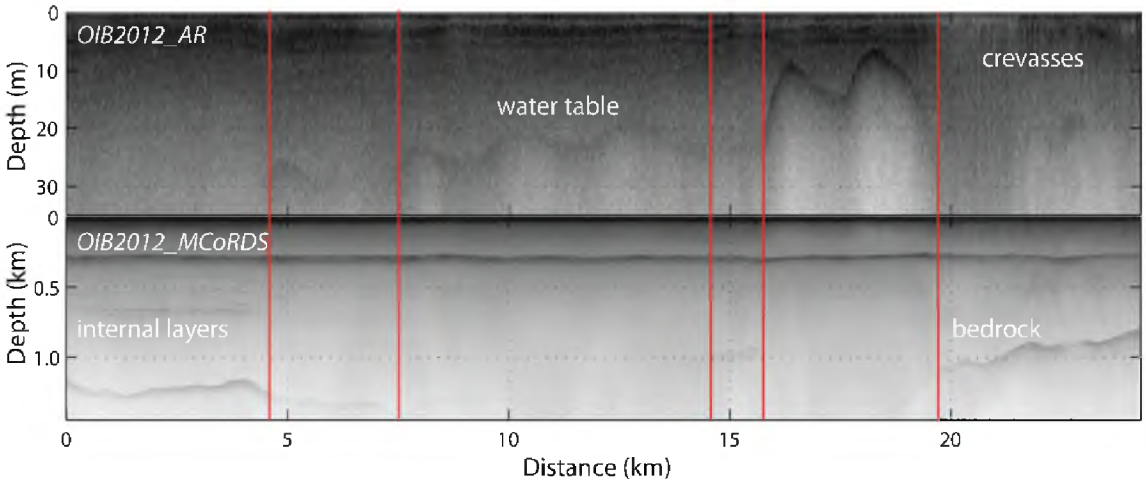

Figure 3.5: Comparison between the AR at 750MHz (top) and the MCoRDS at 195MHz (bottom) over the firn aquifer for Apr. 17, 2012. The lack of internal layering and bed return is related to the presence of the firn aquifer. The red vertical lines highlight transitions in both radar profiles.

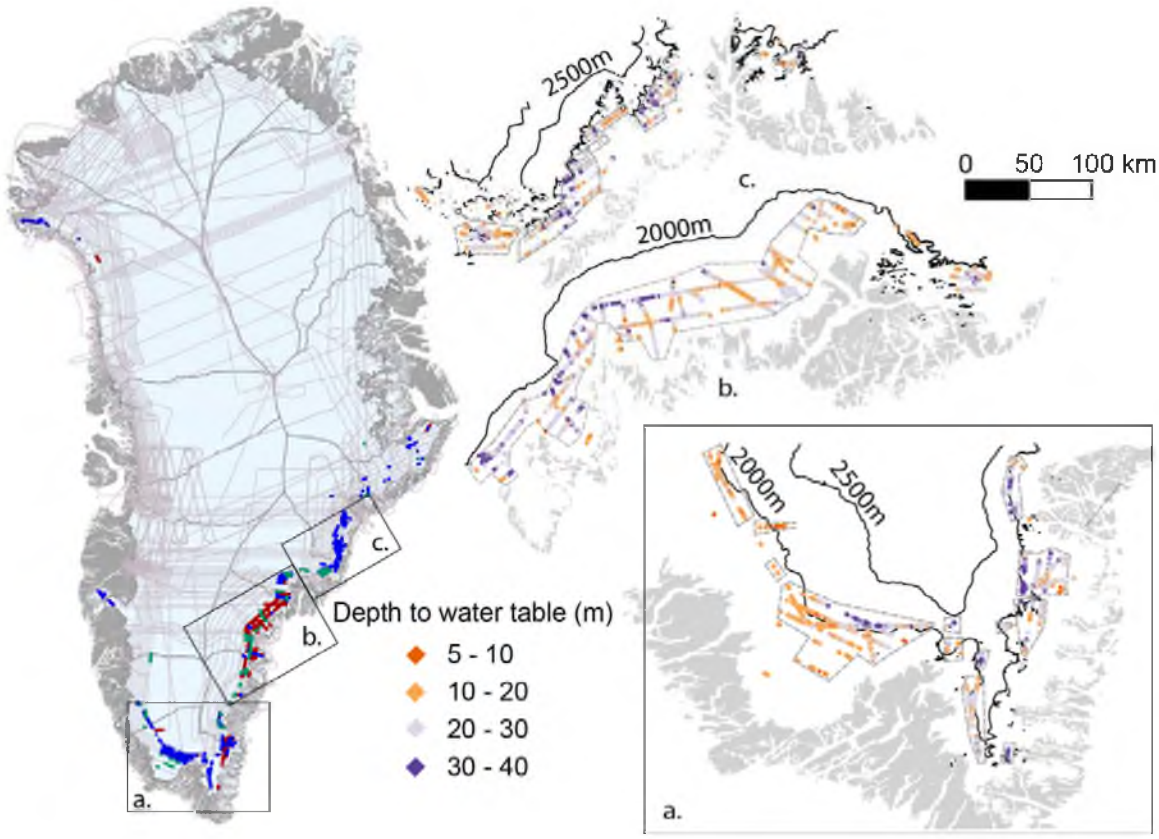

Figure 3.6: Greenland map: Spring detection of water table using OIB Accumulation Radar for 2011 (red), 2012 (blue), and 2013 (green). OIB flightlines are represented in light gray. The different insets show the depth of the firn aquifer surface. Note that insets b. and c. have a 30° angle from the North. Dashed-gray polygons were used to estimate aquifer extents. Ice mask and DEM are from *Howat et al.* [2014]. Coastline is from *Rignot and Mouginot* [2012].

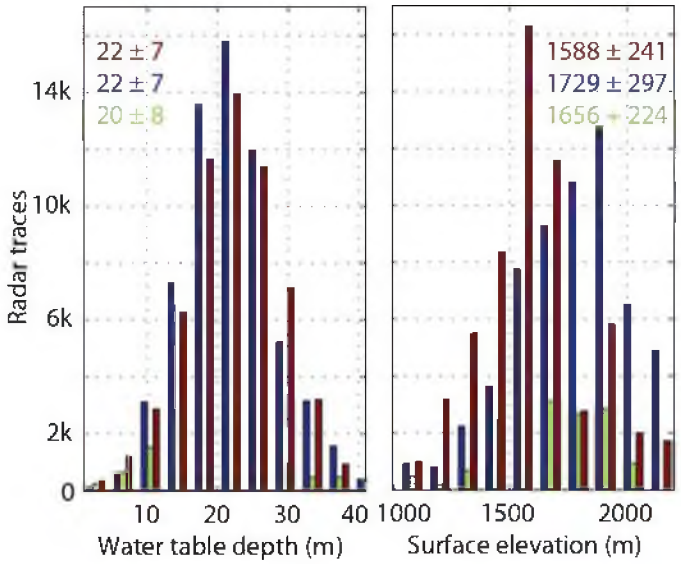

Figure 3.7: Water table depth (left) and surface elevation (right) distribution from three years of radar data: OIB2011 (red), 2012 (blue), and 2013 (green). Mean and ±1 standard deviation are given for each year.

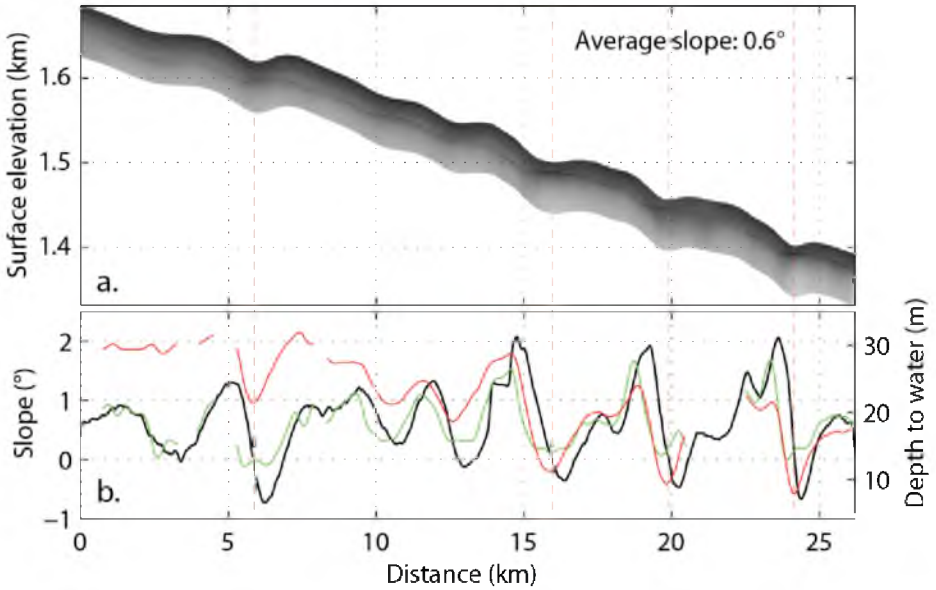

Figure 3.8: a) Airborne radar profile (2011) of the water table surface corrected for topography in direction perpendicular to elevation contours. b) Relationship between the water table depth (red), the surface slope (black), and water surface slope (green). The red vertical dashed lines illustrate the local water surface depth minimum (red) observed when the surface slope (black) intersects 0.

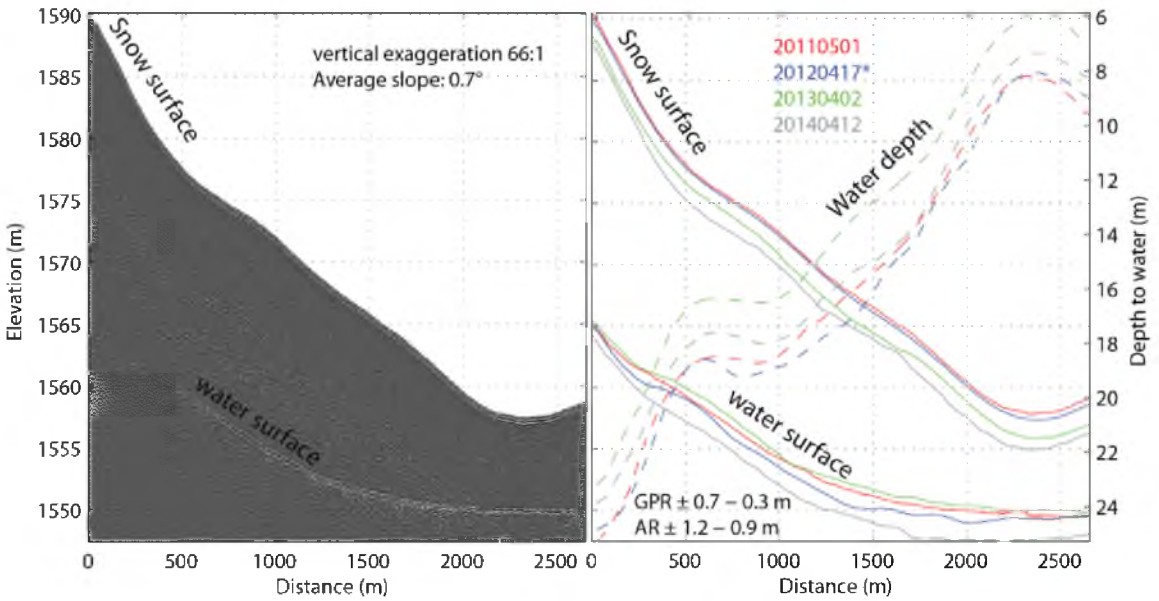

Figure 3.9: Temporal evolution of the depth to the water table from GPR for four consecutive years between sites ACT11-A to ACT11-A2 (Figure 3.1). Left panel, the GPR profile is taken in 2011. Right panel, solid lines are related to the left y axis (elevation) whereas dashed lines are related to the right y axis (depth to water). The 2012 profile is obtained from airborne radar. The maximum horizontal distance between two transects is 70 m. The water table elevation uncertainty range corresponds to each end of the profile.

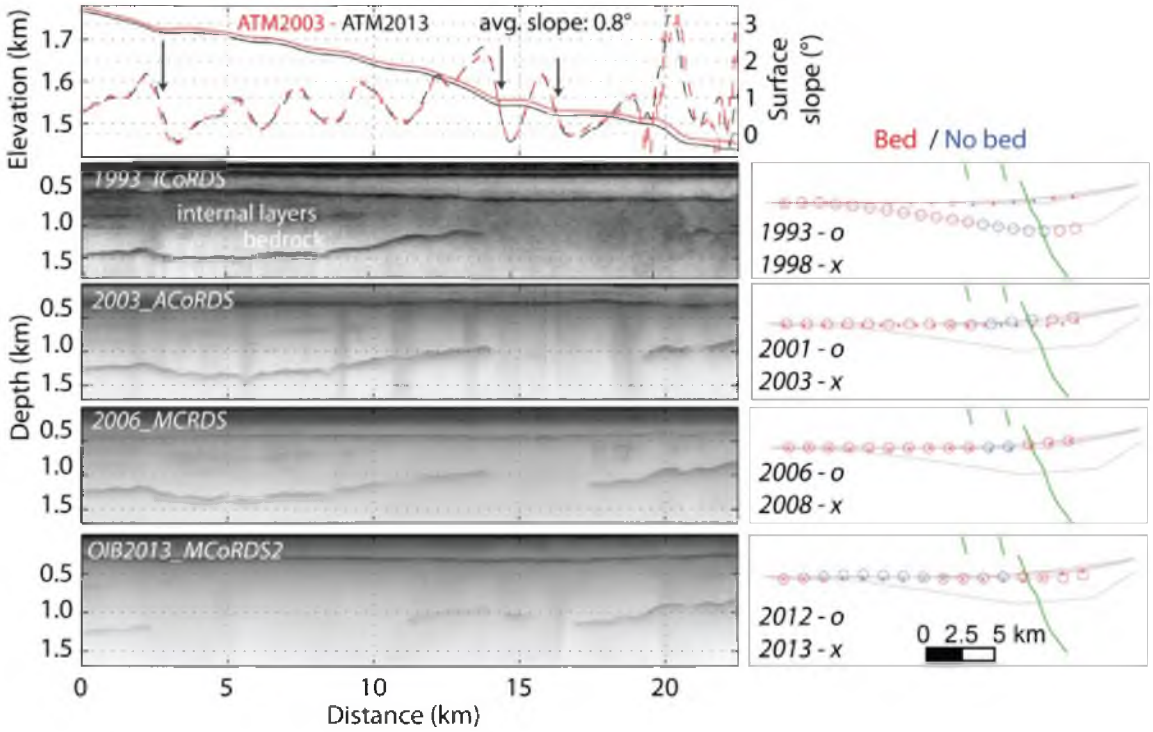

Figure 3.10: Missing bed echoes over the last two decades related to the presence of water in the firn. Note that the 1993 data are not aligned with the other radar profiles (~2 km south). Top left panel presents two ATM variables for 2003 (red) and 2013 (black): elevation (solid) and slope (dash). Black vertical arrows illustrate strong slope gradients at the high-elevation limit of the aquifer. Left panels present radar depth-sounder profiles for 1993-2013. Right panels overlay airborne flightlines and the presence (blue) or absence (red) of a firn aquifer is inferred from the lack of bed returns. Upper crevasses (green) are mapped using L-band imagery [*Moon and Joughin*, 2008].

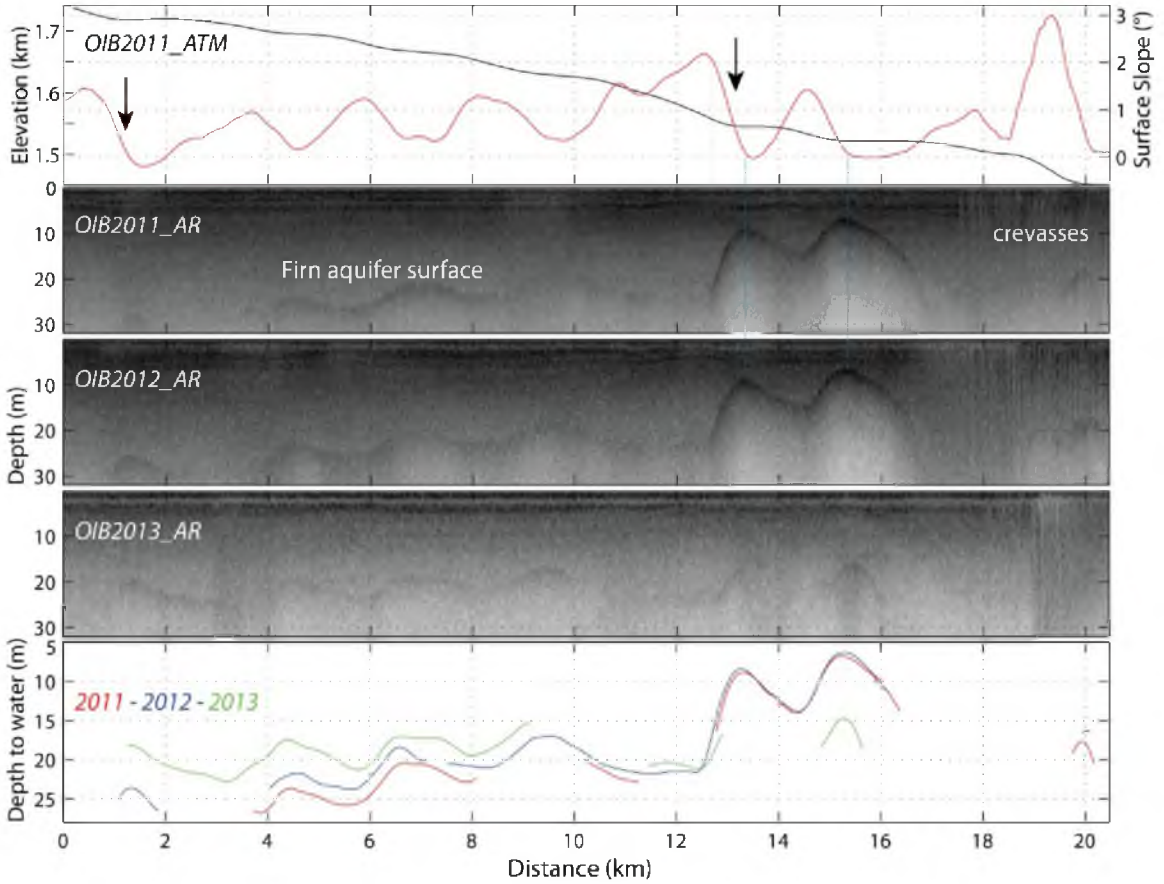

Figure 3.11: Yearly evolution of the water table surface between spring 2011 and 2013 upstream of Helheim Glacier (between red arrows on Figure 3.1). The top panel represents the elevation (ATM, black) and surface slope (red) profiles. The lower panel corresponds to the depth of the water retrieve from the three AR profile above taken over repeated flightlines. The maximum distance between two flightlines is 220 m. Blue vertical lines illustrate water surface patterns.

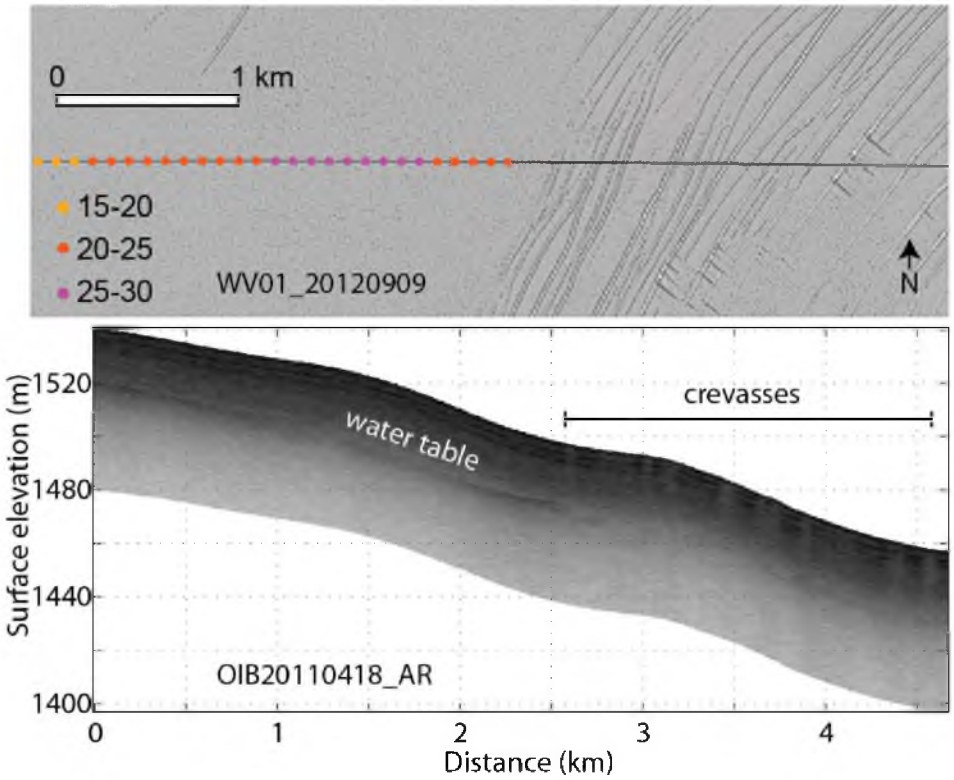

Figure 3.12: Lower-elevation end of the firn aquifer with crevasses. Top panel image is a WorldView 1 image from DigitalGlobe© with a 0.5 m resolution. Colors represent depth to the water table in m. The radar profile is located in the Køge Bugt bay (65.2°N 51.5°W) upstream of Glacier C (left) [Glacier name from *Rignot and Mouginot*, 2012].

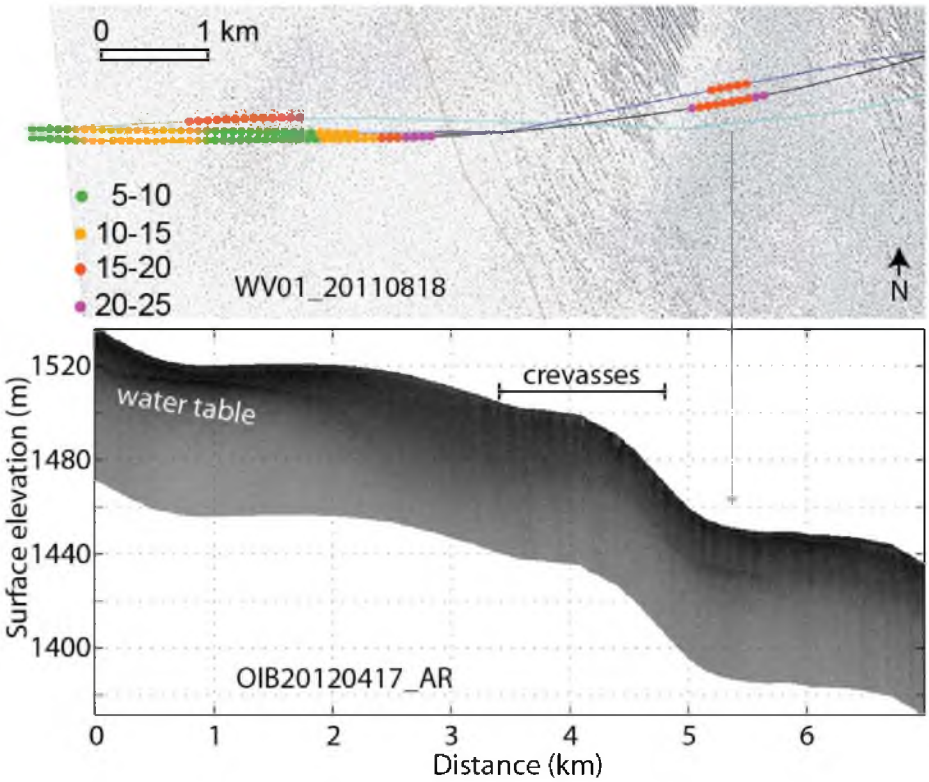

Figure 3.13: Second example of aquifer and crevasse connection. Top panel image is a WorldView 1 image from DigitalGlobe© with a 0.5 m resolution. Colors represent depth to the water table in m. Flightlines in blue, black and cyan represents OIB 2011, 2012, and 2013, respectively. The radar profile is located upstream of Helheim glacier, corresponding to km 15 to 20 on Figure 3.11.

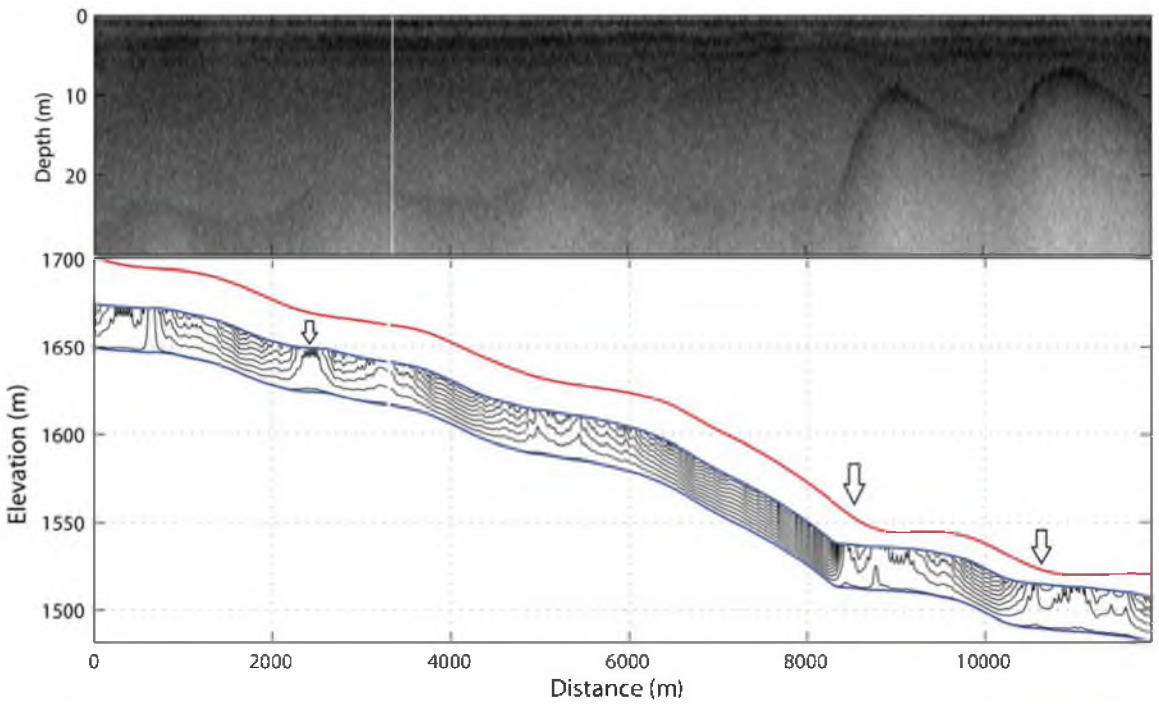

Figure 3.14: Top panel, AR profile for OIB2012 upstream of Helheim glacier (identical to 3rd panel on Figure 3.11). Bottom panel, we simulate flowlines (black) using the water table elevation for boundary conditions (blue). Vertical arrows represent main local discharge locations. Snow surface (red) is obtained from ATM data collected simultaneously than the radar.

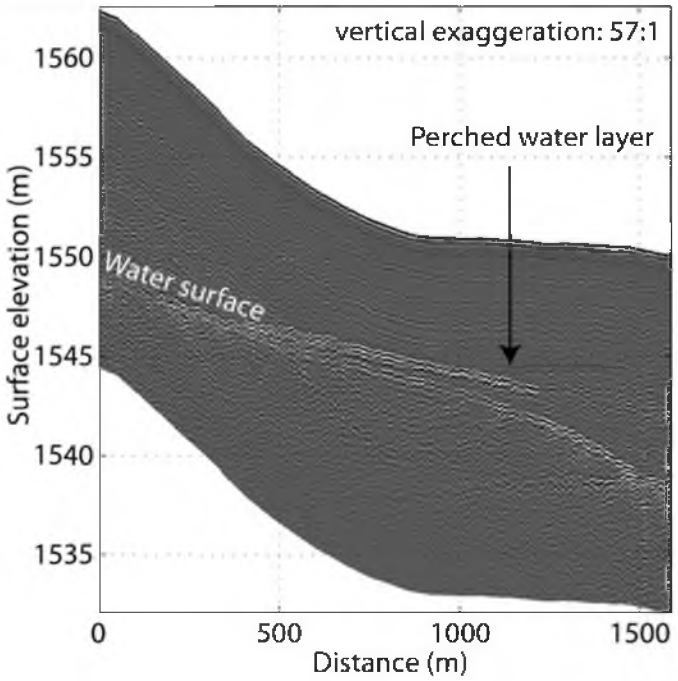

Figure 3.15: Near along-flow GPR profile collected in April 2014, corrected for surface elevation, over a 1.5km segment (Figure 3.1). A perched water table is observed ~1-2m above the firn aquifer surface, likely ponding on a thick ice layer and traveling down glacier.

Table 3.1: OIB flight campaign characteristics for to the aquifer regions using the AR

OIB flight campaign	Total flightlines (km)	Total linear distance with aquifer (km)	Aquifer-repeat tracks (km) 2011 | 2012 | 2013			Aquifer deduced area (km^2)
2011	119,810	1,030	-	335	75	-
2012	169,200	1,105	335	-	80	-
2013	148,760	285	75	80	-	-
Total	437,770	2,420	450	415	155	28,500

Table 3.2: Location and stratigraphy of the different firn cores collected during fieldwork (Figure 3.1). The two-digit numbers in the firn-core names give the year of collection. Note that FA13-A and B are located 1.5 m apart.

Firn cores	Elevation (m)	Depth to water (m)	Ice fraction (%)
ACT11-A	1589	25	14
ACT11-A2	1559	10	7
FA13-A	1563	12.2	9
FA13-B*	1563	12.2	8

3.10. References

Ahlstrøm, A.P. and the PROMICE project team (2008), A new programme for monitoring the mass loss of the Greenland ice sheet, *In: Bennike, O. & Higgins, A.K.(eds): Review of Survey activities 2007. Geological Survey of Denmark and Greenland Bulletin 15,* 61-64.

Benson, C. S. (1962), *Stratigraphic studies in the snow and firn of the Greenland Ice Sheet. U.S. Snow, Ice and Permafrost Research Establishment*, U.S. Snow, Ice and Permafrost Research Establishment Research Rep.

Bezeau, P., M. Sharp, D. Burgess, and G. Gascon (2013), Firn profile changes in response to extreme 21st-century melting at Devon Ice Cap, Nunavut, Canada, *Journal of Glaciology*, *59*(217), 981–991, doi:10.3189/2013JoG12J208.

Box, J. E., A. Ahlstrøm, J. Cappelen, X. Fettweis, D. Decker, T. Mote, D. van As, R. S. W. van de Wal, B. Vinther, and J. Wahr (2011), Greenland [in "State of the Climate in 2010"], *Bull. Amer. Meteor. Soc.*, *92*(6), S161–171.

Bradford, J. H., J. T. Harper, and J. Brown (2009), Complex dielectric permittivity measurements from ground-penetrating radar data to estimate snow liquid water content in the pendular regime, *Water Resour. Res.*, *45*(8), W08403, doi:10.1029/2008WR007341.

Brown, J., J. Harper, W. T. Pfeffer, N. Humphrey, and J. Bradford (2011), High-resolution study of layering within the percolation and soaked facies of the Greenland ice sheet, *Annals of Glaciology*, *52*(59), 35–42, doi:10.3189/172756411799096286.

Burgess, E. W., R. R. Forster, J. E. Box, E. Mosley-Thompson, D. H. Bromwich, R. C. Bales, and L. C. Smith (2010), A spatially calibrated model of annual accumulation rate on the Greenland Ice Sheet (1958–2007), *Journal of Geophysical Research: Earth Surface*, *115*(F2), n/a–n/a, doi:10.1029/2009JF001293.

Catania, G. A., and T. A. Neumann (2010), Persistent englacial drainage features in the Greenland Ice Sheet, *Geophysical Research Letters*, *37*(2), n/a–n/a, doi:10.1029/2009GL041108.

Cogley, J.G., R. Hock, L.A. Rasmussen, A.A. Arendt, A. Bauder, R.J. Braithwaite, P. Jansson, G. Kaser, M. Möller, L. Nicholson and M. Zemp (2011), Glossary of Glacier Mass Balance and Related Terms, *IHP-VII Technical Documents in Hydrology No. 86, IACS Contribution No. 2, UNESCO-IHP, Paris.*

Colbeck, S. C. (1975), A theory for water flow through a layered snowpack, *Water Resources Research*, *11*(2), 261–266, doi:10.1029/WR011i002p00261.

Coléou, C., and B. Lesaffre (1998), Irreducible water saturation in snow: Experimental results in a cold laboratory, *Annals of Glaciology*, *26*, 64–68.

Conway, H., and R. Benedict (1994), Infiltration of water into snow, *Water Resour. Res.*, *30*(3), 641–649, doi:10.1029/93WR03247.

Csatho, B. M., A. F. Schenk, C. J. van der Veen, G. Babonis, K. Duncan, S. Rezvanbehbahani, M. R. van den Broeke, S. B. Simonsen, S. Nagarajan, and J. H. van Angelen (2014), Laser altimetry reveals complex pattern of Greenland Ice Sheet dynamics, *PNAS*, *111*(52), 18478–18483, doi:10.1073/pnas.1411680112.

Doolittle, J. A., B. Jenkinson, D. Hopkins, M. Ulmer, and W. Tuttle (2006), Hydropedological investigations with ground-penetrating radar (GPR): Estimating water-table depths and local ground-water flow pattern in areas of coarse-textured soils, *Geoderma*, *131*(3–4), 317–329, doi:10.1016/j.geoderma.2005.03.027.

Enderlin, E. M., I. M. Howat, S. Jeong, M.-J. Noh, J. H. van Angelen, and M. R. van den Broeke (2014), An improved mass budget for the Greenland ice sheet, *Geophys. Res. Lett.*, *41*(3), 2013GL059010, doi:10.1002/2013GL059010.

Forster, R. R. et al. (2014), Extensive liquid meltwater storage in firn within the Greenland ice sheet, *Nature Geosci*, *7*(2), 95–98, doi:10.1038/ngeo2043.

Fountain, A. G. (1989), The storage of water in, and hydraulic characteristics of, the firn of South Cascade Glacier, Washington State, U.S.A., *Annals of Glaciology*, *13*, 69–75.

Fountain, A. G. (1996), Effect of snow and firn hydrology on the physical and chemical characteristics of glacial runoff, *Hydrol. Process.*, *10*(4), 509–521, doi:10.1002/(SICI)1099-1085(199604)10:4<509::AID-HYP389>3.0.CO;2-3.

Fountain, A. G., and J. S. Walder (1998), Water flow through temperate glaciers, *Rev. Geophys.*, *36*(3), PP. 299–328, doi:199810.1029/97RG03579.

Gascon, G., M. Sharp, D. Burgess, P. Bezeau, and A. B. G. Bush (2013), Changes in accumulation-area firn stratigraphy and meltwater flow during a period of climate warming: Devon Ice Cap, Nunavut, Canada, *J. Geophys. Res. Earth Surf*, *118*(4), 2013JF002838, doi:10.1002/2013JF002838.

Gogineni, S. P. (2012), IceBridge MCoRDS geolocated radar echo strength profiles. April-May 2012, *Boulder, Colorado USA: NASA DAAC at the National Snow and Ice Data Center*.

Hanna, E., X. Fettweis, S. H. Mernild, J. Cappelen, M. H. Ribergaard, C. A. Shuman, K. Steffen, L. Wood, and T. L. Mote (2013), Atmospheric and oceanic climate forcing of

the exceptional Greenland ice sheet surface melt in summer 2012, *International Journal of Climatology*, doi:10.1002/joc.3743.

Harper, J., N. Humphrey, W. T. Pfeffer, J. Brown, and X. Fettweis (2012), Greenland ice-sheet contribution to sea-level rise buffered by meltwater storage in firn, *Nature*, *491*(7423), 240–243, doi:10.1038/nature11566.

Howat, I. M., B. E. Smith, I. Joughin, and T. A. Scambos (2008), Rates of southeast Greenland ice volume loss from combined ICESat and ASTER observations, *Geophys. Res. Lett.*, *35*(17), L17505, doi:10.1029/2008GL034496.

Howat, I. M., A. Negrete, and B. E. Smith (2014), The Greenland Ice Mapping Project (GIMP) land classification and surface elevation data sets, *The Cryosphere*, *8*(4), 1509–1518, doi:10.5194/tc-8-1509-2014.

Humphrey, N. F., J. T. Harper, and W. T. Pfeffer (2012), Thermal tracking of meltwater retention in Greenland's accumulation area, *J. Geophys. Res.*, *117*, 11 PP., doi:201210.1029/2011JF002083.

Jansson, P., R. Hock, and T. Schneider (2003), The concept of glacier storage: A review, *Journal of Hydrology*, *282*(1–4), 116–129, doi:10.1016/S0022-1694(03)00258-0.

Jones, N.L. (1999), SEEP2D Primer, *Environmental Modeling Research Laboratory, Brigham Young University, Provo, Utah.*

Koenig, L. S., C. Miège, R. R. Forster, and L. Brucker (2014), Initial in situ measurements of perennial meltwater storage in the Greenland firn aquifer, *Geophysical Research Letters*, *41*, 1–5, doi:10.1002/2013GL058083.

Kovacs A., Gow A.J., and Morey R.M. (1995), The in-situ dielectric constant of polar firn revisited, *Cold Regions Science and Technology*, *23*(3), 245–256, doi:10.1016/0165-232X(94)00016-Q.

Krabill, W. B. (2011), IceBridge ATM L2 Icessn elevation, slope, and roughness, *Boulder, Colorado USA: NASA DAAC at the National Snow and Ice Data Center*.

Krabill, W. B., W. Abdalati, E. B. Frederick, S. S. Manizade, C. F. Martin, J. G. Sonntag, R. N. Swift, R. H. Thomas, and J. G. Yungel (2002), Aircraft laser altimetry measurement of elevation changes of the greenland ice sheet: Technique and accuracy assessment, *Journal of Geodynamics*, *34*(3–4), 357–376, doi:10.1016/S0264-3707(02)00040-6.

Kuipers Munneke, P., S. R. M. Ligtenberg, M. R. van den Broeke, J. H. van Angelen, and R. R. Forster (2014), Explaining the presence of perennial liquid water bodies in the firn of the Greenland Ice Sheet, *Geophys. Res. Lett.*, *41*(2), 476–483, doi:10.1002/2013GL058389.

Leuschen, C., C. Lewis, P. Gogineni, F. Rodriguez-Morales, J. Paden, and J. Li (2011), IceBridge accumulation radar 11b geolocated radar echo strength profiles. April-May 2012, *Boulder, Colorado USA: NASA DAAC at the National Snow and Ice Data Center*.

Lüthi, M. P., C. Ryser, L. C. Andrews, G. A. Catania, M. Funk, R. L. Hawley, M. J. Hoffman, and T. A. Neumann (2014), Excess heat in the Greenland Ice Sheet: Dissipation, temperate paleo-firn and cryo-hydrologic warming, *The Cryosphere Discuss.*, *8*(5), 5169–5193, doi:10.5194/tcd-8-5169-2014.

McGrath, D., W. Colgan, N. Bayou, A. Muto, and K. Steffen (2013), Recent warming at Summit, Greenland: Global context and implications, *Geophysical Research Letters*, *40*(10), 2091–2096, doi:10.1002/grl.50456.

Miège, C., R. R. Forster, J. E. Box, E. W. Burgess, J. R. McConnell, D. R. Pasteris, and V. B. Spikes (2013), Southeast Greenland high accumulation rates derived from firn cores and ground-penetrating radar, *Annals of Glaciology*, *54*(63), 322–332, doi:10.3189/2013AoG63A358.

Mireault, Y., P. Tetreault, F. Lahaye, P. Heroux, and J. Kouba (2008), Online precise point positioning: A new, timely service from Natural Resources Canada.(INNOVATION), *GPS World*.

Moon, T., and I. Joughin (2008), Changes in ice front position on Greenland's outlet glaciers from 1992 to 2007, *J. Geophys. Res.*, *113*(F2), F02022, doi:10.1029/2007JF000927.

Moon, T., I. Joughin, B. Smith, M. R. van den Broeke, W. J. van de Berg, B. Noël, and M. Usher (2014), Distinct patterns of seasonal Greenland glacier velocity, *Geophys. Res. Lett.*, *41*(20), 2014GL061836, doi:10.1002/2014GL061836.

Mote, T. L. (2014), MEaSUREs Greenland Surface Melt Daily 25km Ease-Grid 2.0., *Boulder, Colorado USA: NASA DAAC at the National Snow and Ice Data Center*.

Oerter, H. and Moser, H. (1982), Water storage and drainage within the firn of a temperate glacier (Vernagtferner, Oetztal Alps, Austria), *In Hydrological Aspects of Alpine and High-Mountain Areas*, *138*, 71–81.

Parry, V., P. Nienow, D. Mair, J. Scott, B. Hubbard, K. Steffen, and D. Wingham (2007), Investigations of meltwater refreezing and density variations in the snowpack and firn within the percolation zone of the Greenland ice sheet, *Annals of Glaciology*, *46*(1), 61–68, doi:10.3189/172756407782871332.

Pfeffer, W. T., and N. F. Humphrey (1996), Determination of timing and location of water movement and ice-layer formation by temperature measurements in sub-freezing snow, *Journal of Glaciology*, *42*(141), 292–304.

Phillips, T., H. Rajaram, W. Colgan, K. Steffen, and W. Abdalati (2013), Evaluation of cryo-hydrologic warming as an explanation for increased ice velocities in the wet snow zone, Sermeq Avannarleq, West Greenland, *J. Geophys. Res. Earth Surf*, *118*(3), 1241–1256, doi:10.1002/jgrf.20079.

Polashenski, C., Z. Courville, C. Benson, A. Wagner, J. Chen, G. Wong, R. Hawley, and D. Hall (2014), Observations of pronounced Greenland ice sheet firn warming and implications for runoff production, *Geophys. Res. Lett.*, *41*(12), 2014GL059806, doi:10.1002/2014GL059806.

Raymond, C. F., and K. Tusima (1979), Grain coarsening of water-saturated snow, *Journal of Glaciology*, *22*, 83–105.

Rennermalm, A. K. et al. (2013), Understanding Greenland ice sheet hydrology using an integrated multi-scale approach, *Environ. Res. Lett.*, *8*(1), 015017, doi:10.1088/1748-9326/8/1/015017.

Rignot, E., and J. Mouginot (2012), Ice flow in Greenland for the International Polar Year 2008–2009, *Geophys. Res. Lett.*, *39*(11), L11501, doi:10.1029/2012GL051634.

Rignot, E., I. Velicogna, M. R. van den Broeke, A. Monaghan, and J. Lenaerts (2011), Acceleration of the contribution of the Greenland and Antarctic ice sheets to sea level rise, *Geophys. Res. Lett.*, *38*(5), L05503, doi:10.1029/2011GL046583.

Rodriguez-Morales, F. et al. (2013), Advanced Multifrequency Radar Instrumentation for Polar Research, *IEEE Transactions on Geoscience and Remote Sensing*, doi:10.1109/TGRS.2013.2266415.

Schneider, T. (1999), Water movement in the firn of Storglaciaren, Sweden, *Journal of Glaciology*, *45*(150), 286–294.

Schneider, T., and P. Jansson (2004), Internal accumulation in firn and its significance for the mass balance of Storglaciären, Sweden, *Journal of Glaciology*, *50*(168), 25–34, doi:10.3189/172756504781830277.

Shepherd, A. et al. (2012), A reconciled estimate of ice-sheet mass balance, *Science*, *338*(6111), 1183–1189, doi:10.1126/science.1228102.

Smith, B. M., and Evans, S (1972), Radio echo sounding: Absorption and scattering by water inclusion and ice lenses, *Journal of Glaciology*, *11*, 133–146.

Sørensen, L. S., S. B. Simonsen, K. Nielsen, P. Lucas-Picher, G. Spada, G. Adalgeirsdottir, R. Forsberg, and C. S. Hvidberg (2011), Mass balance of the Greenland ice sheet (2003–2008) from ICESat data – the impact of interpolation, sampling and firn density, *The Cryosphere*, *5*(1), 173–186, doi:10.5194/tc-5-173-2011.

Tedesco, M., X. Fettweis, M. R. van den Broeke, R. S. W. van de Wal, C. J. P. P. Smeets, W. J. van de Berg, M. C. Serreze, and J. E. Box (2011), Record summer melt in Greenland in 2010, *Eos, Transactions American Geophysical Union*, *92*(15), 126–126, doi:10.1029/2011EO150002.

Tedesco, M., X. Fettweis, T. Mote, J. Wahr, P. Alexander, J. E. Box, and B. Wouters (2013), Evidence and analysis of 2012 Greenland records from spaceborne observations, a regional climate model and reanalysis data, *The Cryosphere*, *7*(2), 615–630, doi:10.5194/tc-7-615-2013.

Van der Veen, C. J. (2007), Fracture propagation as means of rapidly transferring surface meltwater to the base of glaciers, *Geophys. Res. Lett.*, *34*(1), L01501, doi:10.1029/2006GL028385.

CHAPTER 4

SNOW-ACCUMULATION SPATIAL VARIABILITY DETECTED FROM 2-18 GHZ RADARS ACROSS THE WESTERN ICE DIVIDE, CENTRAL WEST ANTARCTICA

4.1. Abstract

Spatial variability in accumulation is found using 2-18 GHz ground and airborne radars for the Central West Antarctic Ice sheet. From the ice divide, toward the Amundsen Sea, we find an increase of the accumulation rate of ~75% (+ 0.20 m w.eq. y^{-1}) for a 70-km transect by following internal annual reflection layers in the radar profile. These annual layers are not preserved on the Ross Sea side, where lower accumulation rates are found (< ~0.25 m w.eq. y^{-1}), and only the main reflection layers can be traced in order to calculate multiyear averaged accumulation rates. At the ice divide, we find a good agreement between the depth-age scales obtained by the radar and the firn cores. On the Amundsen Sea side, where higher accumulation rates are found, the radar-derived accumulation rates are higher than the firn-core accumulation rates. This mismatch may be caused by a noisy seasonal cycle in the isotopes and solutes challenging the establishment of a depth-age scale. Direct comparisons between the water stable isotope depth profile and the radar-averaged waveform could help identify the causes of this mismatch and eventually obtain a reconciled depth-age scale. Also, part of the mismatch

between the two depth-age scales can come from the small-scale spatial variability in the vicinity of the core site (within a radius of 1.5 km). We find up to 1.3 m of vertical variation for a continuous layer located at 25-m depth, across the entire radar grid around the site. I find that the average variation in accumulation rate in this area is 0.1 m w.eq. y-1 in the upper 25-m of the firn column, which is 20% of the average accumulation rate; this is not taken into account by a single-point measurement. Additional data will be processed to confirm the accumulation spatial trend and further investigate the accumulation variability on the Ross Sea side of the divide. The radar-derived snow accumulation rates will be available for comparison with regional atmospheric model outputs.

4.2. Introduction

The West Antarctic Ice Sheet (WAIS) represents the marine-based part of the Antarctic Ice Sheet. Grounded below sea level, WAIS has the potential to collapse making it a crucial place to study past behavior and future response (e.g., Joughin and Alley, 2011). WAIS is bounded by outlet glaciers with floating tongues (e.g., Pine Island Glacier, Thwaites Glacier) and wider ice shelves (Ross, Ronne, Filchner) that respond to oceanic forcing and to melting at their base (e.g., Jacobs et al., 2011). The ocean temperatures have been warming for the last three decades (e.g., Schmidtko et al., 2014). For the Amundsen Sea coast, west of the ice divide, the main outlet glaciers are thinning, retreating, and accelerating, actively contributing to sea level rise (Pritchard et al., 2009; Rignot et al., 2014). It has been highlighted that a possible WAIS collapse may have already begun (Joughin et al., 2014; Rignot et al., 2014). As a whole, WAIS ice loss is

estimated at 65±26 Gt yr^{-1} over the 1992-2011 period (Shepherd et al., 2012). To complete the mass balance of WAIS, the main mass input, snow accumulation, needs to be measured and monitored.

The quantity of snow that accumulated over the last decades is recorded in the firn, the layer of porous snow that survives one mass-balance year, ranging from the surface to the firn-ice transition at depth (Cogley et al., 2011). Air temperature as an effect on snow accumulation and warmer air would lead to greater snowfalls over Antarctica (e.g., Gregory and Huybrechts, 2006). Since 1958, when the first temperature observations became available, Central WAIS has experienced an increase of air temperatures that is most significant during the austral winter and spring (Steig et al., 2009; Bromwich et al., 2013), consistent with borehole temperature observations (Orsi et al., 2012; Steig and Orsi, 2013). In addition, Bromwich et al. (2013) observe a significant air temperature increase in the austral summer, which could lead to surface melt in the future. This observed recent temperature warming trend would suggest synchronous increase of the snow accumulation. However, this expected accumulation trend has not been yet confirmed from firn cores in central WAIS (Frezzotti et al., 2013), radar data (Medley et al., 2013), or climate re-analysis and regional climate models (Monaghan et al., 2006; Lenaerts et al., 2012). Unexpectedly, Burgener et al. (2013) observe a significant decrease of accumulation since 1975 based on 5 shallow firn cores located on both sides of the WAIS ice divide. Reasons for the difficulties in obtaining a robust trend, if any, are numerous and the primary ones are: (1) the short time span observed (only 4-5 decades), (2) the significant interannual and decadal variability in the signal, and (3) the spatial-scale used. Spatial heterogeneities and undulated surface topography will have

repercussions on the accumulation patterns when measurements with different spatial scales are used: firn cores, stake farms, radar profiles, 10-40 km simulation grid sizes.

The variability of atmospheric patterns originating from the air temperature changes over WAIS, leading to accumulation variations, are still the subject of debate, but its tropical origin is commonly accepted (e.g., Bromwich et al., 2013). For a longer time range, spanning the last 2,000 years, WAIS air temperature changes could find its source in the Pacific tropics with a strong decadal variability (Ding et al., 2011; Steig et al., 2013). In addition, the Southern Annular Mode (SAM) brings cooler temperatures in West Antarctica, but its effect is restricted to the autumn (Nicolas and Bromwich, 2014). The combination of SAM and the tropical El Nino Southern Oscillation (ENSO) makes the climate predictions (storm track and intensity) difficult. The main snow transport and deposition is dominated by warm and moist storms originating from the Amundsen-Bellingshausen Sea Embayment, moving toward the WAIS higher-elevation interior depositing snow (Genthon et al., 2005; Steig and Orsi, 2013).

In addition to the climate variability, the scale of the observations and simulations has an impact on the interpretations of the measurements in a larger or smaller context. While individual firn and ice cores suffer from a lack of representativeness of larger scales, numerical simulation grids are too large to fully capture local-scale processes due to the topography. To partly overcome these challenges and bridge the information gap between individual firn cores, ground and airborne radars have been used. Radars image continuous internal reflection layers caused by density contrasts in the layered polar firn with a high sampling rate and a decimeter scale vertical resolution (e.g., Eisen et al., 2008). These continuous reflection layers are assumed to be of a same age, referred to as

isochrones, and have been successfully used in WAIS to derive past accumulation rates (e.g., Nereson et al., 2000; Spikes et al., 2004; Medley et al., 2013). Having a firn-core depth-age scale at each end of the radar profile allows the dating of individual layers and confirms that the layers as isochronous (e.g., Spikes et al., 2004). Topography and wind-redistribution of snow, which influence the accumulation rates, are captured by these radar systems and facilitate firn-core interpretations to a larger area (e.g., Spikes et al., 2004; King et al., 2004).

To complement the five firn cores collected during the 2010 Satellite Era Accumulation Traverse (SEAT) and interpreted by Burgener et al., (2013), we collected in conjunction a total of 330 km of high-vertical-resolution radar profiles between the firn cores. Two high-frequency radars, operating from the ground and from an airborne platform, were used in this study (Panzer et al., 2013; Rodriguez-Morales et al., 2013). Using these surface-based radars in conjunction with shallow firn cores, we characterize the spatial patterns of the annual accumulation rates across the WAIS modern ice-sheet divide. We confirm that annual stratigraphy is preserved on the Amundsen Sea side of WAIS as previously observed from the airborne Snow Radar (2-8 GHz) (Medley et al., 2013). In contrast, we find that the Ross Sea side, with lower accumulation rates, does not preserve an annual stratigraphy in the radar profile. We present the agreement at the different core sites between firn-core depth-age scale and radar-derived depth-age scale. Finally, we present the small-scale variability of accumulation from the radar-derived accumulation rates in the vicinity of a core site and discuss the uncertainties associated when characterizing larger-scale accumulation patterns from firn-core data.

4.3. Satellite Era Accumulation Traverses

The SEAT project consisted of two consecutive Antarctic field seasons, collecting shallow firn cores (< 20 m) and high-frequency radar profiles (2-18 GHz) in order to retrieve recent snow accumulation rates spanning the satellite-era measurements (1975-present) in Central WAIS. The data were collected during snowmobile traverses. The first traverse took place in December 2010 and started at the WAIS divide deep-core site (79.47°S, 112.07°W, 1766 m) and traveled toward the Amundsen Sea, crossing the Ross-Amundsen ice divide, toward higher accumulation rates (Figure 4.1). The in-and-out bound traverse lines were 25 km apart to obtain further spatial variability. A total of 5 firn cores were extracted (Burgener et al., 2013), combined with 350 km of radar data collected over an elevation range of 1650-1800 m. In December 2011, the second traverse started at Byrd surface camp (80.01°S, 119.57°W, 1530 m), 160 km away from WAIS divide camp, also heading toward the Amundsen Sea, for a total of 470 km and collected 8 firn cores.

Previous studies reported modern-averaged snow-accumulation rates range between 0.20 m w.e. yr^{-1} at WAIS divide camp and > 0.25 m w.e. yr^{-1} on the Amundsen-Sea side of the Western divide (Burgener et al., 2013; WAIS Divide Project Members, 2013). The ice thickness at the WAIS divide core site is 3,455 m to bedrock (WAIS Divide Project Members, 2013). For the surface velocities, the Western divide is migrating toward the Ross Sea at a rate of 10 m yr^{-1} due to dynamical thinning on the Amundsen Sea side (Conway and Rasmussen, 2009). The primary source of snow accumulation is associated with storms coming from the Amundsen and Bellingshausen Seas. With a gentle surface slope, low pressure systems may penetrate far inland on the

West side of the ice divide (Steig and Orsi, 2013). Near the ice divide and on the Ross drainage side, accumulation is linked to a mid-latitude mechanism (Kaspari et al., 2004). Air temperature average for the WAIS divide camp is -30°C and temperatures are ranging between -24 and -30°C since 1979 at Byrd station (WAIS Divide Project Members, 2013; Bromwich et al., 2013).

4.4. Data

4.4.1. Ground radars and GPS

The near-surface radars used during the SEAT traverses were developed by the Center for Remote Sensing of the Ice Sheets (CReSIS), University of Kansas. The two Ultra-high-frequency (UHF) frequency-modulated continuous wave (FMCW) radars (Panzer et al., 2013) were operated simultaneously during the two SEAT traverses. The Ku-band radar operates over the frequency range of 12.5 to 17.5 GHz, while the Snow Radar operates at slightly lower frequencies between 2 and 8 GHz (Gomez-Garcia et al., 2012; Panzer et al., 2013; Rodriguez-Morales et al., 2013). Since both radars operate next to each other, a 2-8 GHz band-pass filter is applied to Snow Radar to reduce the signal interference with Ku-band radar (Panzer et al., 2013). Both radars can be used to retrieve continuous internal layers from the snow surface down to 25-30 meters into the dry firn to match the targeted depth for the firn-core collection. For this preliminary study along the SEAT-10 traverse, we will only use the surface-based Ku-band radar since it provided the best radar profiles revealing clearer subsurface features compared to the Snow Radar.

The vertical resolution of both radars is about 5 cm in snow for an average density of 300 kg m^{-3}. A density variation of 100 kg m^{-3} would lead to a ~5% change in the velocity propagation, resulting in a 20-mm difference in the vertical resolution (Panzer et al., 2013). This high vertical resolution allows us to pick reflection layers with an annual resolution in the radar profile. For the horizontal dimension, postprocessing stacking was applied to increase signal-noise ratio by averaging 10 traces, which resulted in an averaged radar trace spacing of 2.5 m. The two radars were installed on a wooden platform, part of an aluminum triangular sled. The transmitting and receiving antennas were located ~2 m above the snow surface. To avoid interferences between the electromagnetic signal and the sled, microwave absorbent material was added around the metal parts and the sled design was not detected in the radar return. The sled is pulled by a snowmobile travelling on the snow surface at a speed averaging 10 km h^{-1}.

Simultaneously with the radar data collection, we used a Trimble R7 rover GPS, mounted on top of the sled (2.5 m above the surface), in a kinematic mode for accurate positioning and to obtain a surface elevation profile. Positions were recorded at a 5 seconds interval rate, corresponding to a sampling interval of ~15 m. GPS data were post-processed using a precise point positioning approach. The Canadian Spatial Reference Service (CSRS) online program was chosen because it uses precise global navigation satellite system orbit ephemerides and clock information together with precise undifferenced carrier-phase observations to improve the accuracy of the collected GPS data points (Mireault et al., 2008). The uncertainties are related within one standard deviation of each transect and averaged here for the two field seasons: latitude and

longitude: 5 cm and elevation: 10 cm. GPS was synchronized to the surface-based radar by assigning to each radar trace a linearly interpolated position and elevation.

4.4.2. Airborne radar

In addition to the surface-based radar data, airborne radar data were collected on 9 November 2011, as part of the NASA's Operation IceBridge (OIB) campaign. The airplane flew over the SEAT10-4 to SEAT10-6 transect about one year after the SEAT10 ground traverse (Figure 4.1). The radar data were collected by the airborne version of the Snow Radar developed by CReSIS, operating at a center frequency of 5 GHz with a bandwidth up to 6 GHz (Leuschen et al., 2011). The ultra-wideband radar enables imaging the polar firn internal layers with a 5 cm vertical resolution, similar to the ground-based system (Rodriguez-Morales et al., 2013). In the along-track dimension, the data product spacing is 1.12 m for a platform velocity of 140 m s^{-1}, but the actual resolution is approximately of 16.7 m for an aircraft at 500 m above surface (Leuschen et al., 2011). The snow surface was identified and picked in the radar data using an amplitude threshold at the base of the surface return.

4.4.3. Firn cores

Oxygen isotopes changes in Antarctic precipitation reflect changes in atmospheric circulation even better than temperature or other variables (Steig et al., 2013). We derive depth-age scales for each firn core using the seasonal variations of δ18O and δD. Two volcanic horizons (Pinatubo and El Chichon) often identifiable in the firn cores offer an independent confirmation of the accuracy of the water-isotope depth-age scale. We refer

the reader to Burgener et al. (2013) for a complete description of the methods used to obtain depth-age scales and density profile for each firn core collected during the SEAT-10 traverse. The depth-age scale temporal accuracy is less than ±1 year for the 1981-2010 period, and about ±1 year prior to 1981 for every firn-core site except SEAT10-4 (Burgener et al., 2013). For this last firn core, the dating was more challenging, resulting in an uncertainty much greater than one year; therefore, this firn core is taken with caution in our analysis. The density sampling was done with a 2-cm vertical spacing for both a 2-m snow pit and from the firn core. Every sample was measured and weighed, 5 and 10% total errors were estimated for the firn core and snow pit, respectively. Table 4.1 illustrates the main characteristics of the firn cores collected during the SEAT-10 traverse.

4.5. Methods

4.5.1. Layer picking and time to depth conversion

To accelerate and simplify the manual picking of the internal layers detected by the radars, a semi-automatic layer picker was developed by A. Ivanov and L. Koenig at NASA Goddard. This picker is based on the difference between the upper frequencies and the lower frequencies in a radar image to accentuate the peaks within a radar trace. Continuous layers are created by connecting the peaks between two traces with respect to depth. After running the automatic picker, a manual step is required to re-organize the data, to connect discontinuous layers and to index each layer. We estimate the picking uncertainty at ± 3 vertical samples. With a sample size of 4 cm, we obtain a vertical uncertainty of 12 cm.

The depths of the internal layers are estimated from the two-way-travel time (TWT) of the radar electromagnetic wave between the snow surface and each continuous layer. For nonmagnetic and low-loss dielectric mediums like snow and firn, the velocity (v) of an electromagnetic wave can be approximated as the ratio of the velocity in a vacuum (c ~0.3 m ns^{-1}) to the square root of the permittivity (real part of the dielectric constant: ε') of the medium (Equation (1)).

$$v = c/\sqrt{\varepsilon'} \qquad (1)$$

A first-order depth estimate is obtained using a constant dielectric value throughout a firn corresponding to a value of ε' = 2.2 and the associated electromagnetic velocity is 0.20 m ns^{-1}. To refine this depth estimate, ε' needs to increase at depth as the density increases. We compare two relationships to calculate ε' as a function of the density (ρ) of snow and ice and the permittivity of ice (Kovacs et al., 1995 for Equation (2) and Looyenga 1965 for Equation (3)).

$$\varepsilon' = (1 + 0.845\rho_{snow}(z))^2 \quad (2)$$

$$\varepsilon' = \left(\frac{\rho_{snow(z)}}{\rho_{ice}} * \left(\varepsilon'^{\frac{1}{3}}_{ice} - 1\right) + 1\right)^3 \quad (3)$$

For Equation (3) we use ρ_{ice} of 917 kg m^{-3} and ε'_{ice} of 3.15. For the density profile used to convert the radar TWT to depth, we compile the density profiles for each firn core during SEAT-10 into a single profile (Figure 4.2). By using a composite density profile, we attempt to minimize the impact of small-scale spatial density heterogeneities in the layered polar firn. In addition, to smooth the significant variations of the density profile measured at a 2-cm resolution, due for example to the presence of low-density hoar layers, we use a bi-exponential relationship to fit the data (Figure 4.2). When using a similar density profile, the differences between Equations (2) and (3) do not exceed 2.5

ns for the upper 20 m of the firn, representing 24 cm in the vertical. For the first 20 m of the firn, we obtain up to 3 ns of TWT differences when subtracting a constant propagation velocity model (0.20 m s^{-1}) with the mixture model from Looyenga, (1965) (Figure 4.2).

4.5.2. Radar-derived accumulation uncertainties

The uncertainty estimation when deriving accumulation rates from internal radar layers comes from the layer age, the density profile, and the layer picking. In this study, the layers revealed by Snow Radar on the Amundsen Sea side (Figure 4.1) are assumed to be annually spaced (Medley et al., 2013). From the surface, which corresponded to December 2010 and November 2011, for the ground radar and the airborne radar, respectively, we count the years down as we encounter new layers. For both ground and airborne radars, we assign to the first subsurface layer the age of 1 January 2010 (or 2011 for the airborne) and count every subjacent layer from there. We did not linearly interpolate the accumulation to obtain a monthly resolution, since the assumption of a constant accumulation throughout the year might not be valid (Bromwich et al., 2004). If an internal layer is weaker within the radar profile and is not being identified and traced over the entire profile, the accumulation rate would double where this layer is missing. In contrast, a sub-annual layer could form at another time within the year and the picking this sub-annual layer would lead to an underestimation of the accumulation rate for this year. Figure 4.3 illustrates the presence of the annual layer dominants in the vicinity of SEAT10-4 where higher accumulation rates are found. At SEAT10-5, the lack of annual stratification is observed where snow accumulation rates are smaller. For both radars, the

annual layers become difficult to identify below a depth of 10 m, leading to an increase of the age uncertainty. In addition, by assuming a steady-state spatially-invariant density profile over the entire radar profile, we do not take into account spatial heterogeneities of the density that would have an effect when converting TWT to depth and to calculate water-equivalent accumulation rates. Finally, an error of 3 vertical samples (~12 cm) is introduced when picking each individual layer, which would result in a 0.048 m w.eq y^{-1} error in the accumulation rate estimates.

4.6. Results

4.6.1. Internal stratification variability across the ice divide

During SEAT10, the modern ice-sheet divide was crossed twice, between site SEAT10-1 and SEAT10-3 and between SEAT10-4 and SEAT10-6 (Figure 4.1). We choose the transect from SEAT10-4 to SEAT10-6 to explore the spatial patterns of accumulation across the ice divide. This transect is preferred because one firn core (SEAT10-5) is located at the divide and the two other cores are located ~70 km away from the ice divide on each side (Figure 4.1). Using the Ku-band radar operating on the surface, we deduce an increasing spatial trend of accumulation from SEAT10-6 to SEAT10-4, assuming the layers to be isochrones (Figure 4.4). The internal layers revealed by the Ku-band radar are likely annual in the vicinity of SEAT10-4 (Figure 4.3) and most of the way toward the ice divide (Figure 4.4), as confirmed by a previous study over Thwaites Glacier catchment (Medley et al., 2013). However, the transect between SEAT10-5 and SEAT10-6 on the Ross Sea side only shows multi-annual layers. We assumed that the smaller spacing between individual layers in a lower accumulation

regime and surface processes such as wind scouring, drifting, and redistribution, preventing the radar data from solving for annual accumulation rates (Figure 4.4). However, a few isochronal layers, continuous from SEAT10-5 to SEAT10-6, allow the calculation of accumulation rates, averaged over multiyear time periods. For the surface topography, over a similar 70-km transect length, the slope is greater toward the Amundsen Sea, compared to the slope toward the Ross Sea. The surface undulations are also more pronounced on the Amundsen Sea Side (Figure 4.4, left), resulting in a greater topographic expression of the bed and shallower ice (Morse et al., 2002). This undulated topography on the Amundsen Sea side could affect the snow accumulation rates locally.

4.6.2. Spatial patterns of accumulation

Based on the radar profiles of Figure 4.4, internal layers are picked on either side of the ice divide (Figure 4.5, top panels). Whereas layers with an annual resolution are identified on the Amundsen-Sea-side profile, only four layers are picked on the Ross-Sea-side profile, dated using the internal layer ages at SEAT10-5, assuming continuous layers to be isochronous. A few layers, identified as annual near the SEAT10-4 firn core, disappeared toward the ice divide as the snow accumulation decreases (blue layers on Figure 4.5). These layers were not included when deriving accumulation rates.

On the Amundsen Sea side, we found that the averaged accumulation rates derived from the Ku-band radar increase by ~75% (+0.20 m w.eq. y^{-1}) over a 70-km transect, from SEAT10-5 to SEAT10-4 (Figure 4.5). A similar increasing trend of the averaged accumulation rates was not confirmed using the stable-isotope dating for SEAT10-4 and SEAT10-5 (Table 4.1). Indeed, the radar-derived averaged accumulation

rates for the SEAT10-4 location are significantly higher (+0.22 m w.eq. y^{-1}) than the firn-core accumulation rates even within the ±1 σ of interannual variability range (Figure 4.4, left panel and Table 4.1). However, this is likely due to the difficulties in dating the SEAT10-4 firn-core, resulting in uncertainties much greater than one year, as reported by Burgener et al. (2013). At the divide (SEAT10-5), radar and firn-core accumulation rates are in agreement. On the Ross Sea side, only a few layers were picked, resulting in multi-annual averaged accumulation rates. On this side, the accumulation rates are decreasing while going away from the divide for both firn cores and radar data. At SEAT10-6, the radar-derived accumulation rates are slightly lower than the firn core but stay within ±1 σ of variability. A similar decreasing trend of accumulation from the Amundsen Sea toward the ice divide and beyond was reported by Morse et al. (2002) (Figure 4.5). In their study, one layer was dated at 2.5 ky in the Byrd ice core and this horizon was followed in the radar data, producing a long-term averaged accumulation rate. Medley et al. (2013) reported similar accumulation rates on the Amundsen Sea side of the divide but this airborne-radar study did not investigate accumulation pattern on the Ross sea side. It will be interesting to see if this ~140-km accumulation spatial pattern is also detected by the regional climate models that simulate accumulation at a larger grid size (~25 km).

4.6.3. Temporal variations

We compare the depth of individual years using depth-age scales obtained in three different ways: oxygen-isotope dating on firn cores, Ku-band radar layers, and OIB Snow Radar layers for the last 30 years, at four different sites (Figure 4.6). For SEAT10-3 and -4, given years are found at greater depths in the radar dating compared to the firn-core

dating. At SEAT10-4, the airborne-radar depth-age scale diverges from the ground-radar depth-age scale at 10 m; this is due to the presence of a few continuous weaker layers in the ground-radar profile that were not found in the airborne radar profile. At the ice divide (SEAT10-5), the three depth-age scales agree; the airborne depth-age scale is shorter since annual layers were not continuously observed below 7-m depth (Figure 4.3 bottom-right panel). For SEAT10-6, only four internal radar layers are dated using the annual radar layers at SEAT10-5, and continuously traced until SEAT10-6 (Figure 4.6). For SEAT10-6, a good agreement is found with an average of 0.75 m for the depth differences between the radar and the firn cores. The older internal layers tend to be shallower for the radar compared to the firn cores.

The common time span studied here is about 30 years, which allows us to explore the interannual variations in accumulation to detect potential temporal trends. For each firn core extracted during SEAT10, a statistically significant decreasing trend of accumulation has been observed (Burgener et al., 2013). However, caution and advanced statistical analysis are required when validating an observed trend for such short time records (~30 years) (Rupper et al., 2015). Using the radar layers, such advanced statistical analysis to find the trend has not been done yet, and no simple statistical trend is evident. Using both radar and firn-core accumulation rates, we observe that the interannual variability ($\pm 1\sigma$) is in general greater for the high-accumulation sites compared to the low-accumulation sites. The standard deviation (σ) is three times higher for the SEAT10-4 compared to SEAT10-5 for both firn cores and radar-derived accumulations rates (Table 4.1). On Figure 4.7, we compare the interannual variability obtained for the radar-derived accumulation rates and for firn-core accumulation rates at

three different locations. The high-snow years observed in the firn-core data do not always match with the radar data for SEAT10-5 where averaged accumulation is similar. For the high-accumulation sites, the averaged accumulation rate is lower in the firn cores compared to the radar throughout the entire 30-year time period for SEAT10-5 but only for the last 15 years for SEAT10-4. Between 1982 and 1995, accumulation rates are found in the core with similar values compared to the radar (Figure 4.7). SEAT10-1 and SEAT10-6 sites were not presented here since their annual accumulation rates were not calculated using the radar data due to the lack of annual stratification. We note that when averaged-accumulation rates are less than ~0.25 m w.eq. y^{-1} based on the firn cores, the annual radar layers become difficult to follow continuously with both OIB Snow Radar and surface-base Ku-band radar.

4.6.4. Small-scale spatial variability

In the vicinity of each firn-core site, a 200-m by 200-m grid and a ~10-km bowtie-shaped transect were surveyed by the ground radar to explore the small-scale spatial variability of snow accumulation. We present on Figures 4.8 and 4.9 the results obtained at SEAT10-4, our highest accumulation site, where the internal reflection layers were traced. The top-left panel of Figure 4.8 illustrates the layout of the survey. The snow-surface conditions and surface roughness during the grid survey were similar to those observed a year later using the Digital Mapping System (DMS) onboard a NASA aircraft, with small sastrugis formed by wind erosion (top-right panel on Figure 4.8). The radar profile presents continuous internal reflection layers over the entire grid and bowtie pattern that we traced to look at the accumulation-rate variability for each radar trace.

The internal stratigraphy on the radar profile is represented by straight continuous layers that become slightly undulated at greater depth. The impact of these undulations can be quantified by looking at the difference between the depths of each isochrone layer over the entire profile. We found that the maximum depth variation for a layer of a given age increases at depth (Figure 4.9), consistent with the observed undulation patterns in the radar stratigraphy, which are more pronounced at greater depth (Figure 4.8). We find an averaged layer-depth variation of 0.65±0.35 m from the surface to 25-m depth with variations increasing with depth. The layer-depth variability is up to 1.3 m for the 1976 layer across the entire transect combining grid and bowtie-shaped pattern, less than 1.5 km away from the firn-core site. The observed layer differences in depth across the grid will have an impact when deriving accumulation rates. We find an averaged accumulation-rate variability of 0.1 m w.eq. y^{-1}, which is 20% of the averaged accumulation for the firn-core site (Figure 4.9, middle panel). It is important to note that we use the same steady-state spatially invariant density profile to convert the radar TWT to depth so spatial density variations, which are expected to be small, are not accounted for.

4.7. Discussion

Large- and small-scale spatial accumulation variability is observed across the Central WAIS ice divide in the surface-based radar data. The spatial increase (+75%) of the accumulation rates from the divide toward the Amundsen Sea side (to SEAT10-4), spanning 70 km, is not being captured by the firn cores due to the noisier seasonal stable isotope signal for this firn core (Burgener et al., 2013). The radar-derived accumulation

rates are in agreement with the previously radar-derived long-term accumulation trend (Morse et al., 2002), and the radar-derived accumulation map for Thwaites Glacier catchment (Medley et al., 2013). For the firn-core dating, the water stable isotope and solute method was difficult at the high-accumulation site, especially for the SEAT10-4 firn core (Burgener et al., 2013). At this site, the age confirmation using the well-dated Pinatubo and El Chichon volcanic markers did not occur. To explain the absence of volcanic markers at depth and the lower averaged-accumulation using the $\delta^{18}O$ isotopes for dating, we make the hypothesis that this core can contain a strong sub-annual isotopic signal, which could lead to an erroneous dating by following a sub-annual cycle instead of the annual cycle at shallow depths. If this hypothesis is valid, the volcanic markers would be found at greater depths for SEAT10-3 and SEAT10-4. On the Amundsen Sea side, the high-accumulation regime allows extraction of seasonal information from water stable isotopes (Küttel et al., 2012).

We also note the absence of annual radar reflectors for the Ross Sea side where lower accumulation rates are found. The Ku-band radar has vertical resolution of 5cm, which is about eight times greater than the spacing between two annual layers, for averaged snow accumulation rates of 0.2 m w.eq. y^{-1} and a snow density of 500 kg m^{-3}. Therefore, annual layers have the potential to be detected if density contrasts are large enough to generate a signal reflection at given interfaces. We think that different snow deposition, wind redistribution, and densification processes occurring on the Ross Sea side could lead to a different stratification in the firn and the absence of annual reflectors in the radar data. The surface depositional processes, including wind redistribution, are likely on similar scale as snow deposition by the different storms over a year. This

mechanism would not allow a good preservation of the stratigraphy like on the Amundsen Sea side. High-accumulation sites are expected to present larger density contrast with important layering on an annual basis, whereas low-accumulation sites would only have a small variability in density and a similar grain size range due to wind effect (Landais et al., 2006). However, a later study by Hörhold et al., (2011) observed that the density variability decreases with increasing mean-annual temperature and accumulation rates. A higher density variability at lower accumulation sites could produce a more complex snowpack, preventing the establishment of clear reflection layers. In addition of their density, layers are also created due to grain size and shape, hardness, and viscosity (Hörhold et al., 2011), which could impact the radar signal.

This work is still in progress and we have detailed snow-pit stratigraphy during the SEAT-11 fieldwork at 8 different sites across the ice divide to help understand the processes causing the layering in the radar data. We complemented the pit stratigraphy at each site with infrared images to better quantify the observed variation in the snow with depth. During SEAT-11, we also have detailed radar measurements with both the Ku-band Radar and the Snow Radar next to each snow pit and we used a metal plate at given depth to better calibrate the radar data with depth. In addition, we would like compare directly the water stable isotope depth profile with a stacked radar waveform to see if there are any correlations between the two signals and relate physical snow deposition and densification processes with the chemistry. Finally, during SEAT11, we have repeated firn cores at two locations on either side of the ice divide and we will analyze them independently to provide an additional check on the deduced depth-age scales using two different dating techniques.

4.8. Conclusions

Continuous high-frequency radar profiles across the West Antarctic ice sheet divide are able to retrieve accumulation rates for the last 30 years. From the ice divide toward the Amundsen Sea, we observe a 75% (+ 0.20 m w.eq. y^{-1}) increase of accumulation over a 70-km transect using radar-detected annual layers created by density contrasts in the upper part (> 25 m) of the firn. On the Ross Sea side of the divide, the annual layers are not detectable for accumulation rates less than ~0.25 m w.eq. y^{-1}. However, continuous isochronal layers do span the ice divide, allowing for retrieval of multiyear accumulation rates ranging between 0.15 and 0.2 m w.eq. y^{-1}. While comparing the firn-core depth-age scales obtained by stable-isotopes dating with the radar depth-age scale assuming the layers to be annual and isochrones, we find a good agreement at the low-accumulation sites but some discrepancies for the higher-accumulation sites likely due to the noisier isotope signal challenging the SEAT10-4 firn core dating (Burgener et al., 2013). While looking at the small-scale variability of accumulation with a 200 m by 200 m grid and a 10-km bowtie-shaped transect, we find an averaged layer-depth variation of 0.65±0.35 m for the first 25 m of the firn column with variability increasing with depth, consistent with the internal undulation patterns observed in the radar data. This variability leads to an averaged accumulation-rate variation of 0.1 m w.eq. y^{-1}, which is 20% of the mean accumulation rate. The depth difference for individual isochrone layer increases with depth across the entire grid and could result in larger differences past the depth limit of 20 m that was investigated in this study. This work will further benefit from a thorough analysis of the SEAT11 data, providing an additional 500 km of radar survey and seven shallow firn cores. The SEAT11 traverse started at Byrd

Station, located 160 km away from the ice divide on the Ross Sea side and allows the investigation of a longer transect in lower accumulation regions.

4.9. Acknowledgments

This work was supported by the US National Science Foundation Office of Polar Programs (OPP-0944653 to R.F and OPP-0944730 to S.R). C.M acknowledges the NASA ESS Fellowship program (NXX-11AL64H). Thanks to the 2010 and 2011 additional field team members: Mike Atkinson, Jessica Williams, and Randy Skinner. Thanks to CReSIS, for loan and help with Ku-band and Snow Radars that allowed us to collect high-quality data to make this study possible. Thanks to the Air National Guard, Kenn Borek Air Ltd, and UNAVCO. The radar layers and derived accumulation rates will be available for download as part of the SUMup initiative.

Table 4.1: SEAT-10 firn core locations and specifications. Mean annual accumulation rates are given with one standard deviation for both firn cores and radar, representing the range of the annual values, for a similar time span. Note that original firn-core time spans can be found in Burgener et al. (2013). For the firn cores SEAT10-1 and SEAT10-6, the radar profile internal stratigraphy was only multi-annual and an averaged-annual accumulation rate estimate was not calculated.

NAME	Latitude	Longitude	Elevation (m)	Length (m)	Mean accumulation (m w.eq. y^{-1}) Firn cores	Radar	Common time span (y)
SEAT10-1	79.38°S	111.24°W	1791	15.6	0.22 ± 0.05	- -	1974 - 2010
SEAT10-3	79.04°S	111.55°W	1772	16.7	0.19 ± 0.08	0.38 ± 0.10	1980 - 2010
SEAT10-4	78.49°S	111.70°W	1650	22.6	0.25 ± 0.13	0.47 ± 0.15	1976 - 2010
SEAT10-5	79.12°S	113.04°W	1794	16.5	0.24 ± 0.08	0.27 ± 0.06	1985 - 2010
SEAT10-6	79.75°S	114.55°W	1694	18.7	0.21 ± 0.07	- -	1966 - 2010

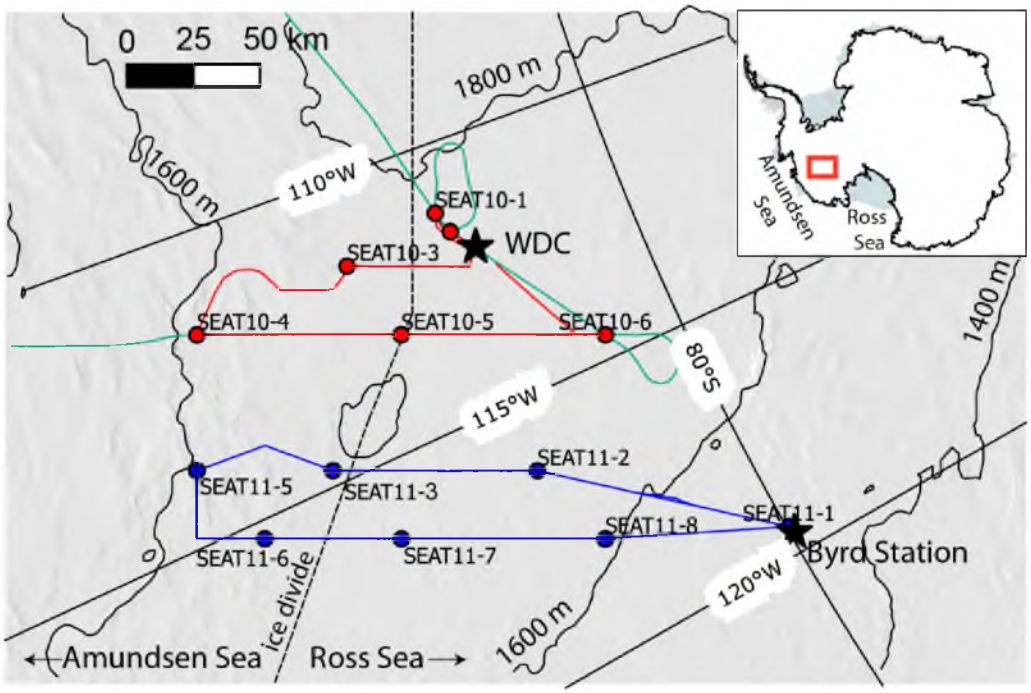

Figure 4.1: Study site in Central WAIS. SEAT-10 (red) and SEAT-11 (blue) represent 330 km and 500 km, respectively. Five firn cores were collected in 2010 and seven in 2011. The ice divide is represented by the dashed line. The starting points of SEAT were WAIS Divide Camp (WDC) in 2010 and Byrd Station in 2011 (black stars). On 9 November 2011, Operation IceBridge (green) flew over the SEAT10-4 to SEAT10-6 with Snow Radar on board. The elevation contour lines (in black) were obtained from high-resolution Radarsat Antarctic Mapping project (RAMP2) (Liu et al, 2001). The background image is a MODIS mosaic (Scambos et al., 2007). This figure was made with basemaps compiled in Qantarctica©.

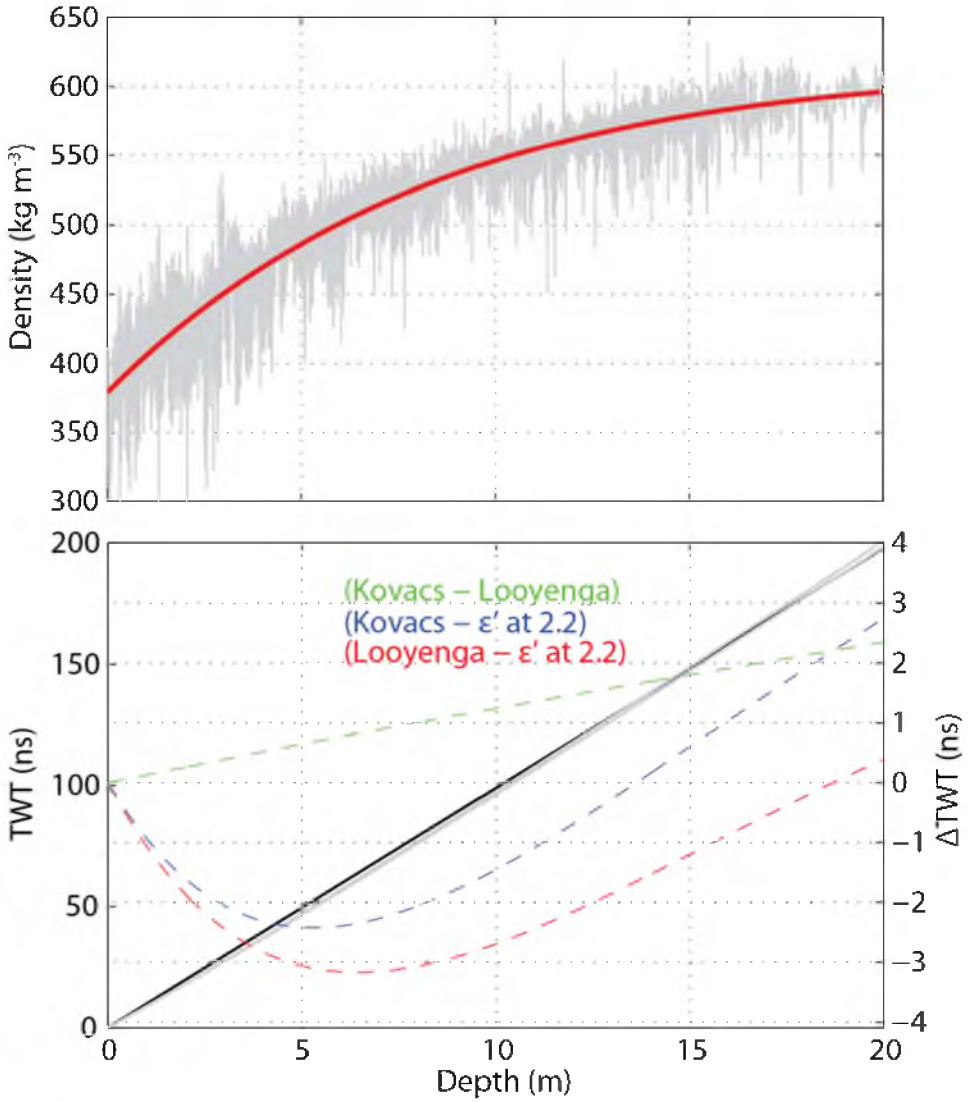

Figure 4.2: Top panel: in gray, raw density profiles for the five firn cores extracted during SEAT10 in Central WAIS (Figure 4.1) used for the TWT to depth conversion. We use a biexponential function to fit the density data (solid red). Bottom panel: Two-way-travel time as a function of depth calculated with three methods: two density adjusted methods (gray) or with a constant dielectric constant at depth (red). Solid lines are related to the left-y axis (TWT), whereas dashed lines are related to the right-y axis (ΔTWT). The differences between the three methods are illustrated with dash lines and remain with the ±3-ns range for the first 20-m depth.

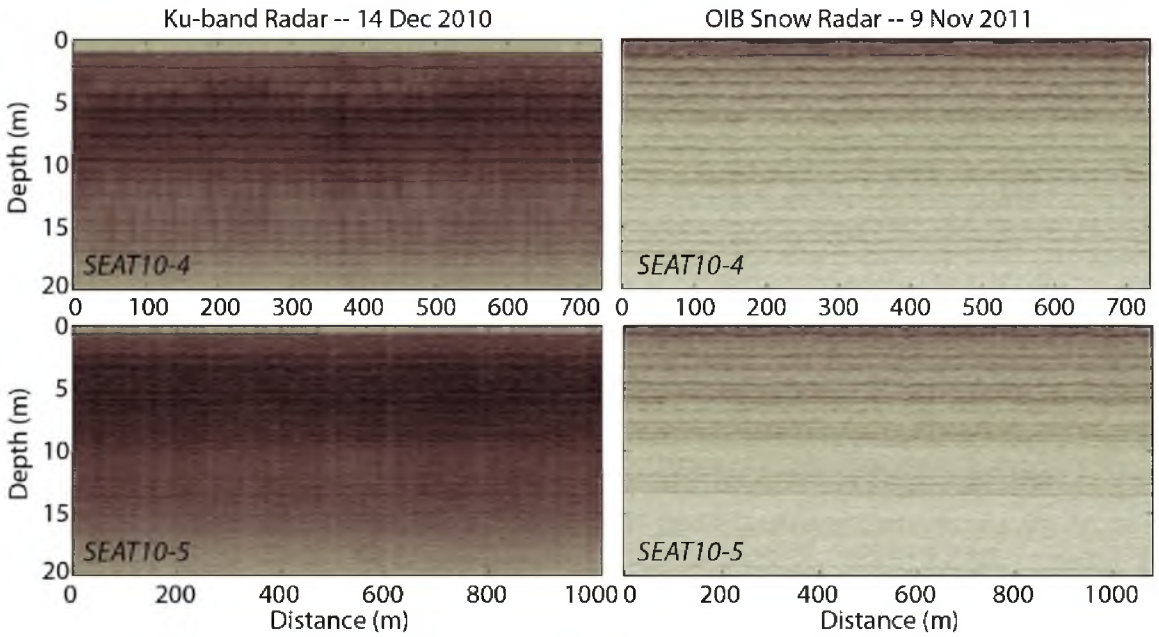

Figure 4.3: Comparison between the Ku-band radar operating from the surface at 15 GHz (left) and the airborne Snow Radar, 5 GHz (right) at two different locations, near SEAT10-4 (top) and SEAT10-5 (bottom). For the Ku-band radar profiles (left), the surface is lowered on purpose to account for the additional year of accumulation that happened between the two data collections to allow a better comparison of their stratigraphy. The maximum horizontal distance between two transects is 40m.

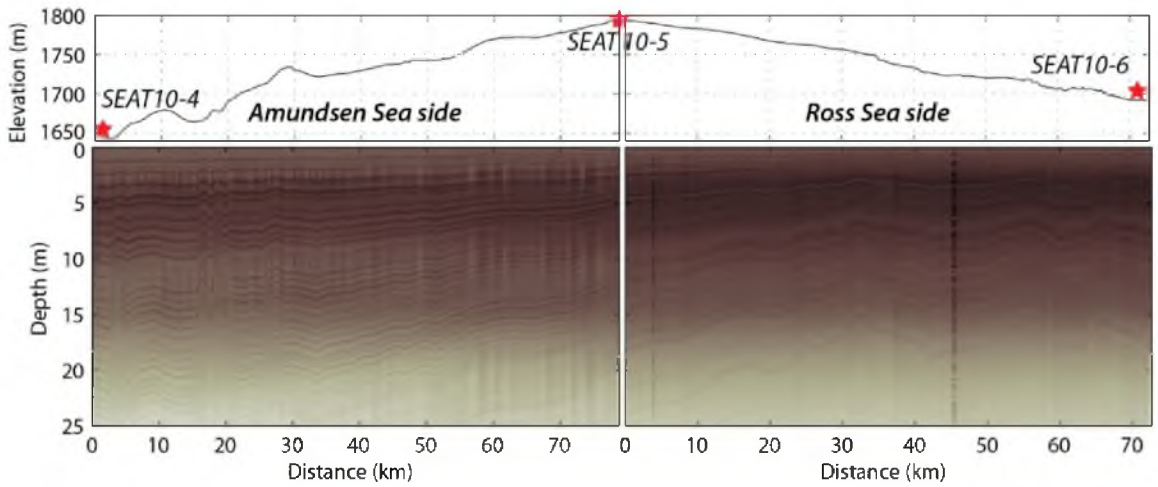

Figure 4.4: Evolution of the Ku-band radar profile while crossing the ice divide between the firn cores SEAT10-4 and SEAT10-6. On the Amundsen Sea side, an annual signal is preserved in the stratigraphy. In contrast, on the Ross Sea side, only the main reflection layers can be traced in the radar profile. An increasing spatial trend of accumulation from the divide toward the Amundsen Sea is visible based on the internal layering.

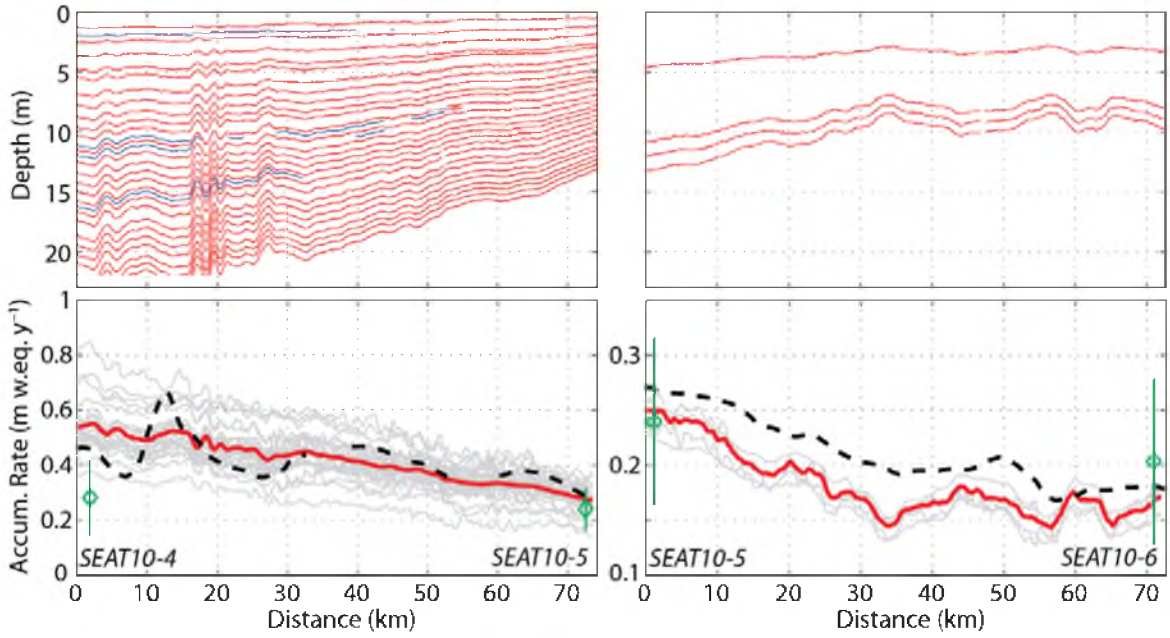

Figure 4.5: Based on the radar profiles on Figure 4.4, accumulation rates are obtained for the SEAT10-4 to SEAT10-6 transect. On the top left, annual layers are in red and the few blue layers represent discontinuous layers that were present at SEAT10-4 but could not be followed all the way toward SEAT10-5 (divide). For the bottom panels, accumulation rates for each radar trace between two distinct layers are in gray and the averaged accumulation rates are in red. We compare our radar-derived accumulation rates with the long-term-averaged radar-derived accumulation rates from Morse et al. (2002) (black dash). The green diamonds represent the averaged accumulation rate ±1 standard deviation for the firn cores, located on both ends of the profile. Note the different vertical scale used for the accumulation rates on each side of the ice divide.

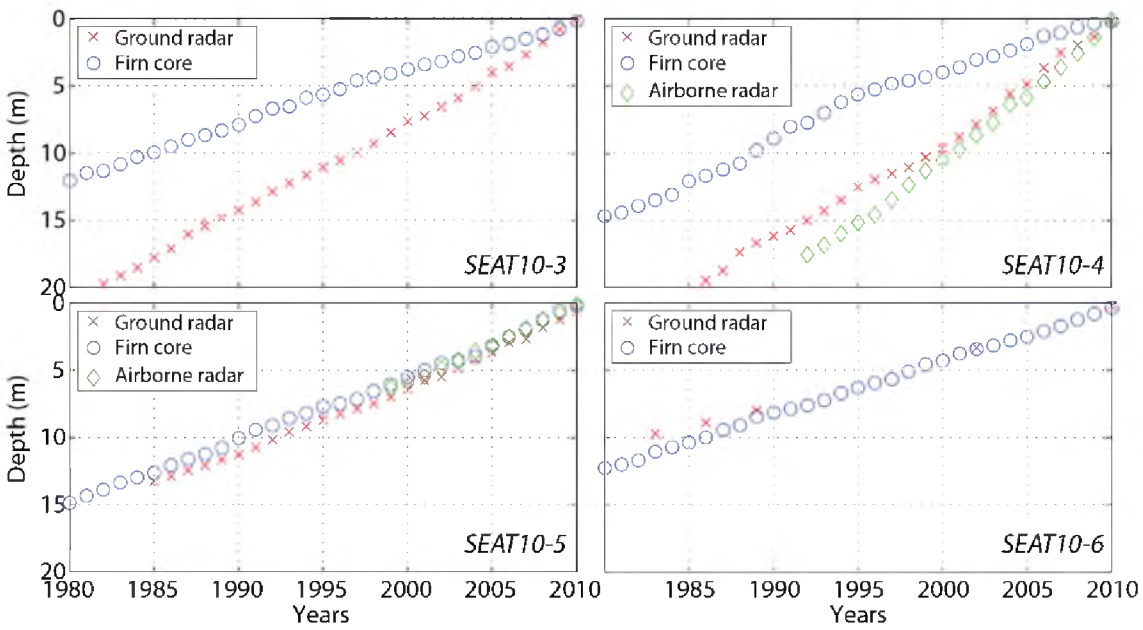

Figure 4.6: Comparison of the depth-age scales obtained using Ku-band radar (red crosses) and the firn core isotopes (blue circles). For SEAT10-4 and -5, OIB Snow Radar layers (green diamonds) were added. For SEAT10-6, only four dated layers were added. We find a good agreement between firn cores and radar for the low-accumulation sites but discrepancies are higher for the high-accumulation sites.

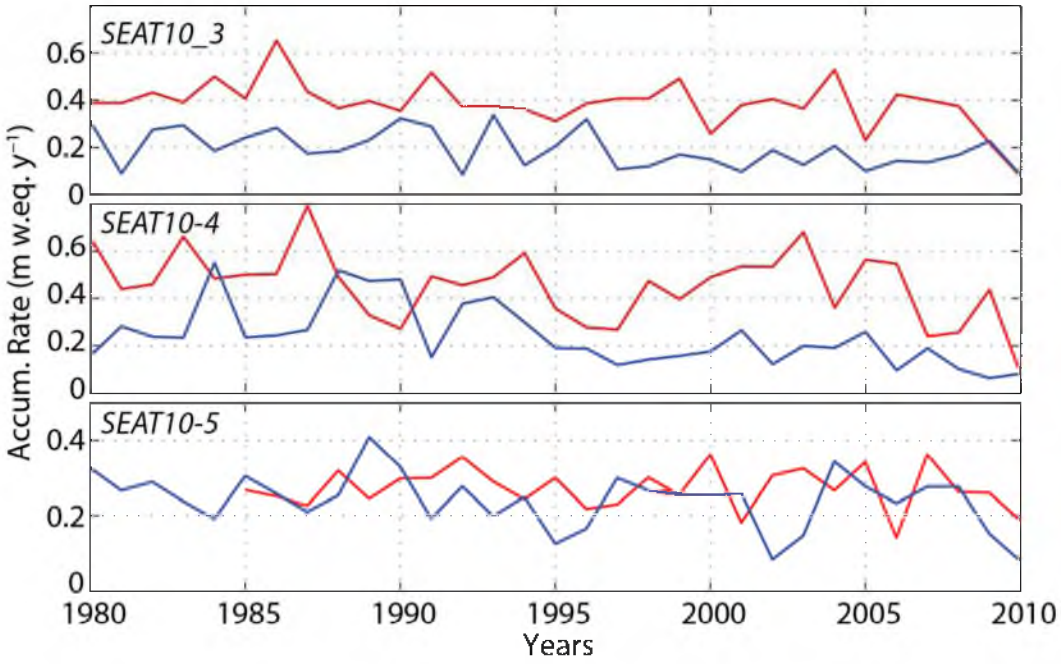

Figure 4.7: Interannual variability of the accumulation rates for the three firn-core sites of SEAT-10 where an annual depth-age scale was obtained from both firn core (blue) and radar (red). The radar-derived accumulation rates are higher than the firn-core accumulation rates for the Amundsen Sea side of the divide. Note the different y-axis scale for SEAT10-5.

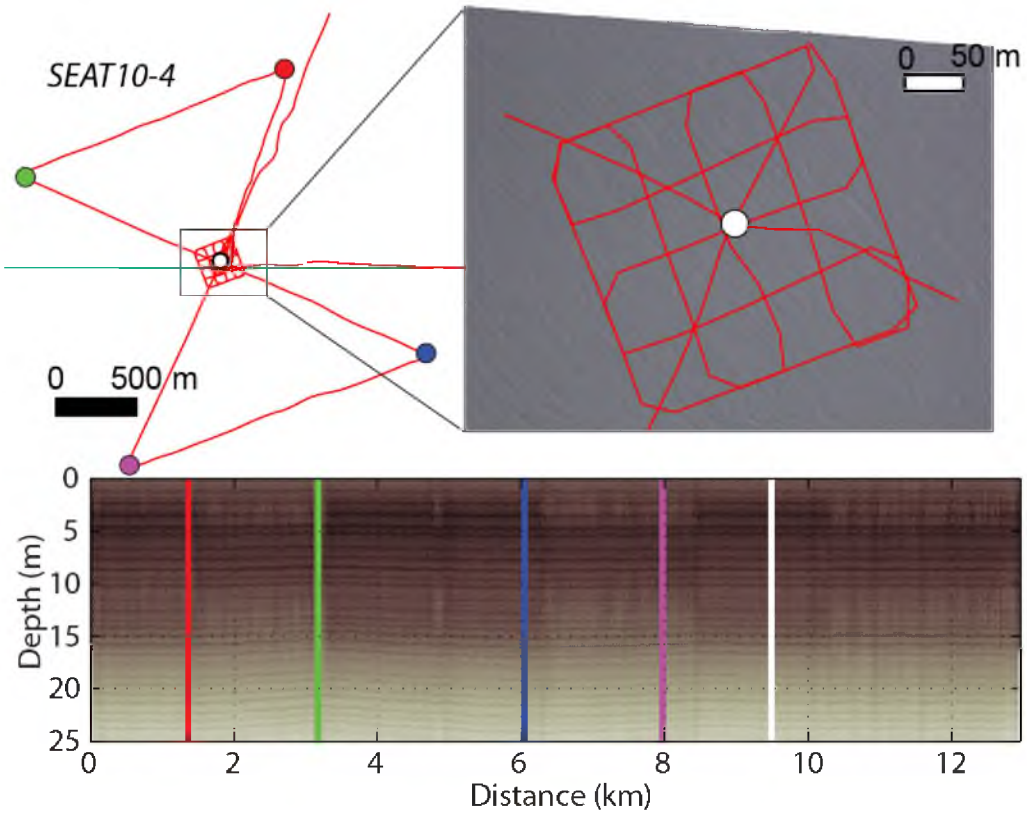

Figure 4.8: Small-scale accumulation variability investigated at SEAT10-4 (Figure 4.1) by a combination of a ~10 km bowtie pattern and a 200 m by 200 m grid. The colored circles located at end points of the bowtie are represented by vertical bars in the radar profile. On the top right-panel, a geo-located DMS image was obtained on 9 November 2011 during the OIB campaign, illustrating the typical surface roughness at the site (Dominguez, 2011).

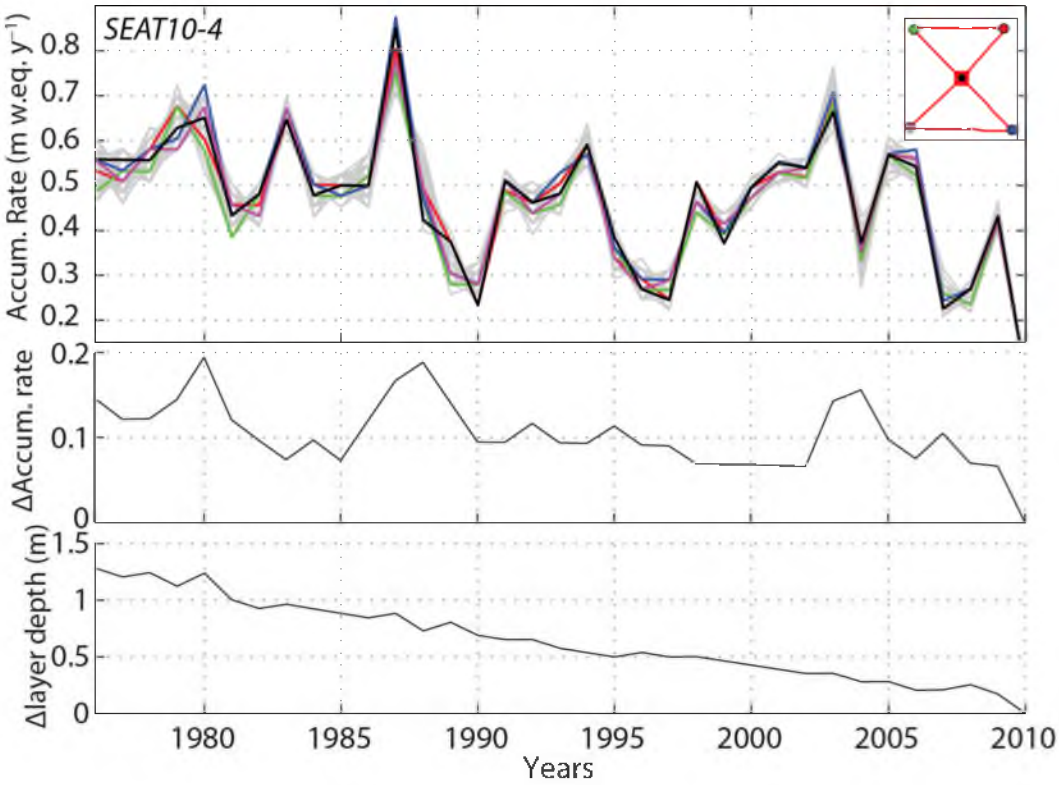

Figure 4.9: Accumulation-rate variability observed in the vicinity of the SEAT10-4 drill site on the Amundsen Sea side. On the top panel, the radar-derived depth-age scales are shown in different colors, matching the different corners of the bowtie pattern. Light gray depth-age scales represent the accumulation rates derived for all the other radar traces for the bowtie and the grid. On the middle panel, the maximum difference between the accumulation rates derived for each radar trace, is calculated for each year, across the entire grid. On the bottom panel, the maximum difference between the layer depths obtained for each radar trace is calculated also for each year.

4.10. References

Bromwich, D. H., Z. Guo, L. Bai, and Q. Chen (2004), Modeled Antarctic precipitation. Part I: Spatial and temporal variability, *J. Climate*, *17*(3), 427–447

Bromwich, D. H., J. P. Nicolas, A. J. Monaghan, M. A. Lazzara, L. M. Keller, G. A. Weidner, and A. B. Wilson (2013), Central West Antarctica among the most rapidly warming regions on Earth, *Nature Geosci*, *6*(2), 139–145, doi:10.1038/ngeo1671.

Cogley, J.G., R. Hock, L.A. Rasmussen, A.A. Arendt, A. Bauder, R.J. Braithwaite, P. Jansson, G. Kaser, M. Möller, L. Nicholson and M. Zemp (2011), Glossary of glacier mass balance and related terms, *IHP-VII Technical Documents in Hydrology No. 86, IACS Contribution No. 2, UNESCO-IHP, Paris.*

Conway, H., and L. A. Rasmussen (2009), Recent thinning and migration of the Western Divide, central West Antarctica, *Geophys. Res. Lett.*, *36*(12), L12502, doi:10.1029/2009GL038072.

Ding, Q., E. J. Steig, D. S. Battisti, and M. Küttel (2011), Winter warming in West Antarctica caused by central tropical Pacific warming, *Nature Geosci*, *4*(6), 398–403, doi:10.1038/ngeo1129.

Dominguez, R. (2011), IceBridge DMS L1B Geolocated and Orthorectified Images, *Boulder, Colorado USA: NASA DAAC at the National Snow and Ice Data Center.*

Eisen, O. et al. (2008), Ground-based measurements of spatial and temporal variability of snow accumulation in East Antarctica, *Rev. Geophys.*, *46*, 39 PP., doi:200810.1029/2006RG000218.

Frezzotti, M., C. Scarchilli, S. Becagli, M. Proposito, and S. Urbini (2013), A synthesis of the Antarctic surface mass balance during the last 800 yr, *The Cryosphere*, *7*(1), 303–319, doi:10.5194/tc-7-303-2013.

Genthon, C., S. Kaspari, and P. A. Mayewski (2005), Interannual variability of the surface mass balance of West Antarctica from ITASE cores and ERA40 reanalyses, 1958–2000, *Climate Dynamics*, *24*(7-8), 759–770, doi:10.1007/s00382-005-0019-2.

Gomez-Garcia, D., F. Rodriguez-Morales, C. Leuschen, and S. Gogineni (2012), KU-Band radar altimeter for surface elevation measurements in polar regions using a wideband chirp generator with improved linearity, in *Geoscience and Remote Sensing Symposium (IGARSS), 2012 IEEE International*, pp. 4617–4620.

Gregory, J. M., and P. Huybrechts (2006), Ice-sheet contributions to future sea-level change, *Philosophical Transactions of the Royal Society of London A: Mathematical, Physical and Engineering Sciences*, *364*(1844), 1709–1732, doi:10.1098/rsta.2006.1796.

Hörhold, M. W., S. Kipfstuhl, F. Wilhelms, J. Freitag, and A. Frenzel (2011), The densification of layered polar firn, *J. Geophys. Res.*, *116*, 15, doi:201110.1029/2009JF001630.

Jacobs, S. S., A. Jenkins, C. F. Giulivi, and P. Dutrieux (2011), Stronger ocean circulation and increased melting under Pine Island Glacier ice shelf, *Nature Geosci*, *4*(8), 519–523, doi:10.1038/ngeo1188.

Joughin, I., and R. B. Alley (2011), Stability of the West Antarctic ice sheet in a warming world, *Nature Geosci*, *4*(8), 506–513, doi:10.1038/ngeo1194.

Joughin, I., B. E. Smith, and B. Medley (2014), Marine ice sheet collapse potentially under way for the Thwaites Glacier Basin, West Antarctica, *Science*, *344*(6185), 735–738, doi:10.1126/science.1249055.

Kaspari, S., P. A. Mayewski, D. A. Dixon, V. B. Spikes, S. B. Sneed, M. J. Handley, and G. S. Hamilton (2004), Climate variability in West Antarctica derived from annual accumulation-rate records from ITASE firn/ice cores, *Annals of Glaciology*, *39*(1), 585–594, doi:10.3189/172756404781814447.

King, J. C., P. S. Anderson, D. G. Vaughan, G. W. Mann, S. D. Mobbs, and S. B. Vosper (2004), Wind-borne redistribution of snow across an Antarctic ice rise, *J. Geophys. Res.*, *109*(D11), D11104, doi:10.1029/2003JD004361.

Kovacs A., Gow A.J., and Morey R.M. (1995), The in-situ dielectric constant of polar firn revisited, *Cold Regions Science and Technology*, *23*(3), 245–256, doi:10.1016/0165-232X(94)00016-Q.

Küttel, M., E. J. Steig, Q. Ding, A. J. Monaghan, and D. S. Battisti (2012), Seasonal climate information preserved in West Antarctic ice core water isotopes: Relationships to temperature, large-scale circulation, and sea ice, *Clim Dyn*, *39*(7-8), 1841–1857, doi:10.1007/s00382-012-1460-7.

Landais, A. et al. (2006), Firn-air δ15N in modern polar sites and glacial–interglacial ice: A model-data mismatch during glacial periods in Antarctica?, *Quaternary Science Reviews*, *25*(1–2), 49–62, doi:10.1016/j.quascirev.2005.06.007.

Lenaerts, J. T. M., M. R. van den Broeke, W. J. van de Berg, E. van Meijgaard, and P. Kuipers Munneke (2012), A new, high-resolution surface mass balance map of Antarctica (1979–2010) based on regional atmospheric climate modeling, *Geophys. Res. Lett.*, *39*(4), L04501, doi:10.1029/2011GL050713.

Leuschen, C., C. Lewis, P. Gogineni, F. Rodriguez-Morales, J. Paden, and J. Li (2011), IceBridge Snow Radar L1B geolocated radar echo strength profiles, *Boulder, Colorado USA: NASA DAAC at the National Snow and Ice Data Center*.

Liu, H, K. C. Jezek, Li, B, and Zhao, Z (2001), Radarsat Antarctic Mapping Project digital elevation model version 2, *Boulder, Colorado USA: National Snow and Ice Data Center.*

Looyenga, H. (1965), Dielectric constant of heterogeneous mixtures, *Physica*, *31(3)*, 401–406.

Medley, B. et al. (2013), Airborne-radar and ice-core observations of annual snow accumulation over Thwaites Glacier, West Antarctica confirm the spatiotemporal variability of global and regional atmospheric models, *Geophysical Research Letters*, *40*(14), 3649–3654, doi:10.1002/grl.50706.

Mireault, Y., P. Tetreault, F. Lahaye, P. Heroux, and J. Kouba (2008), Online precise point positioning: A new, timely service from Natural Resources Canada.(INNOVATION), *GPS World.*

Monaghan, A. J. et al. (2006), Insignificant change in Antarctic snowfall since the international geophysical year, *Science*, *313*(5788), 827–831, doi:10.1126/science.1128243.

Morse, D. L., D. D. Blankenship, E. D. Waddington, and T. A. Neumann (2002), A site for deep ice coring in West Antarctica: Results from aerogeophysical surveys and thermo-kinematic modeling, *Annals of Glaciology*, *35*(1), 36–44, doi:10.3189/172756402781816636.

Nereson, N. A., C. F. Raymond, R. W. Jacobel, and E. D. Waddington (2000), The accumulation pattern across Siple Dome, West Antarctica, inferred from radar-detected internal layers, *Journal of Glaciology*, *46*(152), 75–87, doi:10.3189/172756500781833449.

Nicolas, J. P., and D. H. Bromwich (2014), New reconstruction of Antarctic near-surface temperatures: Multidecadal trends and reliability of global reanalyses, *J. Climate*, *27*(21), 8070–8093, doi:10.1175/JCLI-D-13-00733.1.

Orsi, A. J., B. D. Cornuelle, and J. P. Severinghaus (2012), Little Ice Age cold interval in West Antarctica: Evidence from borehole temperature at the West Antarctic Ice Sheet (WAIS) Divide, *Geophys. Res. Lett.*, *39*(9), L09710, doi:10.1029/2012GL051260.

Panzer, B., D. Gomez-Garcia, C. Leuschen, J. Paden, F. Rodriguez-Morales, A. Patel, T. Markus, B. Holt, and P. Gogineni (2013), An ultra-wideband, microwave radar for measuring snow thickness on sea ice and mapping near-surface internal layers in polar firn, *Journal of Glaciology*, *59*(214), 244–254, doi:10.3189/2013JoG12J128.

Pritchard, H. D., R. J. Arthern, D. G. Vaughan, and L. A. Edwards (2009), Extensive dynamic thinning on the margins of the Greenland and Antarctic ice sheets, *Nature*, *461*(7266), 971–975, doi:10.1038/nature08471.

Rignot, E., J. Mouginot, M. Morlighem, H. Seroussi, and B. Scheuchl (2014), Widespread, rapid grounding line retreat of Pine Island, Thwaites, Smith, and Kohler glaciers, West Antarctica, from 1992 to 2011, *Geophys. Res. Lett.*, *41*(10), 3502–3509, doi:10.1002/2014GL060140.

Rodriguez-Morales, F. et al. (2013), Advanced multifrequency radar instrumentation for polar research, *IEEE Transactions on Geoscience and Remote Sensing*, doi:10.1109/TGRS.2013.2266415.

Rupper, S., W. F. Christensen, E. J. Bickmore, L. Burgener, L. Koenig, M. Koutnik, C. Miège, and R. Forster (2015), The effect of dating uncertainties on net accumulation estimates from firn cores, *Journal of Glaciology*, *accepted*.

Scambos, T. A., T. M. Haran, M. A. Fahnestock, T. H. Painter, and J. Bohlander (2007), MODIS-based Mosaic of Antarctica (MOA) data sets: Continent-wide surface morphology and snow grain size, *Remote Sensing of Environment*, *111*(2–3), 242–257, doi:10.1016/j.rse.2006.12.020.

Schmidtko, S., K. J. Heywood, A. F. Thompson, and S. Aoki (2014), Multidecadal warming of Antarctic waters, *Science*, *346*(6214), 1227–1231, doi:10.1126/science.1256117.

Shepherd, A. et al. (2012), a reconciled estimate of ice-sheet mass balance, *Science*, *338*(6111), 1183–1189, doi:10.1126/science.1228102.

Spikes, V. B., G. S. Hamilton, S. A. Arcone, S. Kaspari, and P. A. Mayewski (2004), Variability in accumulation rates from GPR profiling on the West Antarctic plateau, *Annals of Glaciology*, *39*(1), 238–244, doi:10.3189/172756404781814393.

Steig, E. J., and A. J. Orsi (2013), Climate science: The heat is on in Antarctica, *Nature Geosci*, *6*(2), 87–88, doi:10.1038/ngeo1717.

Steig, E. J., D. P. Schneider, S. D. Rutherford, M. E. Mann, J. C. Comiso, and D. T. Shindell (2009), Warming of the Antarctic ice-sheet surface since the 1957 International Geophysical Year, *Nature*, *457*(7228), 459–462, doi:10.1038/nature07669.

Steig, E. J. et al. (2013), Recent climate and ice-sheet changes in West Antarctica compared with the past 2,000 years, *Nature Geosci*, *6*(5), 372–375, doi:10.1038/ngeo1778.

WAIS Divide Project Members (2013), Onset of deglacial warming in West Antarctica driven by local orbital forcing, *Nature*, *500*(7463), 440–444, doi:10.1038/nature12376.

CHAPTER 5

CONCLUSIONS

5.1. Summary

In this dissertation, I derived past snow accumulation rates and mapped the presence of subsurface water over specific sectors of the Greenland Ice Sheet and the West Antarctic Ice Sheet, using a set of different radar systems. Snow/ice-penetrating radars are strong tools to bridge firn-core point observations to get a spatial understanding of the snow-accumulation distribution due to atmospheric patterns and wind redistribution of snow on an undulating surface. Over West Antarctica, frequency-modulated continuous-wave (FMCW) radars (2-18 GHz) with a ~5 cm vertical resolution detect internal firn horizons with an annual resolution. However, lower-frequency systems (e.g., 400 MHz) only detect dominant continuous internal horizons and therefore, accumulation rates can only be derived for multiannual periods. The choice of the radar frequency depends on the penetration depth required to detect specific subsurface features. In Southeast Greenland, the firn aquifer water table found on average at 20-m depth was detected by both 400-MHz ground-based radar and 750-MHz airborne radar system, but not detected by the 2-8 GHz airborne radar that lacked the penetration depth necessary.

In Chapter 2, I derive accumulation rates over a 70-km transect in Southeast Greenland from ice-penetrating radar observations. I find that snow accumulation rates simulated by a calibrated regional climate model (Polar MM5) capture the mean annual accumulation rates over the southeast part of Greenland. However, both interannual variability and small-scale spatial variations found in the radar-derived accumulation rates and in the firn cores due to surface topography are not taken into account during the model simulations. Following an elevation gradient from 2350 m to 1830 m toward the southeast coast of Greenland, I find that accumulation increases by 52% (~0.43 m w.eq. y^{-1}). The maximum spatial variability estimated from the radar, which is not captured by single-point firn cores, is up to 23% (0.24 m w.eq. y^{-1}) over distance less than 10 km. Looking at the temporal variations from the firn cores, I did not find any significant trend in accumulation since 1973, despite the temperature warming observed in the Arctic. Finally, the three firn cores (~50 m) that were collected are strongly intercorrelated in terms of past accumulation interannual variability but are not significantly correlated to the North Atlantic Oscillation (NAO), meaning that additional climatic patterns could have been at play to explain the signal variability in accumulation.

For Chapter 3, I used different radar systems operated from the ground and from an airplane to spatially map the extent of a firn aquifer and the depth to its water table over the Greenland ice sheet. Widespread perennial firn aquifers are found in an elevation range of ~1200-200 m within the percolation zone of the Greenland ice sheet. They represent an area of ~28,500 km^2 based on mapping their extent with radar data, and have average depth of 22±8 m below the snow surface. I inferred the presence of a firn aquifer since the 1990s using the radar-depth sounder data that were deployed by CReSIS from

an aircraft. When combining the radar data with surface elevation profiles, I found that firn aquifers are initiated by strong surface slope gradients that increase the quantity of meltwater to be collected. The firn aquifer is unconfined and the flow of water is local, driven by ice-sheet surface undulations. A succession of local flow cells are hypothesized based on numerical hydraulic simulations using the water table depth from the radar data as boundary conditions and some water could be discharged at the steep-to-flat transitions. Finally, based on repeated radar profiles for the upper part of Helheim Glacier, I suspect water drainage into the crevasses, but both the volume of water and flow rate remain unknown.

In Chapter 4 of this dissertation, I quantified the spatial variations of the recent snow-accumulation rates on both sides of the West Antarctic Ice Sheet (WAIS) ice divide using a combination of firn cores and high-frequency radars developed by CReSIS. Using radar-imaged internal reflections, I found that there is a 75% (± 0.20 m w.eq. y^{-1}) spatial increase of the averaged-accumulation rate along a 70-km transect from the ice divide toward the Amundsen Sea side. At the ice divide, I find a good agreement between the depth-age scales obtained by the radar and the firn cores. On the Amundsen Sea side, where higher accumulation rates are found, the radar-derived accumulation rates are higher than the firn-core accumulation rates. This mismatch can be caused by a noisy seasonal cycle in the isotopes and solutes challenging the establishment of a depth-age scale. Finally, small-scale radar grids (~10 km length) are used to investigate the small-scale variability of accumulation and show how a single-point firn core is representative of a wider region. In the vicinity of the firn core at SEAT10-4, I find up to 1.3 m of vertical variations for a continuous layer located at 25-m depth across the radar grid. The

averaged accumulation-rate variability is 0.1 m w.eq. y^{-1} in the vicinity of the core site (less than 1.5 km away), which is not taken into account by a single point measurement.

5.2. Broader impacts of this work

This work aimed to further our knowledge on the mass balance of the ice sheets of Greenland and Antarctica. Net snow accumulation is the only net mass input for both ice sheets that could offset the mass loss represented by ice discharge, surface melt and runoff, and basal melt. Accumulation is variable in space and time, challenging the establishment of a depth-age scale that would be representative of a larger region over the ice sheet. The accumulation data collected during the different fieldwork over Greenland and Antarctica show the importance of both spatial and temporal variability. For the spatial variability, radar-derived accumulation rates capture small-scale accumulation patterns (< 10 km) driven by the undulated surface of the ice sheets that is not captured by the model. This observation could have an interesting potential using new high-resolution digital elevation model to simulate the accumulation to be expected based on ice-sheet topography. The regional spatial accumulation gradient observed from the radar data was captured by the calibrated Polar MM5 regional model for SE Greenland. The accumulation gradient can therefore be used with a high-resolution surface elevation model to precise accumulation patterns, assuming that those surface features are steady through time. The temporal variability of accumulation for the time period investigated provide information on the past climate variability. For the Greenland ice sheet part of my work, the depth-age scales obtained from the Southeast sector only span the last 40 years, which makes it difficult to establish a trend from this short time record and given

the signal variability. For both the Greenland and Antarctic projects, I did not find any increasing trend of accumulation over the last 40 years. Over West Antarctica, our firn core measurements show even a decreasing trend of accumulation (Burgener et al., 2013), which highlights the importance of taking into account regional climatic patterns, especially across Antarctica where signals may be different. For Greenland, an increase in snowfall was inferred since the end of the Little Ice Age based on a recent accumulation reconstruction using firn cores and a regional climate model (Box et al., 2013). Based on this reconstruction, the accumulation signal correlates well with the North Atlantic Oscillation index, which is an indicator of the large-scale climate pattern, but changes sign over a period of 135 years, indicating that decadal processes are part of the climate variability.

The Greenland firn aquifer will impact the surface mass balance of the Greenland ice sheet. The recent finding of this subsurface water in the firn highlights the current lack of knowledge regarding snow processes active in the percolation zone of the Greenland ice sheet where surface melt is present. The remaining challenge is to connect the firn aquifer to the rest of the Greenland hydrologic system. The aquifer likely impacts ice-sheet mass balance in at least three ways: firn densification, contribution to runoff, and ice dynamics. The firn aquifer is an integral part of the ice-sheet hydrology and this relates to our ability to estimate uncertainties in the runoff in the percolation regions of the ice sheet in a warming climate (Harper et al., 2014). The presence of an aquifer needs to be accounted while deriving a volume change obtained from satellite or airborne altimeters to a mass change. Such a perennial body of water in the subsurface increases the density of the firn column at least temporally. Knowledge of the processes active in

the percolation zone is important to determine the position and surface elevation of the meltwater runoff line. The runoff evolution in the future of the ice sheet is crucial, as it directly impacts the sea level rise when meltwater is able to directly leave the ice sheet and enter in the ocean.

5.3. Future research directions

The research presented in this dissertation answers many questions, but it also allows me to ask many new questions. Follow-on research can be done using existing datasets, but there is also a need to collect new data over both Greenland and the Antarctic ice sheet. Fortunately, since 2010, the NASA Operation IceBridge (OIB) mission has been collecting a large amount of high-quality radar data, covering a good portion of the Greenland ice sheet, and across in West Antarctica. This dataset and other planned ground-based investigations leave open many opportunities for new work. In the following, I present possible future research directions for each chapter.

Building on the findings in Chapter 2, I would use the data collected by Accumulation Radar onboard of the NASA OIB P-3 airplane over Greenland. The Accumulation Radar has been successful at imaging internal layers up to a few hundred meters depth in the ice sheet and accumulation rates can be derived from these layers (Rodriguez-Morales et al., 2013; Medley et al., 2014). During the 2011 OIB season, the southeast region of Greenland was extensively surveyed, providing several ~500-km radar profiles parallel to different elevation contour lines. At high-elevation (> ~2000 m), in nearly dry firn conditions, multiannual internal isochrones can be followed down to 50 m depth. To derive accumulation rates, a similar method to the one used in Chapter 2

could be used, by dating the radar-imaged isochrones with a firn-core depth-age scale (collected at a similar time). The density information obtained from the firn cores would also be useful to convert radar TWT to depth. In sectors closer to the coast (< 2000 m a.s.l.), with significant summer melt, the penetration depth of the radar signal is challenged. In this region, preliminary assessment of the Accumulation Radar data does not show a good preservation of the internal firn layering beyond the last summer melt, which is a relatively bright subsurface reflector. Knowing the depth of this melt layer relative to the snow surface is still important as it corresponds to the seasonal snow depth, which could be later converted into a snow-water equivalent (SWE) product. For this part of the work, I recommend using the Snow Radar, also onboard the aircraft, but this system has a higher frequency range. This will allow a better vertical resolution while tracing the last summer layer. This second method would give the last year of snow accumulation with some uncertainties. The main uncertainty source is related to snow density, which is required for both TWT-to-depth conversion and SWE estimation. Also, this method will not account for any snow falling in the spring past airborne-radar collection date. On the other hand, the main advantage of this method will be to capture the small-scale (<10 km) processes in snow accumulation that are currently not handled by larger-scale regional-climate-model simulations. These radar-derived accumulation rates and accumulation maps at the ice-sheet scale will be valuable to constrain regional climate model mass inputs for past, present, and future simulations. Another interesting direction with this radar data will be to derive firn compaction rates, over repeated flightlines (separated a year or two apart). Similar continuous internal horizons can be

followed and the difference between two known and dated horizons can be used to calculate firn compaction rates (Kruetzmann et al., 2011; Simonsen et al., 2013).

Building on the work in Chapter 3, exciting new work can be done because there remains a lot to learn about the firn aquifer. After mapping the extent of the aquifer using airborne radar data, I have raised numerous research questions, including: (1) What is the fate of the water table? (2) What is the time of residence of the water in the aquifer? (3) How to image the water-saturated firn / ice transition? (4) What are the consequences of the aquifer on surface mass balance estimates? To help answer question (3), a lower-frequency radar system should be applied above the firn aquifer. Indeed, the current 400-MHz surface-based radar does a good job imaging the water table (Forster et al., 2014), but attenuation of the radar signal prevents imaging below this interface. However, the thickness of this a water-saturated layer is critical to deduce water volume storage and the spatial variation of the water. The sharp dielectric transition observed at the water table interface contrasts with the progressive transition from water-saturated firn to ice. Since the scattering and absorption (radio wave extinction) increases with radio frequency when meltwater and soaked firn conditions are present (Smith and Evans 1972), lower-frequencies are recommended. By using surface-based radar operating at lower frequencies (10 MHz – 40 MHz), chances to obtain signal information below the water table surface would increase. Successful echo soundings of temperate glaciers with presence of 0°C ice and liquid water using 10 to 32 MHz radars have been reported (i.e., Sverrisson et al., 1980). In combination with this, common Mid-Point surveys (CMPs) can be used to obtain the velocity variations of the electromagnetic waves at depth and infer density changes above, within, and below the firn aquifer. CMP measurements can

provide a way to find the phase velocity needed for time-depth conversions to accurately monitor at what depth changes in the firn/ice structure occur. This technique has been used recently in West Greenland to estimate density profiles of the upper 80 m of the ice sheet (Brown et al., 2012). In addition to the radar work, other geophysical in-situ techniques can be performed in aquifer regions. Upcoming fieldwork in spring 2015 will further investigate the aquifer by bringing in other geophysical techniques and hydrological measurements to determine the physical properties of the water table.

Besides geophysical field-based methods, numerical modeling developments can be pursued. The infiltration of water into the snow and firn is a nonuniform process, therefore challenging to simulate. When meltwater travels downward throughout the porous winter snowpack and the firn, snow metamorphism is enhanced and the inter-granular space is filled with water. For the Greenland percolation zone, the firn stratigraphy is found to be heterogeneous, where ice lenses (horizontal) and ice columns (vertical) offer preferential pathways for meltwater to travel, changing firn physical properties in their vicinity. A simple 1-D water-bucket percolation scheme with accumulation and melt used as forcing has been used to simulate persisting liquid water depth over the Greenland winter (Forster et al., 2014; Kuipers Munneke et al., 2014). But these initial modeling efforts need to be expanded to simulate an accurate water volume at a 20-m depth in the firn. Field measurements of water volume, temperature, water height, and lateral flow will improve our understanding of the snow physics to be implemented in the simulations to handle water percolation, movement, and retention within the snow/firn as well as its thermal properties. Initial work toward this direction was performed using the 1-D snow-model CROCUS, which was primarily designed for

seasonal alpine snow and avalanche forecasting (Brun et al., 1989; Brun et al., 1992). More Recently, CROCUS has been integrated in the externalized surface module SURFEX, facilitating stand-alone and coupled simulations (Vionnet et al., 2012). The model provides the temporal evolution of variables, temperature, density, liquid water content, and snow type, for each snow/firn layer. Physical processes like heat conduction, snow compaction, snow melt, water percolation, and subsequent refreezing are handled by the model. Initial simulations with CROCUS adapted to SE Greenland conditions allowed for nearly complete water retention in the pore space and water was simulated at depths of 10 m to 40 m, persisting over the winter. These initial simulations of depth to the water-saturated layer and temperature profiles closely match initial field measurements but require higher than average accumulation. Therefore, future research directions would be in running sensitivity tests under various accumulation scenarios and with maximum water retention for each snow layer in order to match the observed layer saturation, water depths, and temperatures. Simulations should also be conducted to constrain the bottom of the firn aquifer by varying bottom boundary conditions. Finally, water-saturated firn in 3-D could be simulated to allow lateral flow of water to help answering research questions (1) and (2).

Chapter 4 is a work in progress. The firn cores collected in 2011 during the second snowmobile traverse (SEAT-11) have not been fully processed yet and their depth-age scales were not available at the time of this study. The accumulation-rate mismatch observed between the firn cores and the radar data at the high-accumulation sites is interesting and will be fully explored in future work. Since the vertical resolution of the radar is only about 5 cm, it would be interesting to directly compare the $\delta^{18}O$

profile obtained at a 2-cm resolution to a radar trace intensity profile to see if the radar reflections could be correlated to the isotopes variations. At a snow-pit scale, detailed radar experiences were done with a metal plate to precisely relate the observed pit snow/firn stratigraphy with the radar layers and could provide additional information to further our knowledge on the cause of the signal reflections. We would also explore the frequency dependency at both C-band and Ku-band on the snow physical variables to see if different densification processes could lead (or contribute) to the different radar profile observed on either side of the West divide, likely working together with snow accumulation variations. An additional 500 km of radar data still needs to be processed, and the internal layers need to be traced for SEAT-11. This second traverse started at Byrd Station, ~160 km away from the ice divide toward the Ross Sea and would permit further exploration of the radar data in a low-accumulation regime, to see if any temporally increasing trend of accumulation could be detected for the last 50-60 years, which may correlate with the recent air temperature warming observed at Byrd Station (Bromwich et al., 2013).

5.4. References

Box, J. E. et al. (2013), Greenland ice sheet mass balance reconstruction. Part I: Net snow accumulation (1600–2009), *J. Climate*, *26*(11), 3919–3934, doi:10.1175/JCLI-D-12-00373.1.

Bromwich, D. H., J. P. Nicolas, A. J. Monaghan, M. A. Lazzara, L. M. Keller, G. A. Weidner, and A. B. Wilson (2013), Central West Antarctica among the most rapidly warming regions on Earth, *Nature Geosci*, *6*(2), 139–145, doi:10.1038/ngeo1671.

Brown, J., J. Bradford, J. Harper, W. T. Pfeffer, N. Humphrey, and E. Mosley-Thompson (2012), Georadar-derived estimates of firn density in the percolation zone, western Greenland ice sheet, *Journal of Geophysical Research: Earth Surface*, *117*(F1), n/a–n/a, doi:10.1029/2011JF002089.

Brun, E., E. Martin, V. Simon, C. Gendre, and C. Coléou (1989), An energy and mass model of snow cover suitable for operational avalanche forecasting., *J. Glaciol.*, *35*(121), 333–342.

Brun, E., P. David, M. Sudul, and G. Brunot (1992), A numerical model to simulate snow-cover stratigraphy for operational avalanche forecasting, *Journal of Glaciology*, *38*, 13–22.

Burgener, L. et al. (2013), An observed negative trend in West Antarctic accumulation rates from 1975 to 2010: Evidence from new observed and simulated records, *J. Geophys. Res. Atmos.*, *118*(10), 4205–4216, doi:10.1002/jgrd.50362.

Forster, R. R. et al. (2014), Extensive liquid meltwater storage in firn within the Greenland ice sheet, *Nature Geosci*, *7*(2), 95–98, doi:10.1038/ngeo2043.

Harper, J. (2014), Cryosphere: Greenland's lurking aquifer, *Nature Geosci*, *7*(2), 86–87, doi:10.1038/ngeo2061.

Kruetzmann, N. C., W. Rack, A. J. McDonald, and S. E. George (2011), Snow accumulation and compaction derived from GPR data near Ross Island, Antarctica, *The Cryosphere*, *5*(2), 391–404, doi:10.5194/tc-5-391-2011.

Kuipers Munneke, P., S. R. M. Ligtenberg, M. R. van den Broeke, J. H. van Angelen, and R. R. Forster (2014), Explaining the presence of perennial liquid water bodies in the firn of the Greenland Ice Sheet, *Geophys. Res. Lett.*, *41*(2), 476–483, doi:10.1002/2013GL058389.

Medley, B. et al. (2014), Constraining the recent mass balance of Pine Island and Thwaites glaciers, West Antarctica, with airborne observations of snow accumulation, *The Cryosphere*, *8*(4), 1375–1392, doi:10.5194/tc-8-1375-2014.

Rodriguez-Morales, F. et al. (2013), Advanced multifrequency radar instrumentation for polar research, *IEEE Transactions on Geoscience and Remote Sensing, Early Access Online*, doi:10.1109/TGRS.2013.2266415.

Simonsen, S. B., L. Stenseng, G. Aðalgeirsdóttir, R. S. Fausto, C. S. Hvidberg, and P. Lucas-Pichery (2013), Assessing a multilayered dynamic firn-compaction model for Greenland with ASIRAS radar measurements, *Journal of Glaciology*, *59*(215), 545–558, doi:10.3189/2013JoG12J158.

Smith, B. M., and Evans, S (1972), Radio echo sounding: Absorption and scattering by water inclusion and ice lenses, *Journal of Glaciology*, *11*, 133–146.

Sverrisson M, Johannsson AE, and Bjornsson H (1980), Radio-echo equipment for depth sounding of temperate glaciers, *Journal of Glaciology*, *25*(93), 477–486.

Vionnet, V., E. Brun, S. Morin, A. Boone, S. Faroux, P. Le Moigne, E. Martin, and J.-M. Willemet (2012), The detailed snowpack scheme Crocus and its implementation in SURFEX v7.2, *Geoscientific Model Development*, *5*(3), 773–791, doi:10.5194/gmd-5-773-2012.